# Compact Multi-Band Differential Bandpass Filters and Diplexers Based on Multimode Resonators

マルチモード共振器を用いた小型マルチバンド
差動型帯域通過フィルタとダイプレクサに関する研究

２０１９年3月

埼玉大学大学院理工学研究科（博士後期課程）

理工学専攻（主指導教員　馬　哲旺）

任　宝平

# DEDICATION

To

My supervisors

And

My parents, my sisters, and

my beloved girl

# ACKNOLEDGEMENTS

# SUMMARY

In modern RF/microwave front-ends of transceivers, RF/microwave filters and diplexers are key passive components for realizing high performance of the systems. In recent years, differential circuits have attracted much attention because of their ability of rejecting common-mode (CM) noise and increasing significantly the immunity and sensitivity of communication systems.

In this dissertation, novel microstrip dual-mode, quadruple-mode, and sext-mode resonators are proposed, and by using these resonators, four compact multi-band differential bandpass filters (BPFs) and one diplexer are developed to meet the increasing demand for high-immunity and high selectivity BPFs in future communication systems.

First, a novel stepped-impedance square ring loaded resonator (SRLR) with quadruple-mode resonant characteristics is proposed. Compared with conventional SRLRs, the new stepped-impedance SRLR can provide one more design freedom to reach a large frequency separation between differential-mode (DM) resonances and common-mode (CM) resonances, and this is very important in the design of multi-band differential BPFs with high CM noise suppression. Moreover, the frequency discrepancy technique is applied in the filter design to separate the CM resonances in adjacent resonators so that the transmission of CM signals is weakened, and the CM suppression is increased. By using the new quadruple-mode stepped-impedance SRLRs, a compact second-order dual-band differential BPF is developed. Source-load coupling after adding two short microstrip lines is introduced to produce multiple transmission zeros and improve significantly the frequency selectivity of DM passbands. The experimental results agree well with the design simulation, which verifies well the proposed structure and design method.

Next, by loading two additional open-circuited stubs to the above SRLR, a new sext-mode stepped-impedance SRLR is obtained. The new resonator has six resonant modes, including three DM resonances and three CM resonances. The operating mechanism of these resonances are investigated by using the even- and odd-mode method and simulation techniques. Three DM resonances are used to configure a second-order tri-band differential BPF. The filter is fabricated, and the measured frequency response agrees well with the theoretical prediction and verifies the proposed resonator and design concept.

The measured passband insertion losses in the above second-order filters are relatively large (about 1 ~ 2 dB) because of the relatively large surface resistance of copper film commonly used in planar microwave circuits. To overcome this problem, the high-temperature superconducting (HTS) techniques are introduced in developing multi-band BPFs, because the HTS film has a surface resistance two- to three- order lower than the normal copper film at low microwave frequencies. In this dissertation, a fourth-order HTS dual-band differential BPF is developed using modified SRLRs, and its measured passband insertion loss is better than 0.16 dB. An eighth-order HTS dual-band differential BPFs is developed using symmetric-stub-loaded resonators, and its measured passband insertion loss is better than 0.35 dB. In the design of these two filters, independent control of both the midband frequencies and the bandwidths of the two passbands are achieved. Benefiting from the HTS technology and the precise design, the fabricated filters show excellent performance such as extremely low insertion loss, high frequency selectivity, and deep CM suppression, which are not realizable using normal conductor substrates.

Finally, a compact 2.45/3.45 GHz diplexer is developed by using a novel hybrid resonant structure. The proposed structure consists of a microstrip stub-loaded dual-mode resonator (MSLDR) and a slotline stub-loaded dual-mode resonator (SSLDR). These two dual-mode resonators are placed on the top and bottom layer of a substrate, respectively, forming two separate signal channels of the diplexer. No matching network is required in the circuit, which simplifies the design of the diplexer, and reduce significantly the circuit size.

# CONTENTS

**Publications**

**Bibliography**

# Chapter 1

# Introduction

## 1.1  Motivation and Objectives

In the past decade, the rapid development in computer aided design (CAD) and fabrication technologies and successful commercial applications of wireless communications have significantly improved our daily lives, because we can free ourselves from the limitation of cables in communication with others. The mobile phones, internet, and the upcoming Internet of Thing (IoT), the fifth-generation radio systems, and the replacement of wired connections with Wi-Fi and Bluetooth enabled people to access to a wide range of information from anywhere and at any time, as shown the sketch of IoT in Fig. 1.1. For providing more comfortable and economic wireless access service, the development of the wireless systems or handed devices show the tendency of more compact size and multi-functions.

Microwave filters and diplexers, which are among the most commonly used passive components in microwave systems, play important roles in many RF/microwave applications. Fig. 1.2 illustrates a simplified block diagram of the front-end of a transceiver. As shown in the figure, the diplexer provides two channels to connect the antenna and transceiver links, while the bandpass filters (BPFs) are used to select needed frequencies and suppress unnecessary signals. Emerging applications continue to challenge microwave filters and diplexers with ever more stringent requirements of higher performance, smaller size, lighter weight, lower cost, and multi-channel responses.

However, in various communication systems with constantly increased integration of microwave/RF circuits, the problems such as signal cross-talk, electromagnetic interference, and power loss are becoming more and more serious. Fortunately, as an attractive approach, differential circuit can be used in a transceiver to solve these problems. As compared with single-ended signals, differential-mode signals exhibit lower

Fig. 1.1. Sketch of Internet of Thing (IoT).
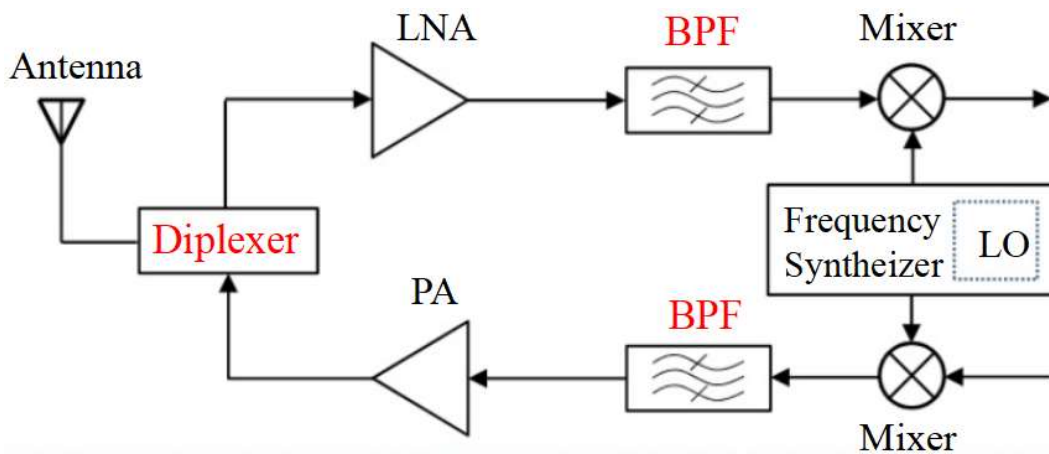


Fig. 1.2. Schematic of generic transceiver frond end.

electromagnetic interference (EMI) and higher immunity to electromagnetic noise and crosstalk. Consequently, a better signal integrity and a higher signal-to-noise ratio (SNR) can be achieved in differential systems. These aspects are especially critical in modern digital systems, where logic signal swing and noise margin have dramatically decreased and hence are less immune to the effects of noise and EMI. Therefore, differential bandpass filters (BPFs) and diplexers with multi-channel responses are highly required in modern communication equipment and systems with ever increasing demand for high reliability, compact size, low cost, and multi-services.

Since the BPF is at the front end of the transceiver, it is essential that its noise figure is low. To achieve a low noise figure for a passive filter, the unloaded quality factor of its resonators needs to be very high. As we know, the use of thin film high temperature superconductors (HTS) with ultra-low surface resistance can achieve high quality factor

resonators for planar filters [1]. HTS planar resonators have been designed with unloaded quality factors as high as 30000. Thus, the HTS technique makes it possible to realize very low passband insertion loss in high-order planar filters. There are a number of attractive advantages of high-order HTS filters, some of these are (1) ultra-low loss in the passband, (2) steep passband skirt, (3) high rejection in stopband, (4) possible to design an ultra-narrow BPF, and (5) small circuit size.

In order to miniaturize multiband RF/microwave filters, multimode resonator, which behaves as the same functions of multiple single-mode resonators, is one of the popular and powerful methods. In addition, slotlines or defected ground structure etched on the ground plane and such that make full use of the limited space in integrated circuit board are also popular used in designing microwave passive circuits with compact size.

The objective of this doctoral research is to carry out first a systematic investigation on the resonant characteristics of various microstrip multimode resonators (MMRs) with varied or further developed configurations. Next, by using these resonators, novel multi-band differential BPFs on the copper-based substrate and high-order dual-band differential BPFs with ultra-low loss and high selectivity using the HTS material are developed. Besides, a novel hybrid resonant structure consisting of a microstrip resonator and a slotline resonant is proposed and then used to develop a diplexer which needs no matching network and has thereby a significantly reduced circuit size and simplified design process.

## 1.2 Literature Review on Multiband Differential Filters

Fig. 1.3 shows a simplified architecture of the differential receiver, the differential filters, as one of key component in the differential receiver, have the advantage of high immunity to interference, high reliability and high output power, as described above [2], [3]. Most of works are concentrated on single-band/wideband differential filters [4]-[24]. With the ever-increasing demands for multi-band wireless equipment providing multi-functional services, the research of multi-band differential BPFs become a hot topic.

In past few years, various multi-band differential BPFs have been designed with the desired performance of good differential-mode (DM) passbands and deep CM suppression.
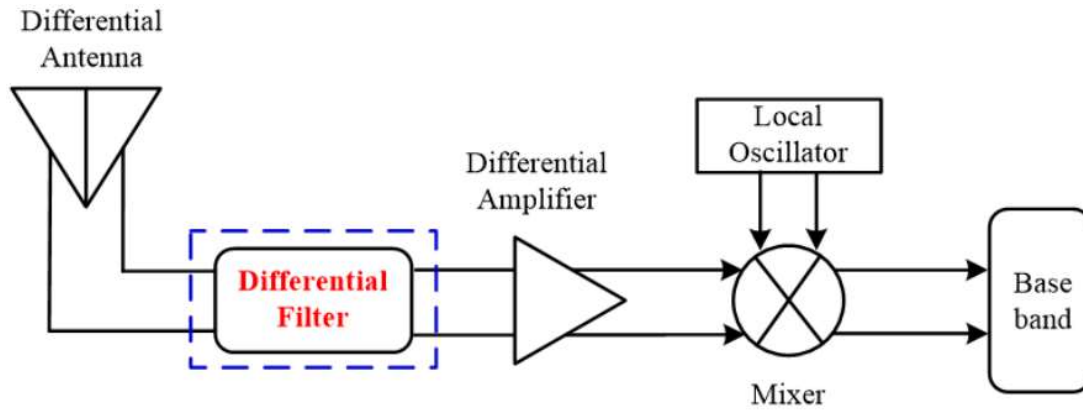
Fig. 1.3  Simplified architecture of the differential receiver.

After searched in IEEE Xplore and Google Scholar, we found only 51 papers in total, 37 in various journals and 14 from conferences, were reported in public until now. Due to the limitation of design difficulty, most of them are dual-band differential BPFs. To construct compact dual-band differential BPFs, manifold multimode resonators, such as the coupled SIRs [25], [26] and center-loaded half-wavelength resonators [27]-[30]. Fig. 1.4(a) and (b) show the configuration of a dual-band differential filter based on coupled SIRs and its DM and CM frequency responses, respectively. Usually, extra terminating microstrip lines [25], [28], [29] or surface-mounted devices (SMDs) [26], [27] are loaded to resonators to deepen or widen the CM rejection.

To simplify the design, various multimode resonators with intrinsic CM suppression, such as the asymmetrical coupled-lines [31], open/short-ended coupled SIRs [32], slotline topologies [33], [34], doubly short-ended half-wavelength resonator in coupled-line structure [35], stub-loaded dumbbell-shaped resonator embedded defected ground structure (DGS) [36] are used to construct high CM rejection dual-band differential BPFs without using any additionally loaded elements. The coupled-lines or coupled resonators in these design exhibit the inherent property of all-stop frequency response and the used slotline or DGS topologies with the microstrip/slotline transitions have the ability of inhibiting the transmission of CM signal. Fig. 5(a) and (b) presents the physical layout of dual-band differential filters based on the coupled-lines topology and slotline topology, respectively. It is shown in Fig. 5(a) that the asymmetrical coupled lines with open- and short-circuited ends will be obtained under CM excitation and inherently has the bandstop characteristic on CM signals. In Fig. 5(b), it is clearly see that the differential pairs feeding
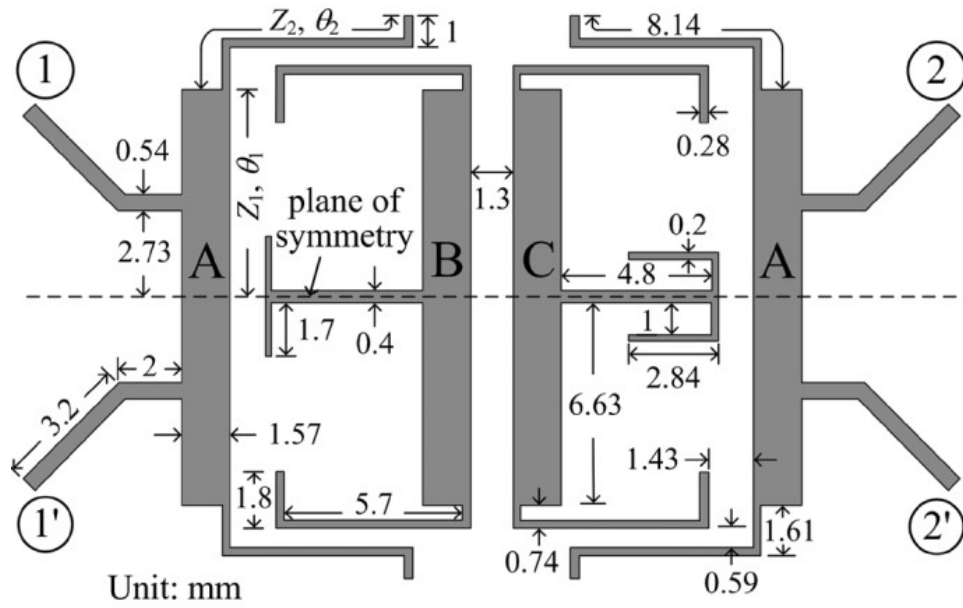
(a)
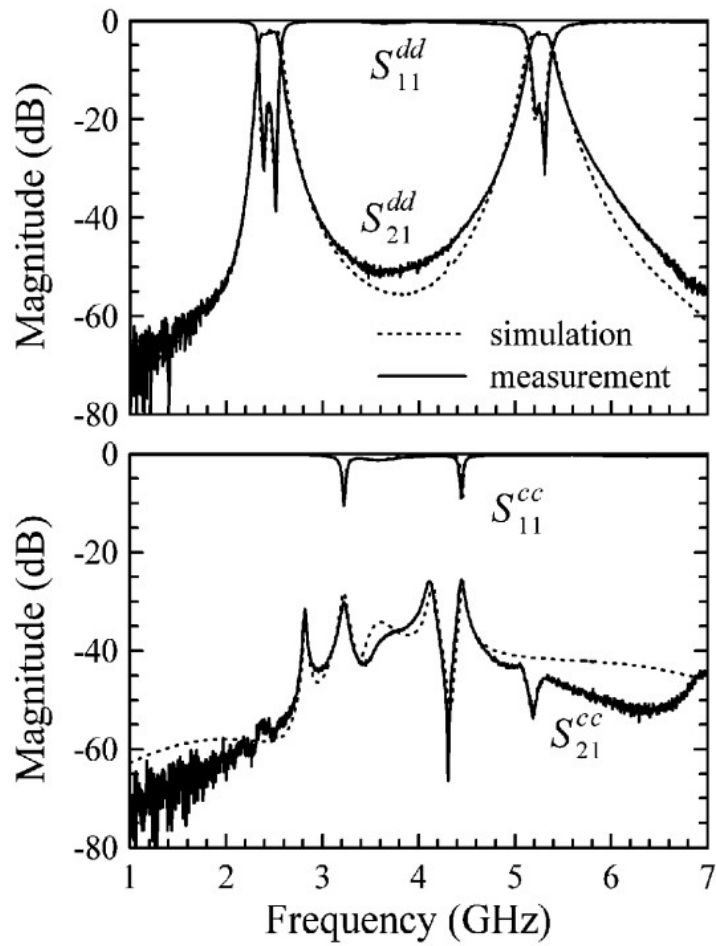


(b)

Fig. 1.4.  (a) Configuration of a fourth-order dual-band differential filter.

(b) Its DM and CM frequency responses.

(a)



(b)
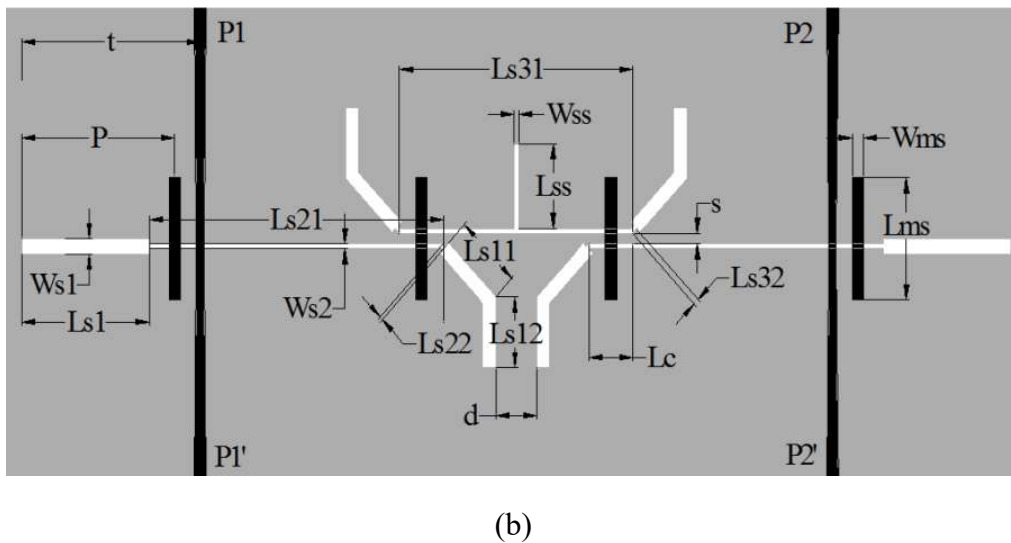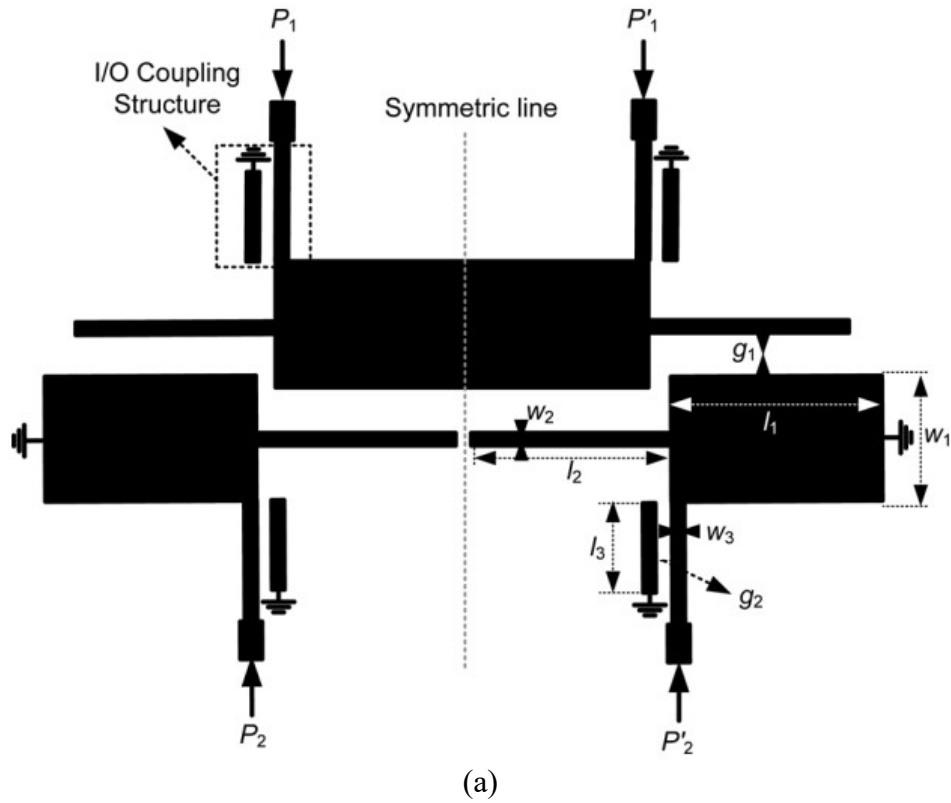
Fig. 1.5.　Physical layout the dual-band differential filter based on
(a) coupled-lines and (b) slotline topology.

structure is natural the microstrip/slotline transition and thereby the CM transmission can be intrinsically rejected without affecting the DM frequency response.

　In addition, substrate integrated waveguide (SIW) technologies with high power handling are used to design dual-band differential filters [37], [38], but circuit size is always large, as shown the circuit in Fig. 1.6(a) occupied $2.7 \times 1.27$ $\lambda g^2$. Two DM
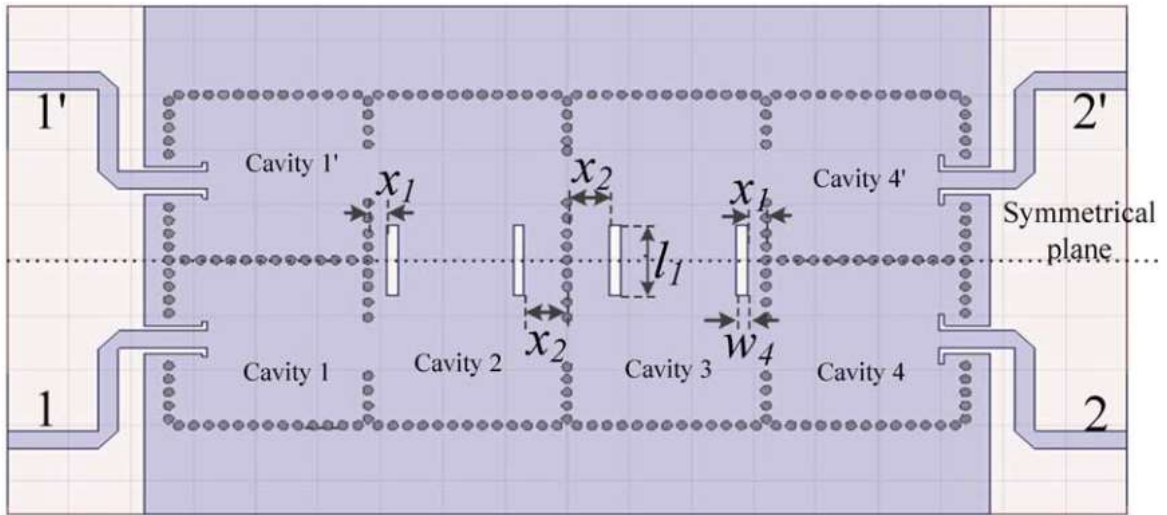
(a)
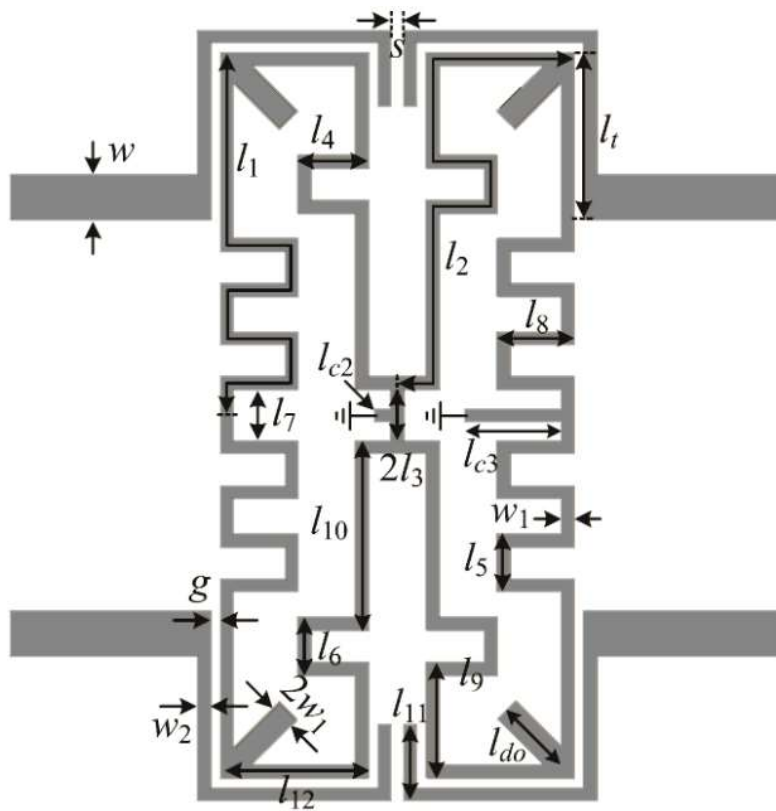


(b)

Fig. 1.6.   Configuration of the dual-band differential filter based on
(a) SIW technology and (b) quad-mode resonator.

passbands are derived by the dominant modes and the higher order modes. The CM resonances are offset with the DM resonances and can not be well excited and transmitted from input to output port. Then, a single quad-mode stub-loaded twin-ring resonator is
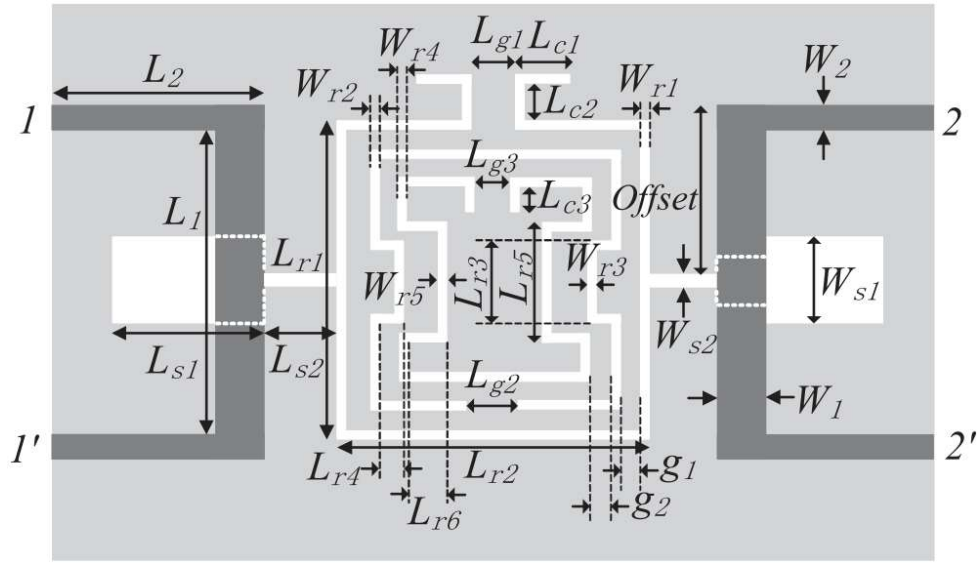
(a)
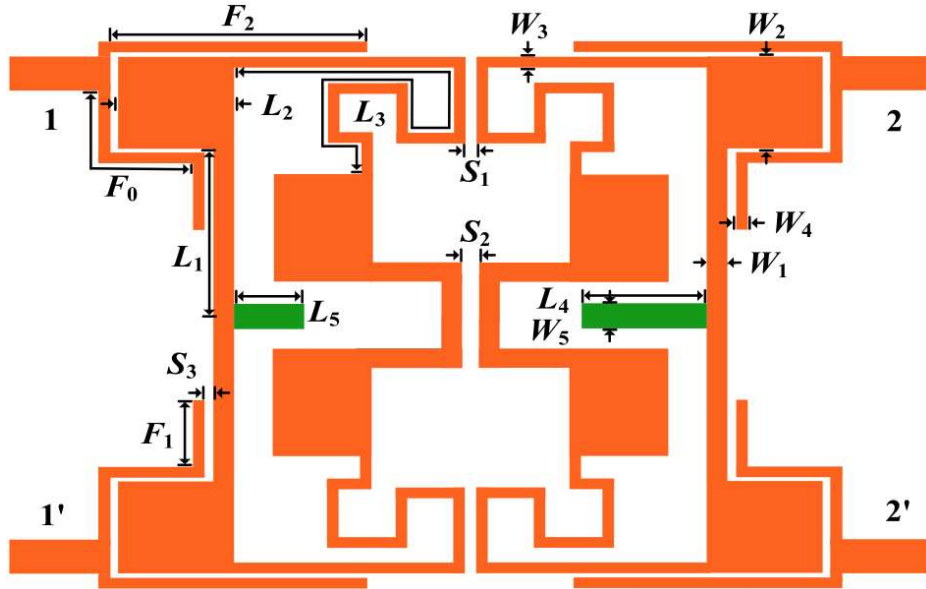


(b)

Fig. 1.7.   Configuration of the dual-band differential filter based on
(a) SIW technology and (b) quad-mode resonator.

proposed to design a compact dual-band differential BPF [39].

For tri-band differential BPFs demonstration, to the best of our knowledge, only five works are reported [40]-[44]. Multi-stub-loaded resonators in [40], [41], complementary split-ring resonator in [42], octo-section stepped-impedance ring resonator in [43], and three pairs of half-wavelength resonators with slotline coupled-feed structure [44]. Fig. 1.7(a) and (b) present the configuration of the designed dual-band differential based on the
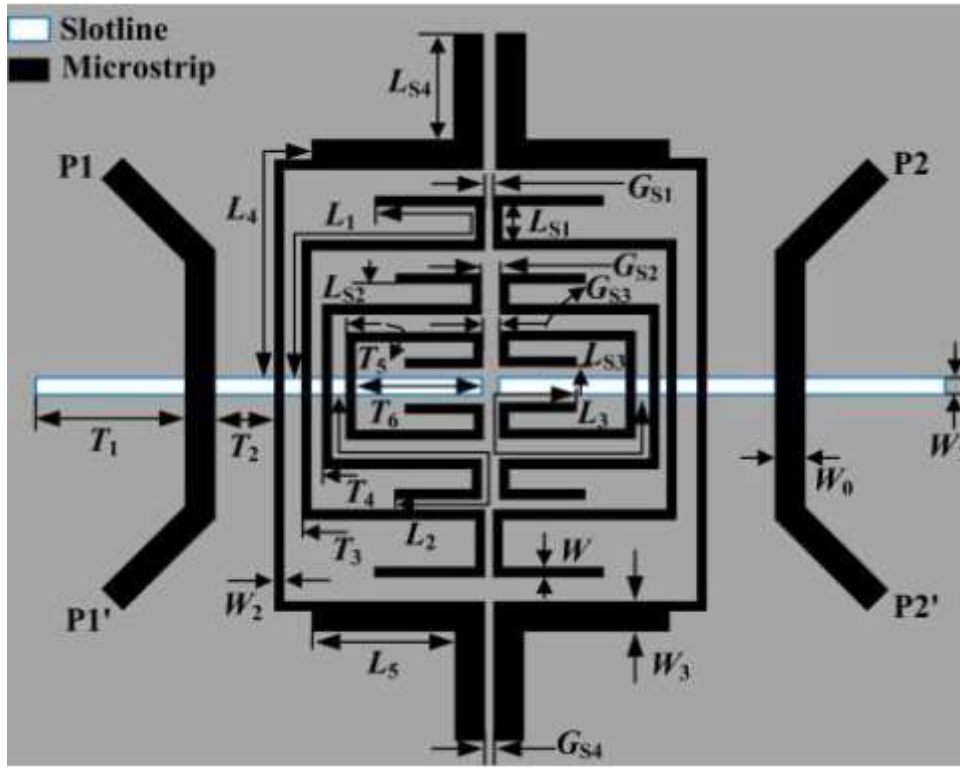
Fig. 1.8.  Configuration of the quad-band differential filter based on
half-wavelength resonators and slotline coupling feed.

complementary split-ring resonator and octo-section stepped-impedance ring resonator, respectively. As shown in Fig. 1.7(a), three DM passbands are formed by three coupled complementary split ring resonators and the CM interference is suppressed by the stepped-impedance microstrip-slotline transition structure.

In addition, there is only one work we found on the design of quad-band differential BPF developed from the design of tri-band differential filter in [43], as demonstrated in Fig. 1.8. For DM, the quad-band performance is realized by four pairs of half-wavelength resonators. Besides, slotline coupled-feed structure is employed to suppress the CM, due to its intrinsic CM rejection.

Although good DM transmission are achieved in these reports, these designs suffer from large circuit sizes because of the cascaded multiple resonators or the CM suppression needs to be improved. In all, the study on differential multi-band BPFs is in progress, but still limited. Besides, these filters are suffering from the high insertion losses caused by the large surface resistance of normal copper board.
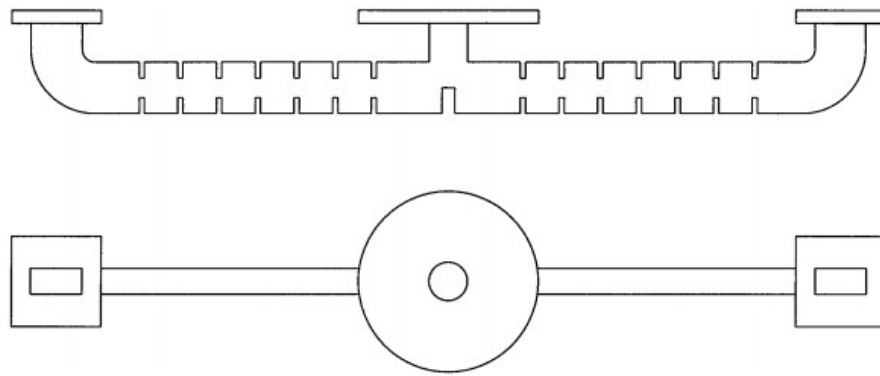
(a)
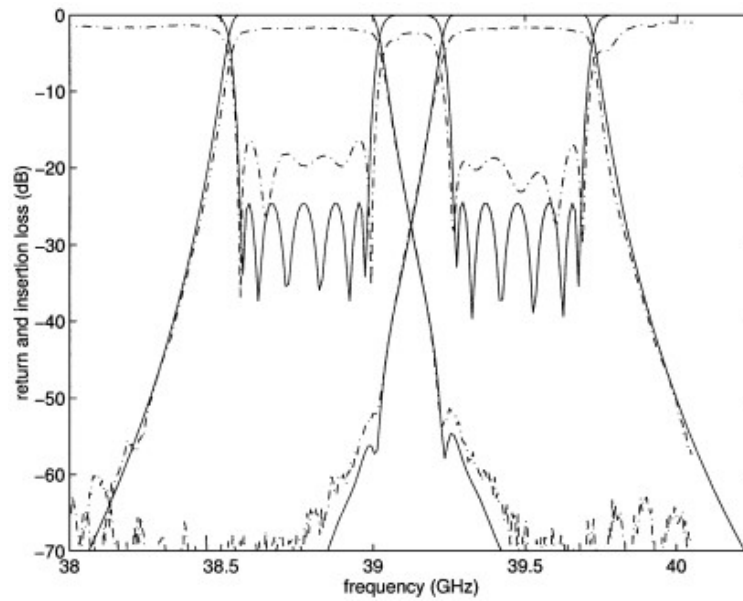


(b)

Fig. 1.9.   (a) Rectangular waveguide diplexer with a circular waveguide common port.

(b) Frequency responses of the diplexer.

## 1.3 Literature Review on Diplexers

As discussed in section 1.1, we know the diplexers are key components that are widely used in wireless systems, such as mobile communication and wireless area network systems. So, in the past decades, many diplexers based on various resonant structures were developed [45]-[56]. In general, these works can be divided into three categories.

   The first one is to adopt metal waveguide to design diplexers for higher power handle capability [45]-[47]. This is the most popular method in the early. Fig. 1.9(a) shows a diplexer implemented by waveguide technology. As shown, each channel has six resonant cavity and the couplings between two cavities are controlled by the different size of gap.
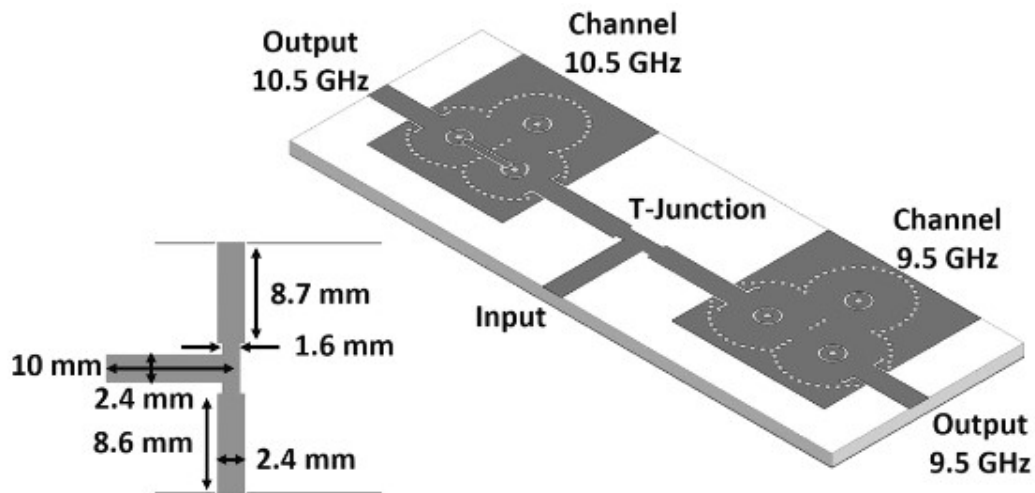
(a)
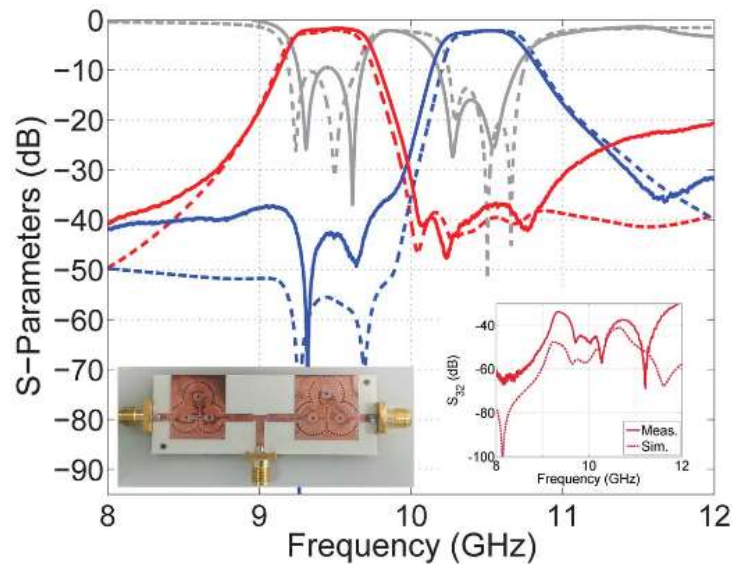


(b)

Fig. 1.10.   (a) Scheme of the diplexer using substrate integrated triplets in combline topology.
(b) Frequency responses of the diplexer.

T-junction with circular to rectangular waveguide structure is acted as the common input. Finally, a six-pole bandpass frequency responses for each channel has been obtained and the channel rejection for both are below 45 dB. As can be seen, diplexer design using the waveguide technique have the advantage of low loss, high selectivity and high power capacity, but the circuit size is large and it is difficult to integrate with other microwave circuits.

To integrate with other planar microwave circuit conveniently, the substrate integrated waveguide (SIW) technology, as the second method, was proposed and used to construct
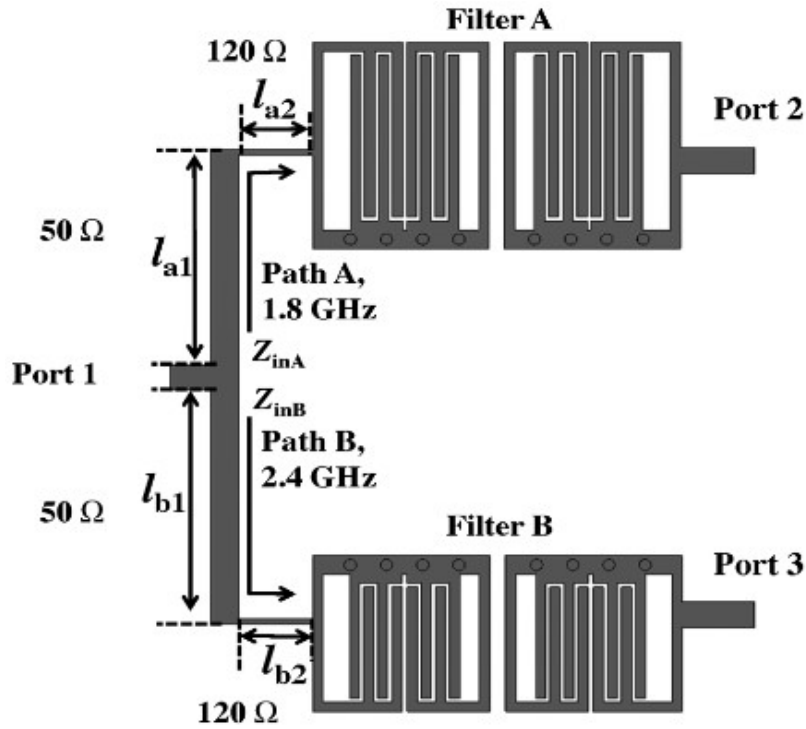
Fig. 1.11.    Configuration of the diplexer based on the hybrid resonators with T-junction.

diplexers [48]-[54]. SIW structure is fabricated by using two periodic rows of metallic vias connecting the top and bottom ground planes of a dielectric substrate and then behaves as the normal rectangular waveguide structure. Fig. 1.10 shows the scheme of one diplexer using substrate integrated triplets in combline topology and its frequency responses. The diplexer consists of two channel filters connected to a common input port through a microstrip T-junction. The filters are independently designed using three-pole circular substrate integrated coaxial resonator and coupling level to each filter is provided through a CPW current probe with two insets. SIW based diplexers have the advantage of high power handling, more compact size, and easier to integrated with other circuits than conventional waveguide technology. Nevertheless, the circuit size of the SIW based diplexers are still relatively large.

The third one is microstrip diplexer [55]-[60]. Microstrip diplexers take advantages of lighter weight, compact size, and better integration with other planar components. Thus, the microstrip diplexers are used more and more frequently in wireless system. The most intuitive design method of diplexer is the combination of two BPFs using a T-junction, as illustrated in Fig. 1.11. An optimized junction should be designed to ensure proper
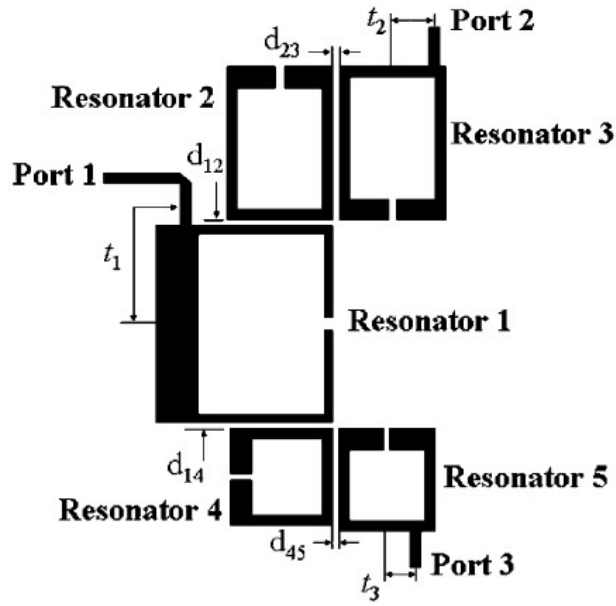
Fig. 1.12.    Configuration of the diplexer based on the stepped-impedance CR.
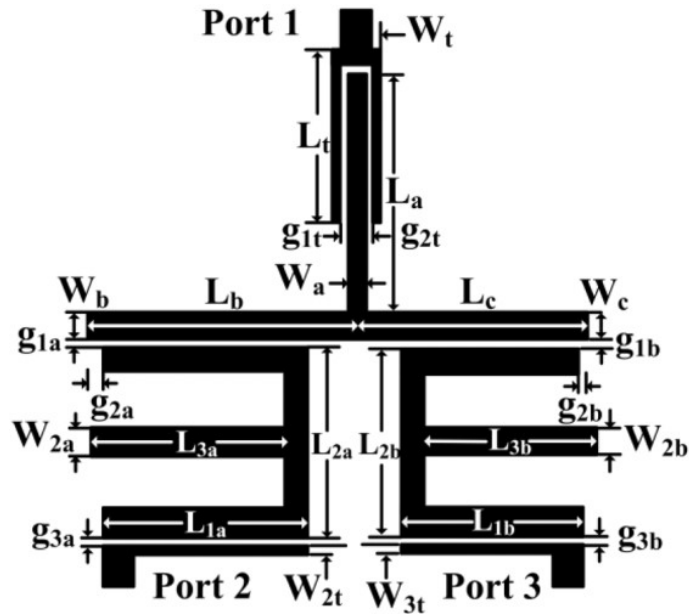


Fig. 1.13.    Configuration of the diplexer based on the stub-loaded CR.

impedance matching at either frequency [55], [56]. Common resonator (CR) technology that acts as an impedance matching network and a resonator for both channels is proposed to replace the input T-junction, as shown in Fig. 1.12. Various configurations of the CR have been studied [57]-[59]. Stepped-impedance resonators with controllable dual-resonant frequencies were designed as a CR [57]. However, it is difficult to realize the desired external couplings for both channels at one tap-position. In [58] and [59],
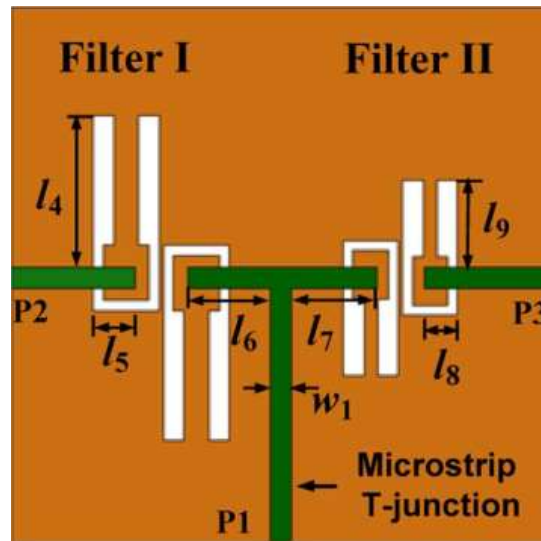
Fig. 1.14.   Configuration of the diplexer based on the slotline resonators.

diplexers employing a dual-mode stub-loaded microstrip resonator as CR were presented. Dual-resonance characteristics of the stub-loaded resonator were fully utilized and compact circuit size was achieved, as depicted in Fig. 1.13. In addition, the asymmetric transmission zeros (Tzs) technique are utilized to constitute the diplexer with the desired port isolation [60]. However, these designs are implemented by the microstrip line structures.

Recently, to make full use of the limited space in integrated circuit board, slotlines or defected ground structures etched on the ground plane are popular used in designing microwave diplexers [61]-[65]. As shown in Fig. 1.14, a compact diplexer is implemented by using slotline hairpin stepped impedance resonator in ground plane. The microstrip-slotline transition is used to split the signal to two channels without extra matching circuits and thereby economizes the circuit size.

## 1.4 Major Contributions of this Dissertation

The research outcome achieved in this doctoral dissertation represents the innovative design of microwave multi-band differential BPFs using the novel multimode resonators and development of the superconducting differential filters and the compact diplexer based on the hybrid resonant structure at the first time.

The major contributions of this dissertation are concluded and listed as follows:

(1) Proposed the quadruple-mode stepped-impedance square ring loaded resonator

(SRLR) and applied to constitute the compact dual-band differential BPF with two good DM passbands and deep CM suppression. Compared with the conventional SRLR, the impedance element, as the new design freedom, is used to adjust the frequency separation of DM resonances and CM resonances. On basis of the proposed quadruple-mode stepped-impedance SRLR, two more open-circuited stubs are added into the resonator and such that a sext-mode stepped-impedance SRLR is obtained. Then, a compact differential BPF is implemented by using the proposed sext-mode stepped-impedance SRLR.

(2) To reduce the insertion loss and improve the selectivity of passbands of the differential filter, high-order HTS multiband differential BPFs are firstly demonstrated in this dissertation. Two multimode resonators, i.e., modified SRLR and SSLR, which are the fully symmetric structure, have more flexible control of the internal coupling and allows themselves suitable for the design of high-order filters. For demonstration, a fourth-order and a eighth-order HTS dual-band differential BPFs are designed with high performance DM passbands and very deep CM suppression.

(3) Proposed the hybrid resonant structure firstly, which consists of a microstrip stub-loaded dual-mode resonator and a slotline stub-loaded dual-mode resonator, and adopted to construct a compact dual-band BPF and compact diplexer. The dual-modes of these two resonators are used to design separately the two passbands of the dual-band BPF and the diplexer. No matching network is required, which simplifies the design of the dual-band BPF and the diplexer, and reduces significantly the circuit size.

## 1.5 Organization of the Dissertation

Chapter 1 is an introductory that briefly describes the motivation and objective of the research of this dissertation. Besides, a literature review of multiband differential BPFs and diplexers are carried out.

Chapter 2 describes a simplified theory or concept for design of differential BPF and diplexer by using the multimode resonators. Then, basic design theory about HTS filter as well as the HTS materials and processing will be introduced.

Chapter 3 presents a newly quadruple-mode stepped-impedance SRLR and a sext-mode SRLR, and based of them, a compact dual-band differential BPF and a compact tri-band differential BPF are designed and implemented.

Chapter 4 introduces two new multimode resonators, which can be use to construct high-order dual-band differential BPF conveniently. For demonstration, a fourth-order HTS dual-band differential BPF and an eighth-order HTS dual-band differential BPF are designed, fabricated and measured to verify the proposed structure and design method.

Chapter 5 provides a new concept to design the compact diplexer simply. In this chapter, a slotline stub-loaded dual-mode resonator (SSLDR) and a microstrip stub-loaded dual-mode resonator (MSLDR) are proposed and discussed firstly and based of them, a compact diplexer with a desired isolation is designed.

Chapter 6 is a conclusion and recommendations for this dissertation.

# Chapter 2

# Fundamental Elements of Circuits Design and HTS Technology

## 2.1 Overview

For supporting the design of the microwave circuits in this dissertation, the required fundamentals will be presented in this chapter. From the studied of the generic model/block of differential filters and diplexers, it is found that the microwave filter is the common important part. Although the physical realization of microwave filters may vary, the circuit network and design theory are common to all. So, the understand and introduction of some concept and design theory of microstrip filter is the key point to develop the multi-band differential filters and diplexers in the following chapters. In addition, two high performance differential filters are designed and implemented based on the high temperature superconducting (HTS) technology. So, the fundamentals of HTS will be introduced in this chapter for readers to understand the unique property of HTS material, especially the mechanism of the extremely low loss.

## 2.2 Basic Models of Differential Filters and Diplexers

### 2.2.1 Basic Model of Differential Filters

Fig. 2.1 depicts the schematic of a generalized four port network of differential BPF, which consists of two pairs of feeding ports ($P_1$ & $P_1$' and $P_2$, $P_2$') and a filtering structure for realizing the desired frequency responses. As shown, the network is symmetric by dashed line AA'. So, the differential filters are always investigated by the well-known even- and odd-mode analysis method. The corresponding differential-mode (DM) bisection, behaves as a conventional bandpass filter, for bandpass frequency response and common-mode (CM) bisection, exhibits the conventional bandstop filter, for bandstop property can be obtained under respective odd-mode (in magnitude and out of phase) and
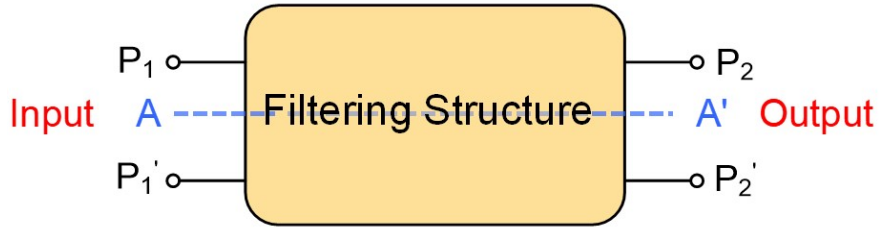
Fig. 2.1.　Four Port Network of Differential BPF.



(a)　　　　　　　　　　　　　　(b)
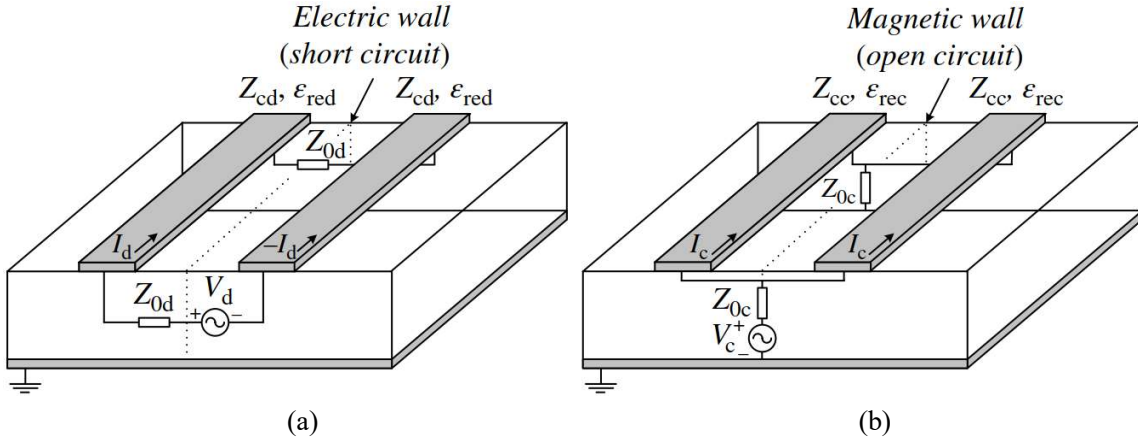
Fig. 2.2.　Voltages and currents in a differential microstrip line and generation of the (a) differential mode and (b) common mode.

even-mode (in magnitude and phase) excitation [2].

Since the differential filters presented in this dissertation are implemented in microstrip technology, the analysis on basic microstrip differential lines is provided for easier to be understand. Fig. 2.2 is an example of a three-wire differential line, implemented by means of a pair of coupled microstrip lines [3]. Such lines support two fundamental propagation modes: the DM and the undifferential mode. The differential mode is the fundamental mode, equivalent to the so-called odd mode, in which the line is driven differentially (in magnitude and out of phase). The undifferential mode, also called CM, is equivalent to the so-called even mode. In the CM, equal signals (in magnitude and phase) propagate at both individual lines. For the differential structure of Fig. 2.2, all these modes are quasi-TEM modes, provided the separation between the ground plane and the lines (substrate thickness) is very small as compared with the wavelength.

It is concluded that the differential and common modes are quasi-TEM modes equivalent to the odd and even mode, respectively. The difference between such modes comes just from signal definitions. In the differential and common modes, two
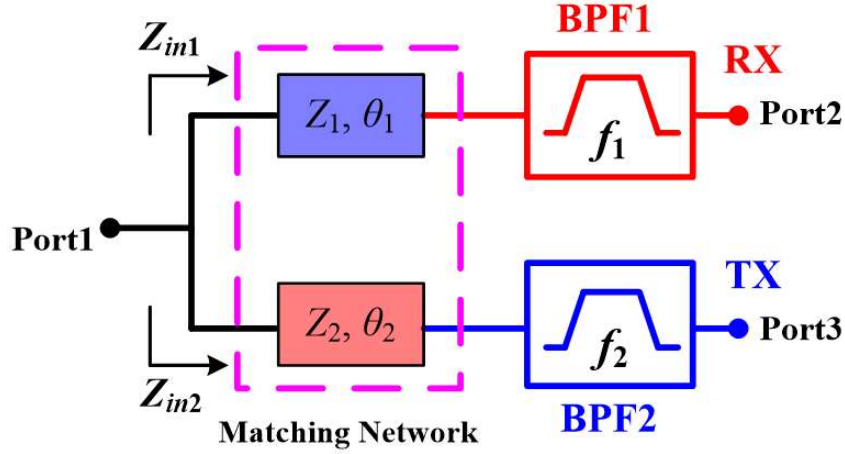
Fig. 2.3. Generic scheme of the diplexer.

single-ended ports are driven as a pair that is called composite port. Any single-ended signal pair applied to a composite port can be decomposed into its differential- and common-mode portions, which are equivalent (but not equal) to the odd and even portions, respectively. The decomposition of hybrid differential- and common-mode voltages and currents into its differential and common-mode portions is depicted in Fig. 2.2.

### 2.2.2 Basic Model of Diplexers

Microwave diplexers are typically employed to connect the receiver (RX) and transmitter (TX) filters of a transceiver to a single antenna through a suitable three port junction as shown in Fig. 2.3. An ideal diplexer should be the capability of satisfactory port matching, excellent filtering responses, and high isolation between TX and RX channel. And it tends to the development of high compactness, light weight, and multi-channel.

To obtain a satisfactory isolation between two links, the impedance-matching condition are as follows [40]:

$$Z_{in1}(f_1) = 50\,\Omega$$

$$Z_{in1}(f_2) = \infty$$

$$Z_{in2}(f_2) = 50\,\Omega \tag{2.1}$$

$$Z_{in2}(f_1) = \infty$$

that is: the input impedance $1(Z_{in1})$ of the RX channel at $f_1$ is 50 Ω but at $f_2$, $Z_{in1}$ is increase to infinity. At this time, TX signal can not be transmitted to receiving channel. Similarly, RX signal will be well prevented for the infinity input impedance of TX link at $f_1$ and, high isolation will be obtained. In general, the matching networks are commonly realized by the T-junction in manifold line type, such as the microstrip, coaxial, and waveguide, and common resonator for reducing circuit size on the one hand and providing one additional resonance and thereby improve the selectivity of passband on the other hand.

As discussed above, microwave filter is one of common important part of the both the differential filters and diplexers. So, in the following section, the basic concept and design theories of the conventional microwave BPFs will be given.

## 2.3 Fundamentals of Microwave Filters

Microwave filter, as a necessary and vial component in electronic systems, is used to select or reject signal at different frequencies. Although the physical realization of microwave filters may vary, the circuit network and design theory are common to all. They are, by nature, distributed networks that usually consist of periodic structures to exhibit passbands and stopband characteristics in various frequency bands.

### 2.3.1 General Definitions

In general, a filter is a two port network, as shown in Fig. 2.4. The transfer function of the two-port filter network is a mathematical description of network response characteristics, namely, a mathematical expression of $S_{21}$. On many occasions, an amplitude-squared transfer function for a lossless passive filter network is defined as [66]:

$$\left| S_{21}(w) \right|^2 = \frac{1}{1+\triangle^2 F_n^2(w)} \tag{2.2}$$

Where $\triangle$ is the ripple constant related to the passband return loss $L_R$. It is defined as

$$\triangle = \left[ 10^{L_R/10} - 1 \right]^{-1/2} \tag{2.3}$$

$F_n^2(w)$ represents a filtering or characteristic function. $w$ is a frequency variable.

For filter characterization, two parameters need to be defined:
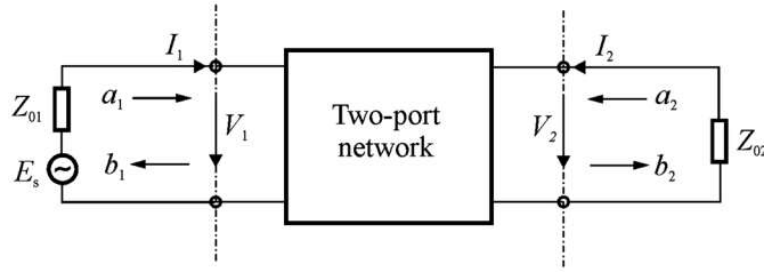
Fig. 2.4. Two-port network.

$$L_A = -20 \log |S_{21}| \quad dB \tag{2.4}$$

$$L_R = -20 \log |S_{11}| \quad dB \tag{2.5}$$

where $L_A$ denotes the insertion loss between ports 1 and 2 and $L_R$ represents the return loss at port 1.

## 2.3.2 Coupled Resonator Filters

Coupled resonator circuit prototype are most commonly used in the design of microwave coupled resonator bandpass filters in the that they can be applied to any type of resonator despite its physical structure. The design method is based on the coupling coefficients between two adjacent resonators and the external couplings of the input and output resonators. Therefore, a relationship between the coupling coefficients and the physical structures needs to be built.

Fig. 2.5 depicts the block diagram of microwave filter structure, in which $k_{n-1, n}$ indicates the coupling coefficient of the coupled resonator n-1 and resonator n and $Q_{exa}$ and $Q_{exb}$ represents the external quality factor of between the resonators at two resonator and the external feeding circuit.

Fig. 2.6 depicts the general model of two coupled resonators where resonators 1 and 2 can be different in structure and have different resonant frequencies. In general, the coupling coefficient may be defined on the basis of a ratio of coupled to stored energy as:

$$k = \frac{\iiint \varepsilon \vec{E}_1 \cdot \vec{E}_2 dv}{\sqrt{\iiint \varepsilon |\vec{E}_1|^2 \, dv \times \iiint \varepsilon |\vec{E}_2|^2 \, dv}} + \frac{\iiint \varepsilon \vec{H}_1 \cdot \vec{H}_2 dv}{\sqrt{\iiint \varepsilon |\vec{H}_1|^2 \, dv \times \iiint \varepsilon |\vec{H}_2|^2 \, dv}} \tag{2.6}$$
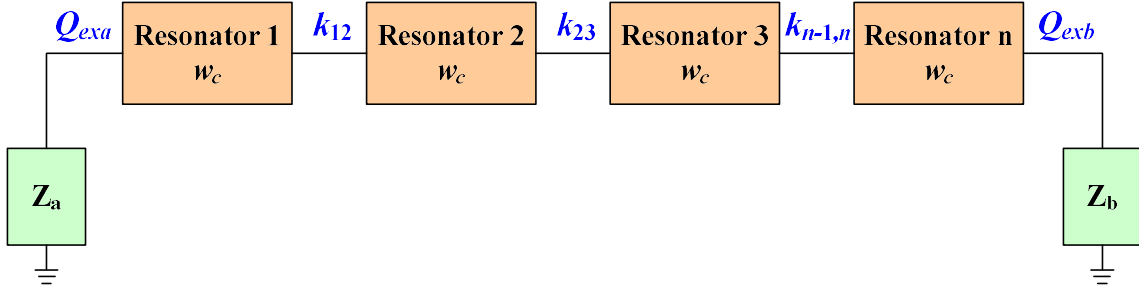
Fig. 2.5.    Block diagram of microwave filter structure.
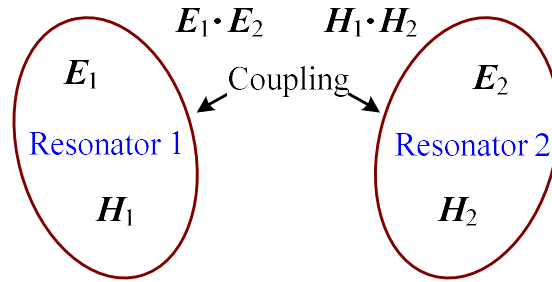


Fig. 2.6.    General model of two coupled resonators.

where where $E$ and $H$ represent the electric and magnetic field vectors, respectively [66]. Note that all fields are determined at resonance and the volume integrals are over entire effecting regions with permittivity of $\varepsilon$ and permeability of $\mu$. The first term on the right-hand side represents the electric coupling, while the second term represents the magnetic coupling. It should be remarked that the interaction of the coupled resonators is mathematically described by the dot operation of their space vector fields, which allows the coupling to have either positive or negative sign. The coupling coefficient can then be determined against the physical structure of coupled resonators if the relationship between the coupling coefficient and the characteristic frequencies is established.

For simplification, the lumped-element circuit models in three kinds of coupling type are shown in Fig. 2.7. Fig. 2.7(a) exhibits the equivalent lumped-element circuit model for electrically coupled resonators, where $L$ and $C$ are the self-inductance and self-capacitance, so that $(LC)^{-1/2}$ equals the angular resonant frequency of uncoupled resonators, and $C_m$ represents the mutual capacitance. After a series of derivation, the electric coupling coefficient $k_E$ can be found as
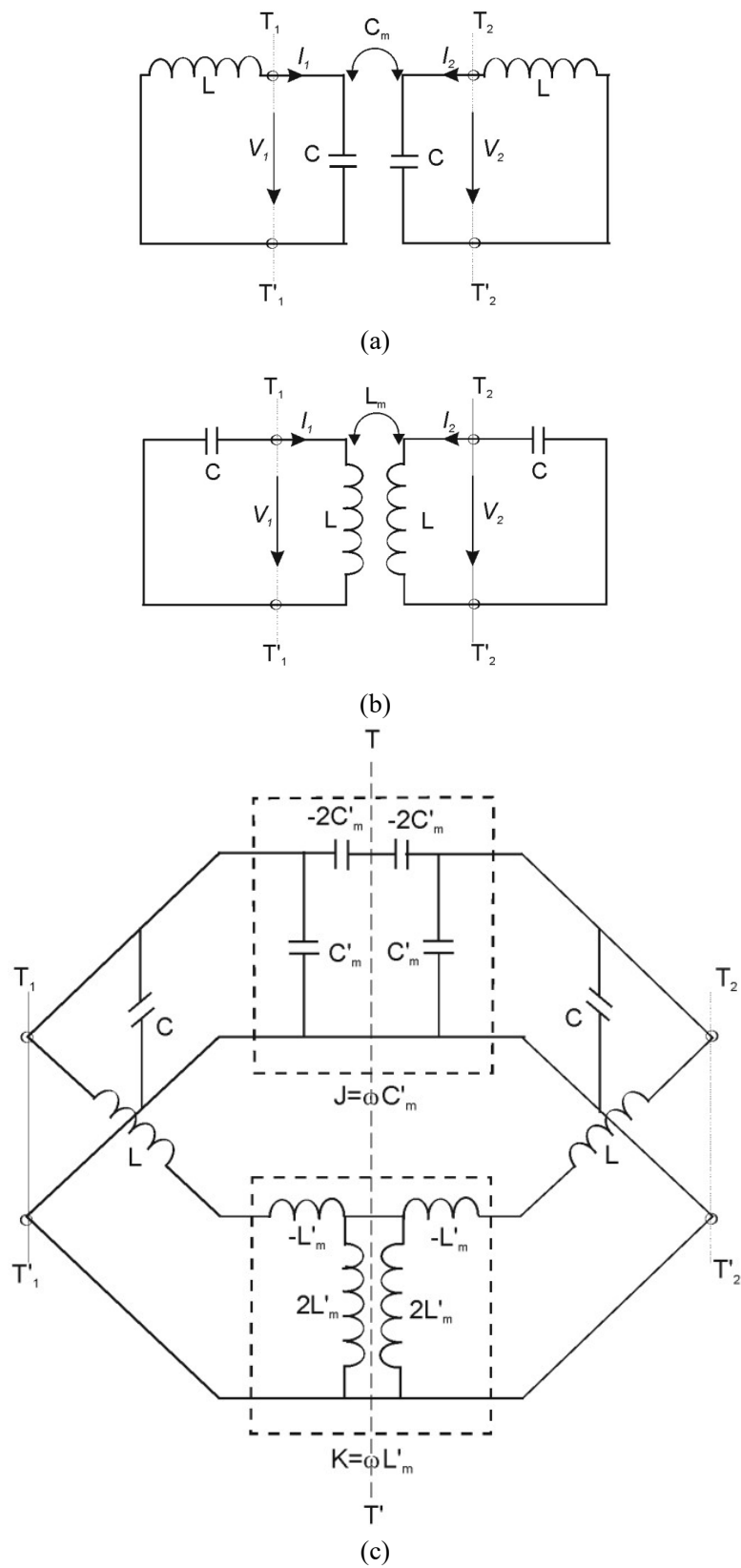
Fig. 2.7.   (a) Coupled resonator circuit with electric coupling. (b) Coupled resonator circuit with magnetic coupling. (c) Coupled resonator circuit with mixed electric and magnetic coupling.

$$k_E = \frac{f_m^2 - f_e^2}{f_m^2 + f_e^2} = \frac{C_m}{C} \qquad (2.7)$$

which is not only identical to the definition of ratio of the coupled electric energy to the stored energy of uncoupled single resonator, but also consistent with the coupling coefficient defined for coupled-resonator filter.

Fig. 2.7(b) shows the equivalent lumped-element circuit model for magnetically coupled resonator structures, where $L$ and $C$ are the self-inductance and self-capacitance, and $L_m$ represents the mutual inductance. Similarly, the magnetic coupling coefficient $k_E$ can be expressed as

$$k_M = \frac{f_m^2 - f_e^2}{f_m^2 + f_e^2} = \frac{L_m}{L} . \qquad (2.8)$$

For coupled-resonator structures, with both the electric and magnetic couplings, a network representation is given in Fig. 2.7(c), where $C$, $L$, $C_m'$, and $L_m'$ are the self-capacitance, the self-inductance, the mutual capacitance, and the mutual inductance. The mixed coupling coefficient $k_X$ can be found to be

$$k_X = \frac{f_e^2 - f_m^2}{f_e^2 + f_m^2} = \frac{CL_m' + LC_m'}{LC + L_m' C_m'} . \qquad (2.9)$$

It is reasonable to assume that $L_m'C_m' \ll LC$, and thus Eq. (2.9) becomes

$$k_X \approx \frac{L_m'}{L} + \frac{C_m'}{C} = k_M' + k_E' . \qquad (2.10)$$

which clearly indicates that the mixed coupling results from the superposition of the magnetic and electric couplings.

Then, after a series of derivation, the universal formulation for extracting the electric, magnetic, and mixed coupling coefficients in terms of the characteristic frequencies of both synchronously and asynchronously tuned coupled resonators as:
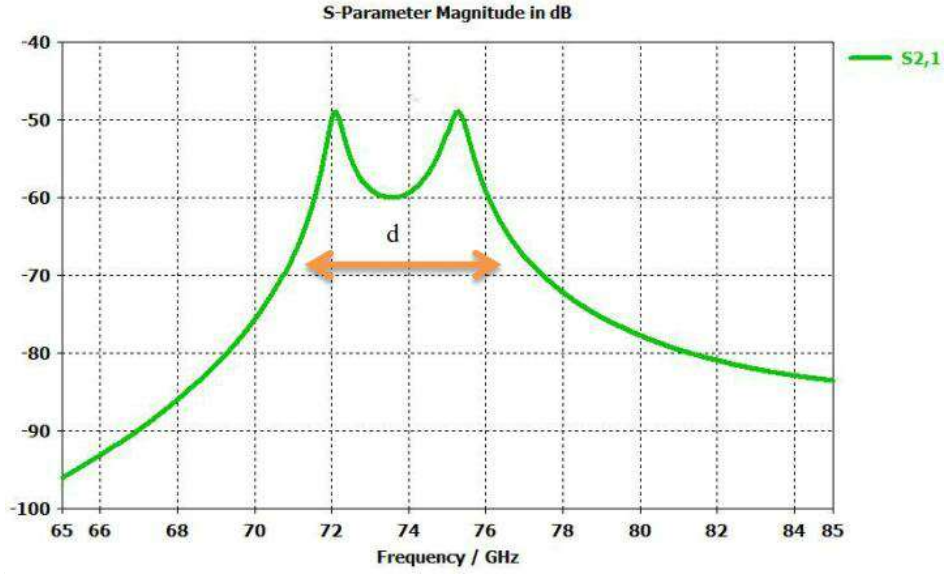
Fig. 2.8.    Frequency response of coupled resonator structure.

$$k = \pm \left( \frac{f_{02}}{f_{01}} + \frac{f_{01}}{f_{02}} \right) \sqrt{ \left( \frac{f_{p2}^2 - f_{p1}^2}{f_{p2}^2 + f_{p1}^2} \right)^2 - \left( \frac{f_{02}^2 - f_{01}^2}{f_{02}^2 + f_{01}^2} \right)^2 } \ . \tag{2.11}$$

Needless to say, the formulation is applicable for synchronously tuned coupled resonators as well and, in that case ($f_{01} = f_{02}$), it degenerates to

$$k = \pm \frac{f_{p2}^2 - f_{p1}^2}{f_{p2}^2 + f_{p1}^2} \ . \tag{2.12}$$

Comparing Eq. (2.12) with Eqs. (2.7), (2.8), and (2.9), it is noticed that $f_{p1}$ or $f_{p2}$ corresponds to either $f_e$ or $f_m$, and are the resonance peaks in the extraction of coupling coefficient by the simulated technique.

As shown in Fig. 2.8, there are two resonance peaks and the magnitude of the coupling coefficient defines the separation $d$ of the two resonance peaks. From Eq. (2.12), it is clearly that the stronger coupling the wider separation d of the two resonance peaks and deeper the trough in the middle.

## 2.3.3 Quality Factors of Microwave Filters

The quality factor $Q$ is useful measure of sharpness and energy loss of resonator circuit. It can be defined as [66]:
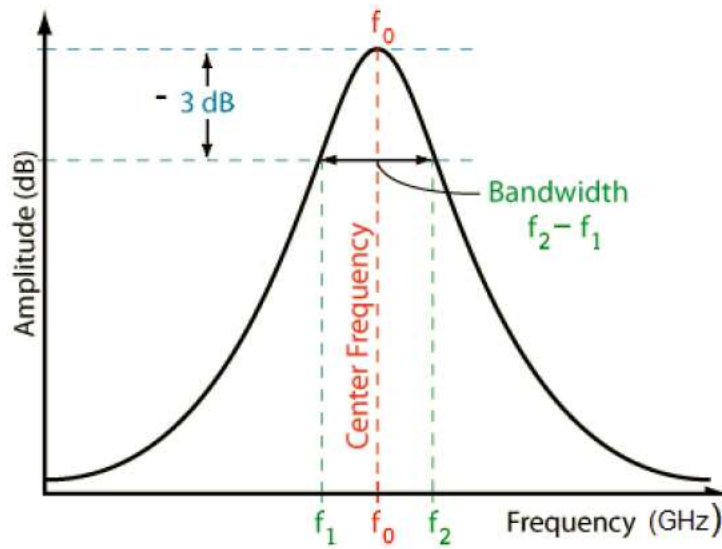
Fig. 2.9.   Scheme for extraction of quality factor.

$$Q = w \frac{\text{average energy stored}}{\text{average energy loss/second}}.$$ 

(2.13)

As can been from this definition, low loss implies a higher quality factor, $Q$.

External quality factor $Q_e$ can be defined in terms of resonance frequency f0 and bandwidth of the resonator circuit, which is expressed as

$$Q_e = \frac{f_0}{\triangle f}$$ 

(2.14)

where

$$\triangle f = f_2 - f_1.$$ 

(2.15)

A high $Q$ factor results in a steep roll-off and narrow bandwidth of the resonator as shown in Fig. 2.9.

## 2.3.4 Filter Design Procedure

In general, the development of a BPF is basis of the lowpass prototype filter. In general, a lowpass prototype filter is defined as a filter whose element values are normalized to make the source resistance or conductance equal to one, denoted by $g_0 = 1$, and the cutoff angular

frequency to be unity, denoted by $\Omega c = 1$ (rad/s). Fig. 2.10 demonstrates two
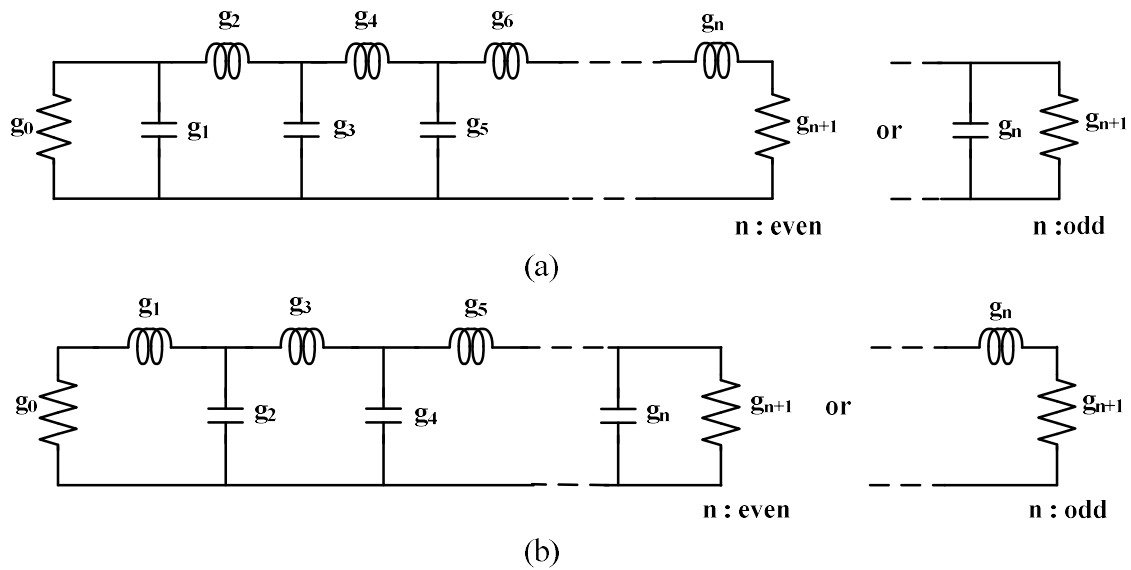


Fig. 2.10. Lowpass prototype filters for all-pole filters with

(a) a ladder network structure and (b) its dual..

possible forms of an n-pole lowpass prototype for realizing an all-pole filter response, including Butterworth, Chebyshev, and Gaussian responses. In this dissertation, all of design exhibits the Chebyshev frequency response. Therefore, Chebyshev lowpass prototype filters will be described in detail in the following.

## 2.3.4.1 Chebyshev Lowpass Prototype Filters

The response of a Chebyshev filter has an equal ripple in the passband and a maximally flat stopband. The element values for Chebyshev lowpass prototype networks shown in Fig. 2.10 can be computed for a given passband ripple $L_{Ar}$ dB and angular cutoff frequency of $\Omega c = 1$ (rad/sec) using the following equations [66]:

$$g_0 = 1.0$$

$$g_1 = \frac{2}{\gamma}\sin\left(\frac{\pi}{2n}\right)$$

$$g_i = \frac{1}{g_{i-1}} \frac{4\sin\left[\dfrac{(2i-1)\pi}{2n}\right] \cdot \sin\left[\dfrac{(2i-3)\pi}{2n}\right]}{\gamma^2 + \sin^2\left[\dfrac{(i-1)\pi}{n}\right]} \quad for\ i = 2, 3, ...n$$

(2.16)

$$g_{n+1} = \begin{cases} 1.0 & for\ n\ odd \\ \coth^2\left(\dfrac{\beta}{4}\right) & for\ n\ even \end{cases}$$

where

$$\beta = \ln\left[\coth\left(\frac{L_{Ar}}{17.37}\right)\right]$$

$$\gamma = \sinh\left(\frac{\beta}{2n}\right)$$

The order of the filter is determined according to the required specifications; such as the minimum stopband attenuation $L_{As}$ dB at $\Omega = \Omega s$ for $\Omega s > 1$ passband ripple $L_{Ar}$ dB. The order of Chebyshev lowpass prototype response is calculated by:

$$n \geq \frac{\cosh^{-1}\sqrt{\dfrac{10^{0.1L_{AS}} - 1}{10^{0.1L_{Ar}} - 1}}}{\cosh^{-1}\Omega_s}.$$

(2.17)

## 2.3.4.2 Bandpass Transformation

Assume that a lowpass prototype response is to be transformed to a bandpass response having a passband $\omega_2 - \omega_1$, where $\omega_1$ and $\omega_2$ indicate the passband-edge angular frequency. The required frequency transformation is

$$\Omega = \frac{\Omega_C}{FBW}\left(\frac{w}{w_0} - \frac{w_0}{w}\right)$$

(2.18)

$$L_S = \left(\frac{\Omega_c}{FBW\omega_0}\right)\gamma_0 g$$

$$C_S = 1/\left(\omega_0^2 L_S\right)$$

$$C_p = \left(\frac{\Omega_c}{FBW\omega_0}\right)\frac{g}{\gamma_0}$$

$$L_p = 1/\left(\omega_0^2 C_p\right)$$
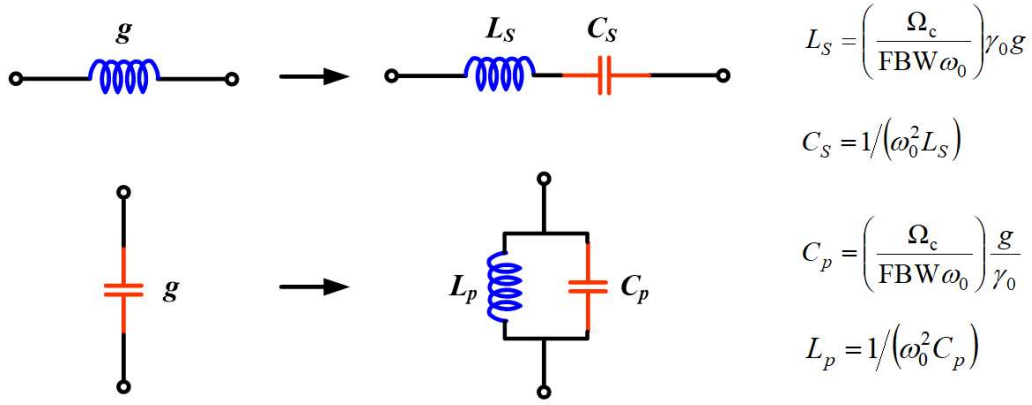
Fig. 2.11.   Basic element transformation from lowpass prototype to bandpass.

with

$$FBW = \frac{w_2 - w_1}{w_0}$$

$$w_0 = \sqrt{w_1 w_2}$$

where $\omega_0$ denotes the center angular frequency and FBW is defined as the fractional bandwidth. If we apply this frequency transformation to a reactive element g of the lowpass prototype, we have

$$j\Omega_s \rightarrow jw\frac{\Omega_c g}{FBW\omega_0} + \frac{1}{jw}\frac{\Omega_c w_0 g}{FBW} \tag{2.19}$$

which implies that an inductive/capacitive element *g* in the lowpass prototype will transform to a series/parallel LC resonant circuit in the bandpass filter. The elements for the series LC resonator in the bandpass filter are

$$L_s = \left(\frac{\Omega_c}{FBWw_0}\right)\gamma_0 g$$

$$C_s = \left(\frac{FBW}{\Omega_c w_0}\right)\frac{1}{\gamma_0 g}$$

for *g* representing the inductance     (2.20)

where the impedance scaling has been taken into account as well. Similarly, the elements for the parallel LC resonator in the bandpass filter are

$$C_p = \left( \frac{\Omega_c}{FBWw_0} \right) \frac{g}{\gamma_0}$$
$$L_p = \left( \frac{FBW}{\Omega_c w_0} \right) \frac{\gamma_0}{g}$$
for $g$ representing the capacitance (2.21)

It should be noted that $\omega_0 L_s = 1/(\omega_0 C_s)$ and $\omega_0 L_p = 1/(\omega_0 C_p)$ hold in Equation 2.10. The element transformation, in this case, is shown in Fig. 2.11.

### 2.3.4.3 Prototype k and q Values

Define k and q as prototype values, where k represents coupling between two resonators, and q represents the external coupling. The q prototype values can be derived from prototype g vales as follows:

$$q_1 = g_0 g_1 \tag{2.22}$$

$$q_n = \begin{cases} g_n g_{n+1} & \text{for } n \text{ odd} \\ g_n / g_{n+1} & \text{for } n \text{ even} \end{cases} \tag{2.23}$$

where $q_1$ and $q_n$ are related to the input and output coupling respectively. The prototype value is derived from prototype $g$ values as follows:

$$K_{ij} = k_{ij} \frac{BW}{f_0} \tag{2.24}$$

$$Q_1 = q_1 \frac{f_0}{BW} \qquad Q_n = q_n \frac{f_0}{BW} \tag{2.25}$$

where $f_0$ is the resonant frequency of the bandpass filter and BW is the absolute bandwidth. $Q_e$ is known as the external quality factor, and the external coupling coefficient is equal to

$$K_e = \frac{1}{Q_e} \tag{2.26}$$

$$Q_{ea} = \frac{g_0 g_1}{FBW}, \quad Q_{eb} = \frac{g_n g_{n+1}}{FBW} \tag{2.27}$$

and the coupling between resonator is

$$K_{C_k} = \frac{FBW}{\sqrt{g_k g_{k+1}}} \qquad (2.28)$$

$$FBW = \frac{BW}{f_0} . \qquad (2.29)$$

## 2.4 Fundamentals of HTS Technology

### 2.4.1 Characteristics of HTS Materials

Superconductors are materials that exhibit a zero intrinsic resistance to direct current flow when cooled below a certain temperature. The temperature at which the intrinsic resistance undergoes an abrupt change is referred to as the critical temperature or transition temperature, denoted by $T_c$. For alternating current flow, the resistance does not go to zero below $T_c$, but increases with increasing frequency. However, at typical RF/microwave frequencies, the resistance of a superconductor is perhaps one thousandth of that in the best ordinary conductor. It is certainly low enough to significantly improve performances of RF/microwave microstrip filters.

Superconductors were first discovered in 1911 [67], for almost 75 years after the discovery, all known superconductors required a very low transition temperature, say 30 Kelvin (K) or lower, which limit the applications of these early superconductors. A revolution in the field of superconductivity occurred in 1986 with the discovery of the superconductors with transition temperature greater than 77K, the boiling point of liquid nitrogen [68]. These superconductors are, therefore, referred to as the high-temperature superconductors. The discovery of the HTS made possible many practical applications of superconductivity. Since then, the development of microwave applications has proceeded vary rapidly, particularly HTS microstrip filters.

The growth of HTS films and the fabrication of HTS microstrip filters are compatible with hybrid and monolithic microwave-integrated circuits. Although there are many hundreds of high-temperature superconductors with varying transition temperatures, yttrium barium copper oxide (YBCO) is the most popular and commercially available HTS material, which typical transition temperatures is 92K.

**Super current**

$J_s$    $\sigma_2$

$J$

$J_n$    $\sigma_1$

**Normal current**
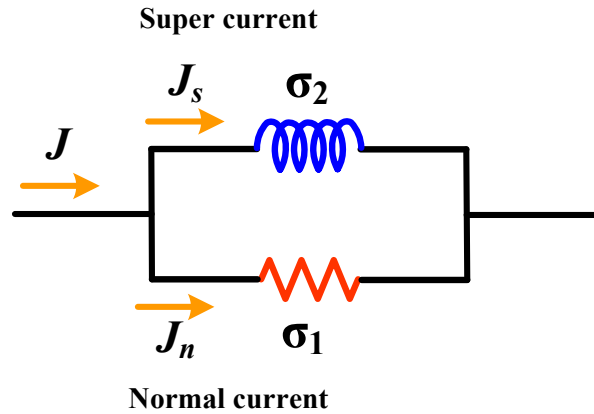
Fig. 2.12.    Simple circuit model depicting complex conductivity.

## 2.4.1.1 Penetration Depth

Superconductivity may be explained as a consequence of paired and unpaired electrons travelling with the lattice of a solid. It is possible to model the superconductor in terms of a complex conductivity $\sigma_1 - j\sigma_2$, such a model is called the two-fluid model.

Fig.2.12 depict a simple equivalent circuit, which describes complex conductivity in a superconductor. $J$ denotes the total current density and $J_s$ and $J_n$ are the current densities carried by the paired and normal electrons, respectively. The total current in the circuit is split between the reactive inductance and the resistance, which represents dissipation. As frequency decreases, the reactance becomes lower and more of the current flows through the inductance. When the current is constant, this inductance completely shots the resistance, allowing resistance-free current flow.

As a consequence of the two-fluid mode, the complex conductivity may be given by

$$\sigma = \sigma_1 - j\sigma_2 = \sigma_n \left(\frac{T}{T_C}\right)^4 - j\frac{1}{w\mu\lambda^2}\left[1 - \left(\frac{T}{T_C}\right)^4\right] \qquad (2.30)$$

where $\sigma_n$ is the normal state conductivity at $T_c$ and $\lambda_0$ is a constant parameter. Note that the calculation of Eq. (2.30) is not strictly valid close to $T_c$.

Normally the approximation $\sigma_2 >> \sigma_1$ can be made for good quality superconductors provided that the temperature is not too close to the transition temperature, where more normal electrons are present. Making this approximation, an important parameter called the penetration depth, based on the two-fluid model, is given by

$$\lambda = \frac{1}{\sqrt{w\mu\sigma_2}} \tag{2.31}$$

Substituting $\sigma_2$ from Eq. (2.30) into (2.31) yields

$$\lambda = \frac{\lambda_0}{\sqrt{1 - \left(\dfrac{T}{T_C}\right)^4}}. \tag{2.32}$$

Thus, $\lambda_0$ is actually the penetration depth as the temperature approaches zero Kelvin. Depending on the quality of superconductors, a typical value of $\lambda_0$ is about 0.2μm for HTS. The penetration depth is actually defined as a characteristic depth at the surface of the superconductor such that an incident plane wave propagated into the superconductor is attenuated by $e^{-1}$ of its initial value. It is analogous to the skin depth of normal conductors, representing a depth to which electromagnetic fields penetrate superconductors, and it defines the extent of a region near the surface of a superconductor in which current can be induced. The penetration depth $\lambda$ is independent of frequency, but will depend on temperature, as can be seen from Eq. (2.32). This dependence is different from that of the skin depth of normal conductors.

As with planar microwave devices using normal conductors, best performance control is obtained when the geometric inductance of the circuit dominates the internal inductance of the superconductor. That is, from a practical point of view, the thickness of the superconductor must be at least two to three times larger than the penetration depth at the temperature of operation.

Another distinguished feature of superconductors is that a dc current or field cannot fully penetrate them. This is quite unlike normal conductors, in which there is full penetration of the dc current into the material. As a matter of fact, a dc current decays from the surface of superconductors into the material in a very similar way to an ac current, namely, proportional to $e^{-z/\lambda_L}$, where $z$ is the coordinate from the surface into the material and $\lambda_L$ is the London penetration depth. Therefore, $\lambda_L$ is a depth where the dc current decays by an amount $e^{-1}$ compared to the magnitude at the surface of superconductors. In the two-fluid model, the value of the dc superconducting penetration depth $\lambda_L$ will be the same as that of the ac penetration depth $\lambda$ given in Equation 2.21 with $\lambda$ being independent of frequency.

## 2.4.1.2 Surface Impedance

The surface impedance of a conductor is the characteristic impedance seen by a plane-wave incident perpendicularly on a planar superconducting surface. The surface impedance is also an important parameter for superconducting materials. In general, solving Maxwell's equation for a uniform plane wave in a metal of conductivity $\sigma$ yields a surface impedance given by

$$Z_s = \frac{E_t}{H_t} = \sqrt{\frac{jw\mu}{\sigma}} \tag{2.33}$$

where $E_t$ and $H_t$ are the tangential electric and magnetic fields at the surface. This definition of the surface impedance is general and applicable for superconductors as well. For superconductors, replacing $\sigma$ by $\sigma_1 - j\sigma_2$ gives

$$Z_s = \sqrt{\frac{jw\mu}{\sigma_1 - j\sigma_2}} \tag{2.34}$$

whose real and imaginary parts can be separated, resulting in

$$Z_s = R_s + jX_s = \frac{\sqrt{w\mu}}{2}\left(\frac{\sqrt{k+\sigma_1}-\sqrt{k-\sigma_1}}{k}+\frac{\sqrt{k-\sigma_1}-\sqrt{k+\sigma_1}}{k}\right) \tag{2.35}$$

with $k = \sqrt{\sigma_1^2 + \sigma_2^2}$. Using the approximations that $k \approx \sigma_2$ and $\sqrt{1 \pm \sigma_1/\sigma_2} \approx 1 \pm \sigma_1/(2\sigma_2)$ for $\sigma_2 >> \sigma_1$, and replacing $\sigma_2$ with $(\omega\mu\lambda^2)^{-1}$, we arrive at

$$R_s = \frac{w^2\mu^2\sigma_1\lambda^3}{2} \quad \text{and} \quad X_s = w\mu\lambda. \tag{2.36}$$

For the two-fluid model, the surface resistance $R_s$ will increase as $\omega^2$ when $\sigma_1$ and $\lambda$ are independent of frequency. $R_s$ will depend on temperature as well. Figure 2.10 illustrates typical temperature-dependent behaviors of $R_s$, where $R_0$ is a reference resistance. The surface reactance in Equation 2.24 may also be expressed as $X_s = \omega L$, where the inductance $L = \mu\lambda$ is called the internal or kinetic inductance. The significance of kinetic inductance
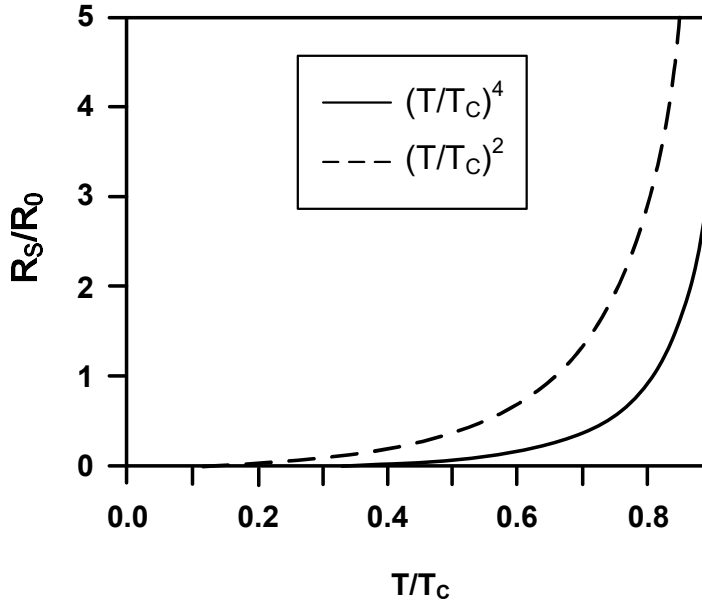
Fig. 2.13.   Temperature dependence of surface resistance of superconductor.

lies in its temperature dependence, which will mainly account for frequency shifting of superconducting filters against temperature.

The surface impedance described above is actually for an infinite thick film; it can be modified in order to take the finite thickness of the film into account. If $t$ is the thickness of the film then its surface impedance is

$$Z_f = R_s \left\{ \coth\left(\frac{t}{\lambda}\right) + \frac{t}{\lambda} \frac{1}{\sinh^2\left(\frac{t}{\lambda}\right)} \right\} + jX_s \coth\left(\frac{t}{\lambda}\right) \tag{2.37}$$

where $R_s$ and $X_s$ are given by Eq. (2.36). Again $\sigma_2 >> \sigma_1$ is assumed in the derivation of the expression. The effect of the finite thickness of thin film tends to increase both the surface resistance and the surface reactance of thin film. Based on published studies, we know that in order to reduce the thin film surface resistance, the thin film thickness should be greater than three to four times the penetration depth, as shown in Fig. 2.14. This is similar to the requirement for normal conductor thin film microwave devices, where the conductor thickness should at least three to four times thicker than the skin depth. The HTS film must be at least 500 nm to 600 nm thick for operation at 77 K, in order for the kinetic inductance effects to be negligible with respect to the total inductance of the circuit.
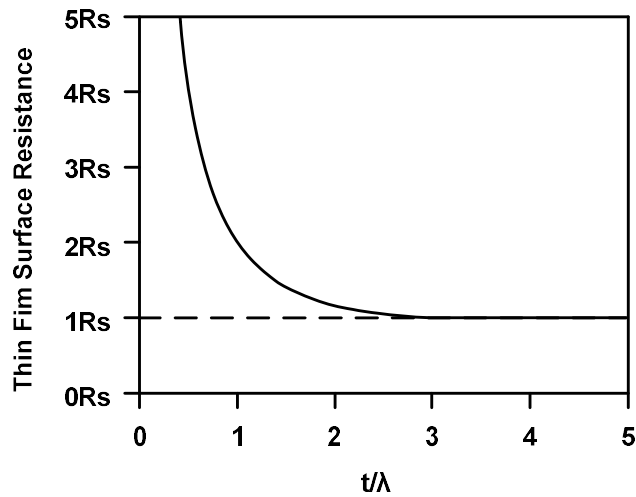
Fig. 2.14.   Surface resistance of superconducting thin films as a function of normalized thickness.

For a normal conductor, the surface resistance and surface reactance are equal and are given by

$$R_s = X_s = \sqrt{\frac{w\mu}{2\sigma_n}} \; . \tag{2.26}$$

Both are proportional to the square root of frequency. The surface resistance of a superconductor increases more rapidly (as frequency squared). Based on published studies, we can know that at 2 GHz the surface resistance of HTS thin film at 77 K is a thousand times smaller than that of copper at 300 K.

## 2.4.2   Substrates for Superconductors

Superconducting films have to be grown on some sort of substrate that must be inert, compatible with both the growth of good quality film, and also have appropriate microwave properties for the application at hand. In order to achieve good epithelial growth, the dimensions of the crystalline lattice at the surface of the substrate should match the dimensions of the lattices of the superconductors. If this is not the case, strain can be set up in the films, producing dislocations and defects. In some cases, the substrates can react chemically, causing impurity levels to rise and the quality of the film to fall. Cracks can be caused in the film if the thermal expansions of the substrate and film are not appropriately matched. Some of the above problems can be overcome by the application of a buffer layer between the films and the substrates. In addition, the surface of substrates

Table 2.1 Substrates for HTS films

| Substrate | $\varepsilon_r$ (typical) | tan $\delta$  (typical) | Comments |
|-----------|--------------|-----------------|----------|
| LaAlO$_3$ | 24.2 @ 77K | $7.6 \times 10^{-6}$  @ 77K and 10GHz | high miniaturisation, loss tangent maximum at 77K |
| MgO | 9.6 @ 77K | $5.5 \times 10^{-6}$  @ 77K and 10GHz | brittle, hygroscopic |
| Sapphire | 11.6 ‖ $c$-axis @ 77K  9.4 ‖ $c$-axis @ 77K | $1.5 \times 10^{-8}$  @ 77K and 10GHz | mechanically strong, low cost, anisotropic |

should be smooth and free from defects and twinning, if possible. These cause unwanted growth and mechanisms that can lead to non-optimal films. For microwave applications, it is of fundamental importance that the substrates have a low dielectric loss tangent (tan$\delta$). If the loss tangent is not low enough, then the advantage of using a superconductor can be negated. It is also desirable that the dielectric constant ($\varepsilon_r$) of a substrate not change much with temperature in most applications, improving the temperature stability of the final applications. Whatever the dielectric constant, it must be reproducible and not change appreciably from batch to batch.

With all the above requirements, it is not surprising that an ideal substrate for HTS films has not been found yet. Nevertheless, a number of excellent substrates, producing high-quality films with good microwave properties, are in common use. Among these, the most widely used and commercially available substrates are the lanthanum aluminate (LaAlO$_3$), magnesium oxide (MgO), and sapphire (Al$_2$O$_3$). LaAlO$_3$ has a higher dielectric constant than MgO and sapphire, but is generally twinned. Sapphire is a low-loss and low-cost substrate, but its dielectric constant is not isotropic and it requires a buffer layer for grow good HTS films. MgO is a very good substrate for applications, but is mechanically brittle. Table 2.1 lists some typical parameters of these substrates. For a sapphire substrate, the values of relative dielectric constant that are given are for both parallel and perpendicular to the $c$-axis (crystal axis) because of anisotropy. The HTS YBCO films fabricated on a 0.5-mm thick MgO substrates with a relative dielectric constant of 9.78 are chosen for our filter design.

## 2.4.3  Device Processing

The patterning of the device can be achieved with conventional photolithography. After photolithography, YBCO can be removed by wet etching with diluted phosphorous acid or

by ion milling [71]. The processing may include the deposition and patterning of low-resistivity contacts for interfacing with other devices or instrumentation. These are typically made by depositing a thin (200 nm to 300 nm) layer of gold or silver through a shadow mask on the contact areas [72]. Another possibility is to deposit a layer of gold or silver over the whole HTS film and then selectively remove the metal in the photolithographic process. The latter option allows for an in situ-deposition of the metal in the same chamber where the HTS film is grown, without breaking vacuum, favoring a low-resistance contact between the HTS and the metal. Interfacing with other devices via coaxial connectors or directly to other substrates, superconducting or otherwise, can be accomplished using gold wire or ribbon attached to the low-resistivity contacts by ultrasonic thermal compression bonding or gap-welding (ribbons). Fabrication details of filters and delay lines made at Northrop Grumman can be found in [73]. Other institutions follow similar procedures. The filter here was fabricated by a standard photolithograph and ion milling process.

## 2.5 Conclusion

This chapter describes some basic concepts and theories that form the foundation for design of microstrip differential filters, high-order HTS differential filters, and compact diplexers. The topics will cover the basic models of microwave differential filters and diplexers, lowpass prototype filters and elements, BPF frequency and element transformations and the basic HTS design procedure. This chapter also introduces some fundamentals of HTS technology. It covers some important properties of superconductors and substrates for growing HTS films, which are essential for the design of HTS microstrip filters. Basic concepts and theories of filters in this chapter provide an effective method for high-performance miniaturized multi-band microstrip differential filters, high-order HTS differential BPFs, and diplexers design.

# Chapter 3

# Multi-Band Differential Bandpass Filters Based on SI-SRLRs

## 3.1 Overview

From the above two chapters, it is known that differential bandpass filters (BPFs) play an important role in modern communication systems for their good common-mode (CM) rejection capability, which results in a higher immunity to the environmental noise and electromagnetic interference. With the continuous appearance of various wireless equipments having multi-functional services, multi-band differential BPFs are highly desired. According to the literature review on differential BPFs in section 2.2, we obtained that there are several typical methods to construct multi-band differential BPFs, one of them is adopting multimode resonator for achieving a compact size.

Recently, a quadruple-mode square ring loaded resonator (SRLR) is proposed for multi-band filter design [74], as shown the structure of SRLR in Fig. 3.1. All line widths of SRLR are assumed equal for analysis simplicity, resulting in a limitation of design freedom. To improve the design flexibility, an additional open stub loaded on the center of square ring in [75] or disperse technique used in [76] are conducted. Nevertheless, a favorable frequency disparity between two adjacent even-mode and odd-mode of the afore-presented resonators is not easy to achieve, which is disadvantaging to construct a differential filter with a desired CM
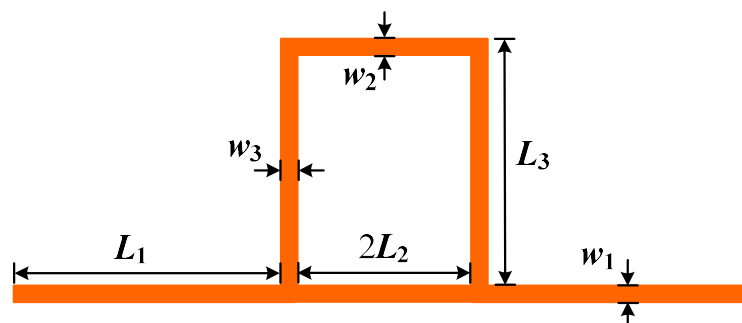


Fig. 3.1    Configuration of SRLR

suppression.

In this chapter, stepped-impedance technique is firstly applied to the conventional SRLR for improving the design flexibility and such that a newly quadruple-mode stepped- impedance SRLR (SI-SRLR) is obtained. Then, two additional open-circuited stubs are loaded at upper two corners of square ring of the proposed SI-SRLR and two more resonant modes are thereby generated. Thus, another newly multimode resonator, named sext-mode SI-SRLR, is obtained. Based on these two multimode SI-SRLRs, high-performance a dual-band differential BPF and a tri-band differential BPF are developed, respectively. Resonant characteristics of these two multimode SI-SRLRs are investigated by the even-/odd-mode method and simulation techniques. Two/three differential-modes (DMs) of SI-SRLR are used to form the dual/triple differential passbands. The admittance ratio $K$ of SI-SRLR is chosen appropriately to prevent the common-mode (CM) interference with DM operations. Moreover, frequency discrepancy by loading open-circuited stubs is used to enhance the CM suppression. In addition, multiple transmission zeros are produced to improve significantly the frequency selectivity of DM passbands. Finally, two compact multi-band differential BPFs are designed, fabricated and measured to verify the proposed structure and design method.

## 3.2 Dual-Band Differential Bandpass Filters Based on Quadruple-Mode SI-SRLR

### 3.2.1 Analysis of Quadruple-Mode SI-SRLR

#### 3.2.1.1 Configuration and Equivalent Circuit of SI-SRLR

The configuration of the proposed microstrip quadruple-mode SI-SRLR is depicted in Fig. 3.2. It consists of a one-wavelength stepped-impedance ring resonator loaded with two open-circuited stubs, which is different from the one-wavelength uniform-impedance ring resonator adopted in [74]-[76]. $L_1$ to $L_3$ and $w_1$ to $w_4$ denote the physical lengths and widths of the corresponding microstrip line segments, respectively. In light of the demonstrations in [76], the equivalent transmission line model (TLM) of the proposed SI-SRLR is also built for property analysis. TLM is shown in Fig. 3.3(a). This circuit consists of six transmission-line sections, with corresponding electrical lengths and characteristic admittances as $\theta_1$, $2\theta_2$, $\theta_3$, and $Y_1$, $Y_2$, $Y_3$, $Y_4$, respectively. Here, $\theta_1 = \beta L_1$, $\theta_2 = \beta L_2$, $\theta_3 = \beta L_3$, and $\beta$ is the propagation
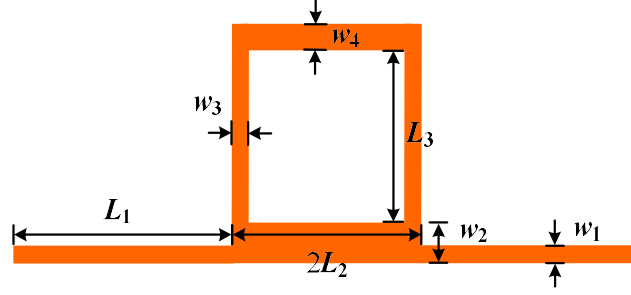
Fig. 3.2    Geometry of the proposed quadruple-mode SI-SRLR.
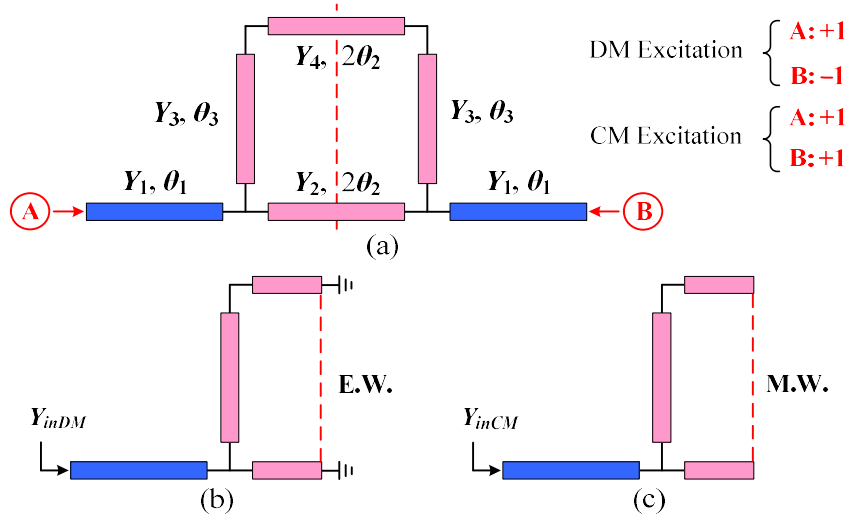


Fig. 3.3    (a) Transmission line model of the proposed quadruple-mode SI-SRLR.
(b) DM equivalent circuit. (b) CM equivalent circuit.

constant of the microstrip line.

## 3.2.1.2 Characteristics of DM and CM Bisection

Since the circuit in Fig. 3.3(a) is a symmetric structure, it can be readily analyzed by using the well-known even- and odd-mode method, as conducted in [76]. In the case of even-mode excitation, the symmetrical plane of the circuit is an electrical wall (E.W.), and the circuit is simplified as shown in Fig. 3.3(b). For the odd-mode excitation, the symmetrical plane is a magnetic wall (M.W.), and the simplified circuit is given in Fig. 3.3(c).

The input admittance of the DM or CM equivalent circuit, $Y_{in, DM \text{ or } CM}$, can be derived as

$$Y_{in, DM \& CM} = Y_1 \frac{Y_L + jY_1 \tan \theta_1}{Y_1 + jY_L \tan \theta_1} \tag{3.1}$$

where
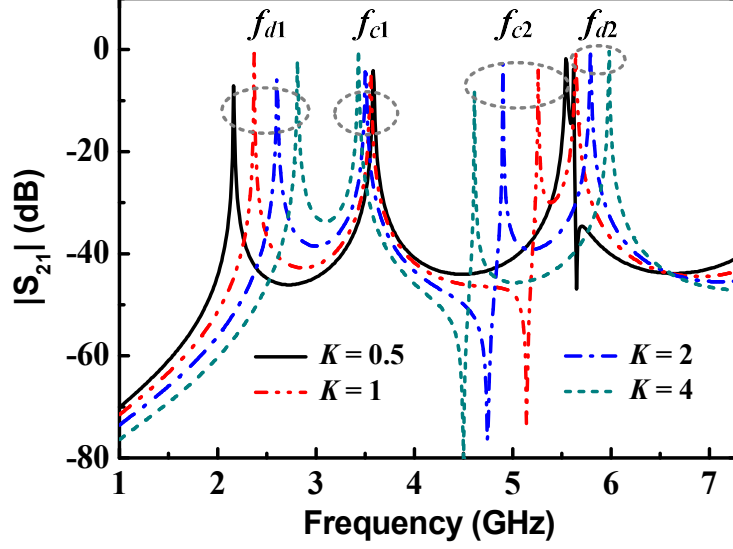
Fig. 3.4    Frequency responses of the SI-SRLR with different values of the admittance ratio $K$.

$$Y_L = \begin{cases} jY_3 \dfrac{Y_3 \tan\theta_3 - Y_4 \cot\theta_2}{Y_3 + Y_4 \cot\theta_2 \tan\theta_3} - jY_2 \cot\theta_2, & DM\ case \\[4mm] jY_3 \dfrac{Y_3 \tan\theta_3 + Y_4 \tan\theta_2}{Y_3 - Y_4 \tan\theta_3 \tan\theta_2} + jY_2 \tan\theta_2, & CM\ case \end{cases} \tag{3.2}$$

From the resonant condition of $Y_{in,\ DM\ or\ CM} = 0$, the DM and CM resonant frequencies can be deduced as follows:

$$\begin{aligned} &Y_3(Y_3 \tan\theta_3 - Y_4 \cot\theta_2) + (Y_1 \tan\theta_1 - Y_2 \cot\theta_2) \\ &\times (Y_3 + Y_4 \tan\theta_3 \cot\theta_2) = 0, \quad DM\ case \end{aligned} \tag{3.3a}$$

$$\begin{aligned} &Y_3(Y_3 \tan\theta_3 + Y_4 \tan\theta_2) + (Y_1 \tan\theta_1 + Y_2 \tan\theta_2) \\ &\times (Y_3 - Y_4 \tan\theta_3 \tan\theta_2) = 0, \quad CM\ case \end{aligned} \tag{3.3b}$$

For simplification, let $Y_1 = Y_3 = Y_4$, $\theta_1 = 2\theta_2$, and define $K = Y_2/Y_1$. Thus, (3) can be reformulated as

$$\begin{aligned} &\left( \tan\theta_3 - \cot(\theta_1/2) \right) + \left( \tan\theta_1 - K \cot(\theta_1/2) \right) \\ &\times \left( 1 + \tan\theta_3 \cot(\theta_1/2) \right) = 0, \quad DM\ case \end{aligned} \tag{3.4a}$$

$$\begin{aligned} &\left( \tan\theta_3 + \tan(\theta_1/2) \right) + \left( \tan\theta_1 + K \tan(\theta_1/2) \right) \\ &\times \left( 1 - \tan\theta_3 \tan(\theta_1/2) \right) = 0, \quad CM\ case \end{aligned} \tag{3.4b}$$

It is obvious from (3.4) that both the DM resonant frequencies and the CM resonant
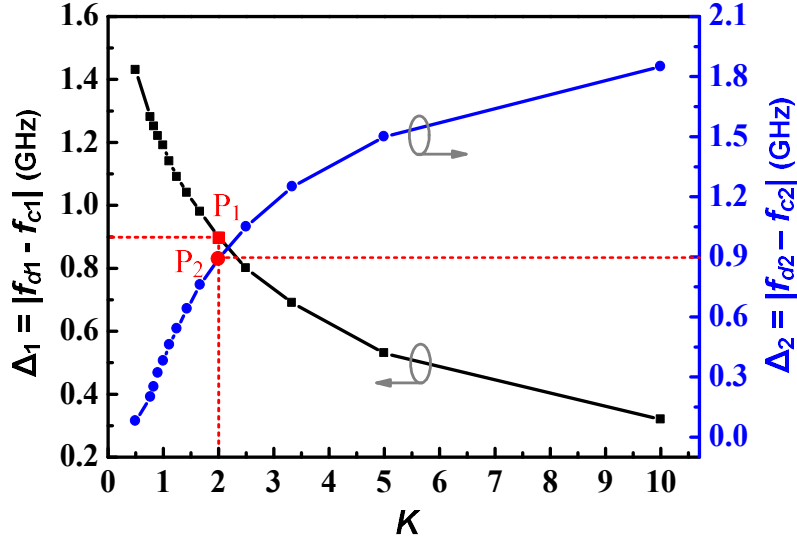
Fig. 3.5    Variation of Δ1 and Δ2 with different admittance ratio $K$.

frequencies can be varied by changing the electrical lengths $\theta_i$ ($i$ = 1, 2, and 3) and the admittance ratio $K$. The typical frequency responses of the SI-SRLR with different values of the admittance ratio $K$ are drawn in Fig. 3.4, which are obtained by using the Agilent ADS simulator. In the simulation, $\theta_1$ and $\theta_3$ are chosen as 60° and 17°, respectively, at 2.2 GHz, and $Y_1$ is 0.01 S. It is seen from Fig. 3.4, four resonant modes of SI-SRLR are observed, including two DM modes at $f_{d1}$ and $f_{d2}$, and two CM modes at $f_{c1}$ and $f_{c2}$. As $K$ increases, the frequencies of the two DM increase, while the two frequencies of CM reduce. We define $\Delta_1 = |f_{d1} - f_{c1}|$ and $\Delta_2 = |f_{d2} - f_{c2}|$, indicating the frequency separation between the two pairs of DM and CM modes. In Fig. 3.5, we show the variation of $\Delta_1$ and $\Delta_2$ against the admittance ration $K$. As can be seen, with the increase of $K$, $\Delta_1$ decreases while $\Delta_2$ increases. This means that the frequency separation between the two pairs of DM and CM modes can be adjusted by changing $K$.

In the design of differential BPF by using multimode resonator, DMs and CMs are always excited simultaneously. If the CM resonant frequency approaches close to the DM frequency, the CM will interfere with the DM, thereby degrading the performance of the differential system [36], [40]. Thus, a large frequency separation between two adjacent DM and CM is highly desired for good DM response and deep in-band CM suppression. As shown in Fig. 3.5, when a small $K$ is chosen, we can get a big $\Delta_1$ but $\Delta_2$ is very small, and vice versa. When $K$ = 2, a balanced frequency separation of the two pairs of DM and CM frequencies can be obtained. The corresponding $\Delta_1$ and $\Delta_2$ is 0.9 (|2.6 - 3.5|) GHz and 0.89 (|4.9 - 5.79|) GHz,
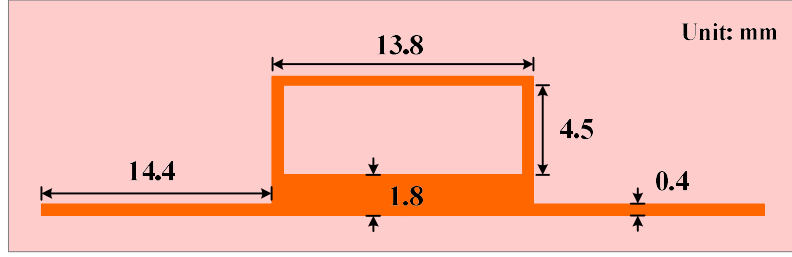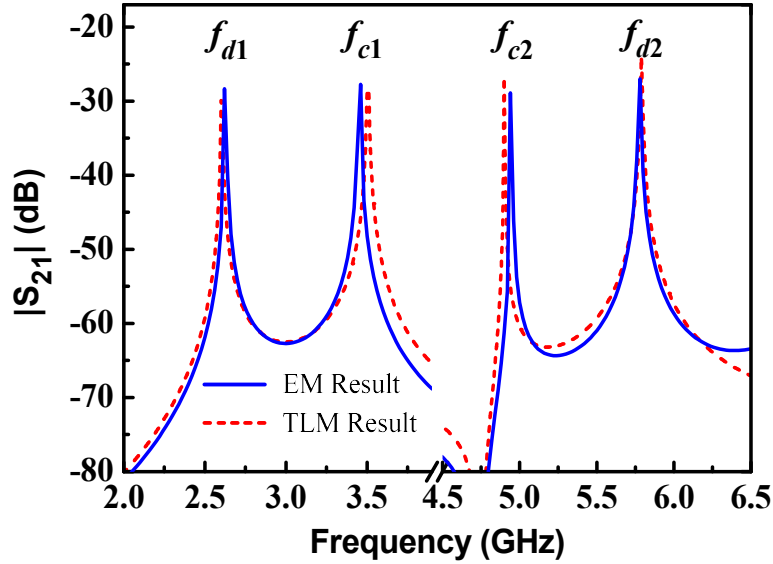
Fig. 3.6 (a) Configuration of the designed quadruple-mode SI-SRLR.
(b) EM and TLM simulated results of the SI-SRLR under weak excitations.

respectively, as shown in Fig. 3.5. The simulated result of the SI-SRLR TLM by ADS simulator under weak excitation is portrayed the red dashed-line in Fig. 3.6(b).

## 3.2.2 Dual-Band Differential Filter Design

In this part, the SI-SRLR is employed to design a dual-band differential BPF with two passbands centered at 2.6 GHz and 5.8 GHz, respectively. Based on the analysis in above section, the dimensions of the quadruple-mode resonators are determined first. Next, the coupling between the feed line and the SI-SRLR and the coupling between two SI-SRLRs are investigated. At last, the source-load coupling method for producing TZs and the CM frequency dispersion technique for noise reduction are applied to improve the performance of both DM response and CM suppression.

### 3.2.2.1 Design of the SI-SRLR

As concluded from Fig. 3.5, the admittance ration $K$ of the SI-SRLR is chosen as 2 for
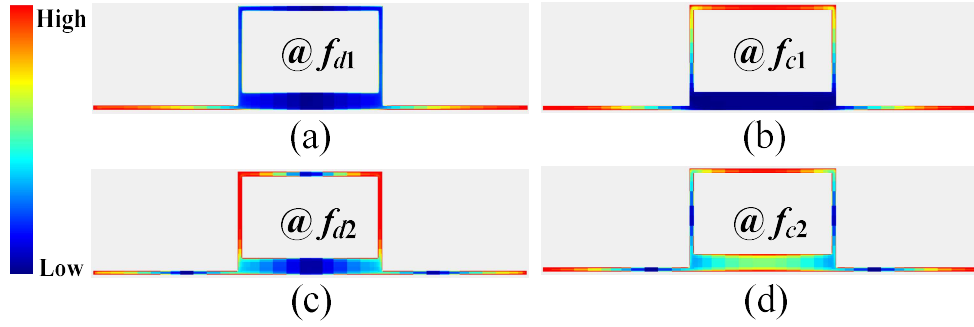
Fig. 3.7 Simulated voltage distributions of SI-SRLR at four resonant modes. (a) $f_{d1}$. (b) $f_{c1}$. (c) $f_{d2}$. (d) $f_{c2}$.

obtaining the balanced frequency separation between the two pairs of DM and CM frequencies and its separation between the two pairs of DM and CM frequencies. The other electrical parameters are kept the same as those used for Fig. 3, i.e., $\theta_1 = 60°$ and $\theta_3 = 17°$ at 2.2 GHz, and $Y_1 = 0.01$ S. $Y_2$ is then 0.02 S as $K = 2$ and $Y_1 = 0.01$ S. The substrate Taconic RF35 with a relative dielectric constant of 3.5 and a thickness of 0.8 mm is used in this paper. From the above electrical parameters, and by using the commercial electromagnetic software *Sonnet em*, the geometrical dimension of the SI-SRLR are obtained and are shown in Fig. 3.6(a). Its EM simulated frequency response under weak excitation is depicted as the blue solid line in Fig. 3.6(b). It can be obtained from figure that the simulated frequency separations $\Delta_1$ and $\Delta_2$ are 0.85 (|2.61 - 3.46|) GHz and 0.85 (|4.94 - 5.79|) GHz, respectively. The discrepancies of resonant frequencies and its separations between the EM simulation and the TLM calculation are attributed to the parasitic effects in EM modeling, which are ignored in the TLM. Fig. 3.7 exhibits the simulated voltage distribution over the SI-SRLR at four resonant modes. It is observed that the voltage is mainly concentrated on two open-circuited stubs at $f_{d1}$ whereas the voltage distributes on not only the one part of the open-circuited stubs but also the vertical segments of square ring at $f_{d2}$. For CM resonances, the voltage distributions cover the open-circuited stubs as well as the horizontal segments of square ring. The discrepancy of voltage distributions between the DM and CM resonances is advantage for CM suppression by using the auxiliary method.

### 3.2.2.2 Design of the Dual-Band Differential BPF

In this part, a second-order dual-band differential BPF is designed based on the previous design of the quadruple-mode SI-SRLR. Fig. 3.8(a) presents the geometrical structure of the designed dual-band differential BPF with two coupled SI-SRLRs. For size reduction, the open-stubs of the SI-SRLR are folded. The two passbands having Chebyshev response with
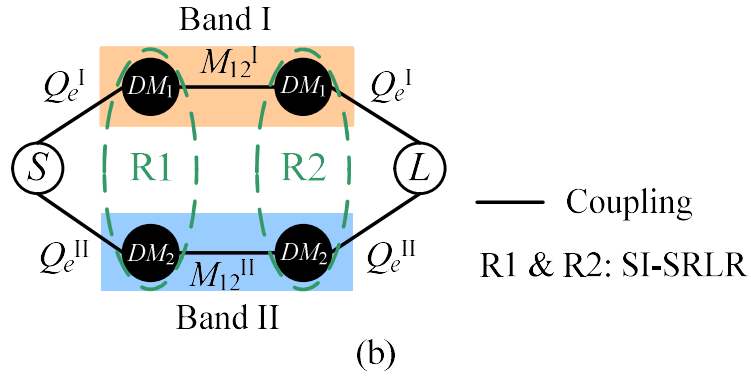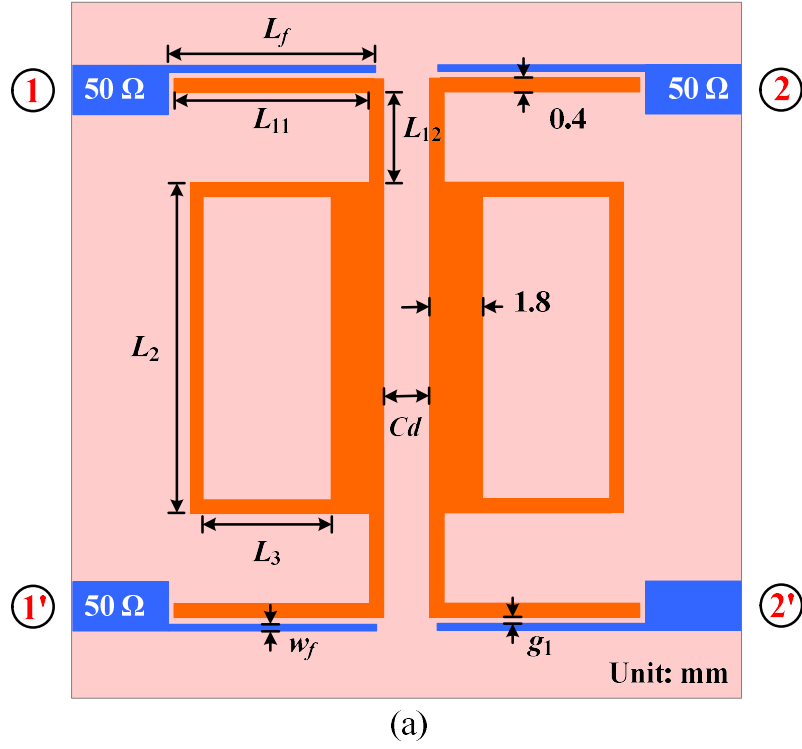
Fig. 3.8    (a) Configuration of the dual-band differential BPF.
(b) Coupling scheme of the BPF under DM operation.

0.04321-dB ripple level are specified at 2.6 GHz and 5.8 GHz. The corresponding desired fractional bandwidth (FBW) is 4.12% and 1.5%, respectively. The coupling scheme of the BPF under DM operation is depicted in Fig. 3.8(b), where nodes $S$ and $L$ denote input and output ports, respectively. Nodes $DM_1$ and $DM_2$ represent the two DMs of SI-SRLR at $fd_1$ and $fd_2$. There are two coupling paths, each coupling path forms a DM passband. The lumped circuit elements of the low-pass prototype filter are found to be $g_0 = 1$, $g_1 = 0.6648$, $g_2 = 0.5445$, and $g_3 = 1.2210$ [24]. Based on (5) and (6), the required coupling parameters shown in Fig. 7(b) are: the coupling coefficients $M_{12}^{I} = 0.0684$ and $M_{12}^{II} = 0.0249$, the external quality factors $Q_e^{I} = 16.2$ and $Q_e^{II} = 44.3$.
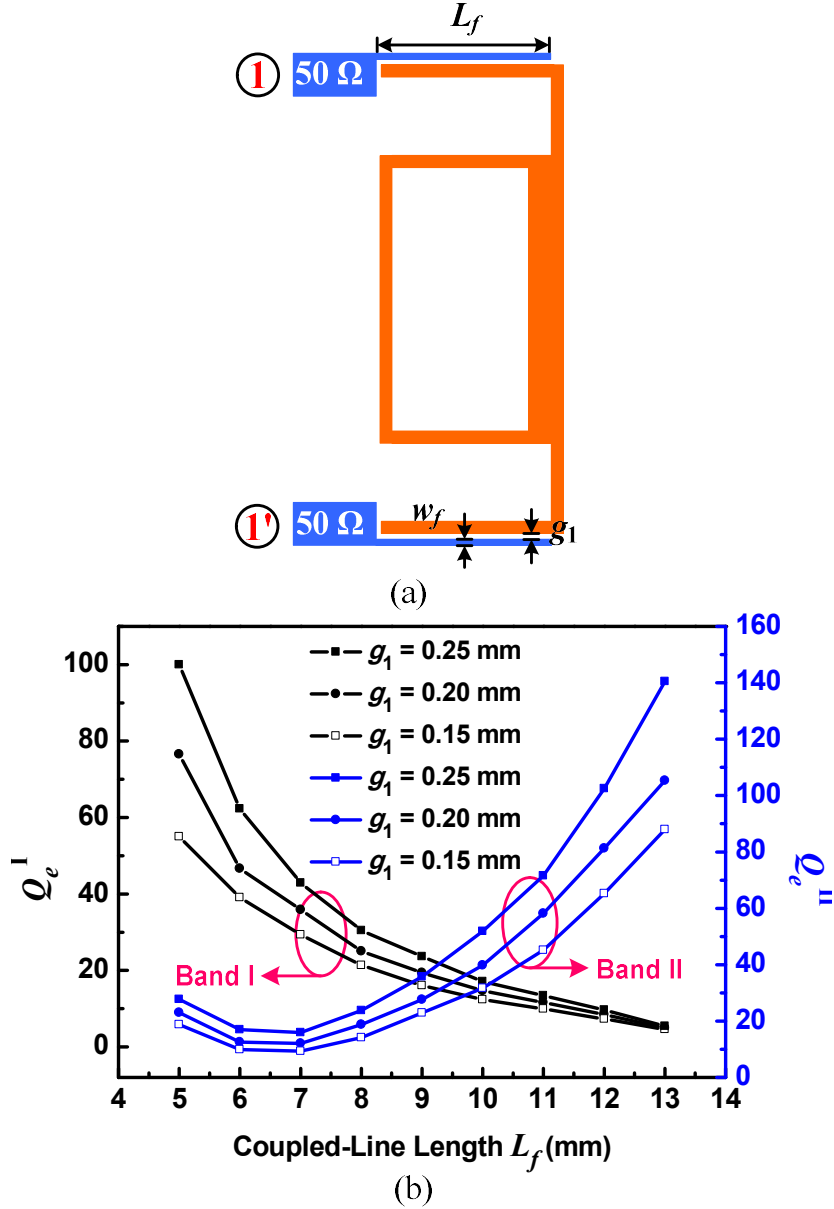
Fig. 3.9　(a) Parallel-coupled feed line structure of SI-SRLR. (b) The extracted $Q_e$ for two passbands under DM excitation, where $w_f$= 0.2 mm.

$$M_{i,i+1} = \frac{FBW}{\sqrt{g_i g_{i+1}}} \quad \text{for } i = 1 \text{ to } n-1 \tag{3.5}$$

$$Q_e = \frac{g_0 g_1}{FBW} \tag{3.6}$$

From the above external $Q$ values and coupling coefficients, we determine the dimensions of both the feed line structure and the internal coupling space between two SI-SRLRs, using the simulator Sonnet em. As shown in Fig. 3.9(a), microstrip parallel-coupled lines are chosen
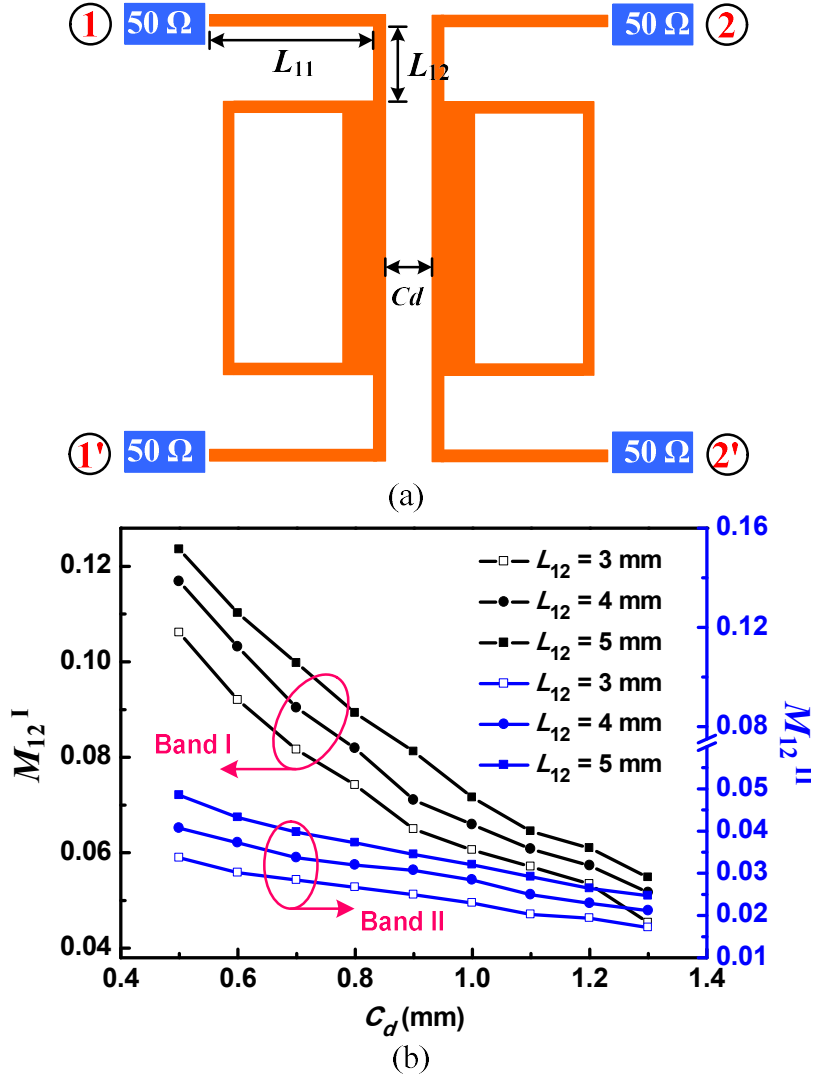
Fig. 3.10   (a) Configuration of two coupled SI-SRLRs. (b) Coupling coefficients as a function of the coupling space $C_d$ under DM excitation.

as the feeding structure in this design. The line width and coupling gap are denoted as $w_f$ and $g_1$, respectively. Fig. 3.9(b) plots the computed variation of the external $Q$ values, $Q_e^{\mathrm{I}}$ for the first passband and $Q_e^{\mathrm{II}}$ for the second passband, versus the coupled-line length $L_f$ when $w_f = 0.2$ mm. Note that a strong I/O coupling leads to a small external quality factor of a resonator [66]. So, it is seen that $Q_e^{\mathrm{I}}$ decreases monotonously as $L_f$ increases. While for $Q_e^{\mathrm{II}}$, it decreases at first as $L_f$ increases when $L_f$ is smaller than 7 but then increases monotonously when $L_f$ is larger than 7. The difference of the variations for two $Q_e$ is attributed to the different voltage distributions of two DM resonances on the open-circuited stubs, as indicated in Fig. 3.7. Also, it can be observed that as the coupling gap $g_1$ increases, the external $Q$ values of both passbands becomes larger. Because a larger coupling gap results in a weaker I/O coupling. From Fig. 3.9(b), the $L_f$ and $g_1$ are determined as 9.3 mm and 0.2 mm, respectively, for the
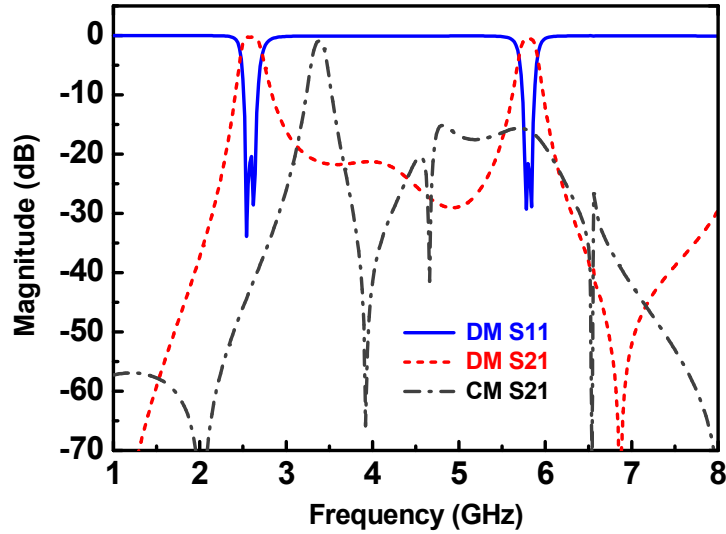
Fig. 3.11    Simulated DM &CM responses of the dual-band differential BPF.

designed filter.

Fig. 3.10(a) shows the configuration of two coupled SI-SRLRs, in which $C_d$ and $L_{12}$ are the coupling distance and length to adjust the total coupling strength. It should be noted that the sum of $L_{11}$ and $L_{12}$ should be remained a constant in order to keep the resonant frequency unchanged. Fig. 3.10(b) provides the computed variation of coupling coefficients, $M_{12}^{I}$ for passband I and $M_{12}^{II}$ for passband II, versus the coupling space $C_d$. It can be seen that the coupling coefficients of both passbands decrease monotonously as $C_d$ increases or $L_{12}$ decreases. From Fig. 3.10(b), the $C_d$ and $L_{12}$ are determined as 0.9 mm and 4 mm, respectively, for the designed filter. The remained geometrical dimensions in Fig. 3.8(a) are obtained after optimizing the frequency response of the filter using Sonnet, and these are: $L_{11}$ = 8.7 mm, $L_2$ = 13.8 mm and $L_3$ = 6.1 mm. With these geometrical parameters, the frequency response of designed dual-band differential BPF is simulated and depicted in Fig. 3.11. The simulated two DM passbands are centered at 2.6 and 5.8 GHz, and their corresponding FBW is 4.13% and 1.51%, respectively, which agree well with the desired specifications. Two reflection zeros are observed in both passbands and the return losses are better than 20 dB. The insertion losses of two passbands are 0.2 dB and 0.5 dB, which are mainly attributed to the dielectric loss (loss tangent is 0.0018).

In view of the CM response, it is seen that the minimum CM suppression is 40 dB within the first DM passband and 15 dB within the second DM passband. Besides, there is a CM resonance peak between the two passbands. Therefore, the CM suppression should be increased. In addition, improvement of the selectivity of the two DM passbands is also
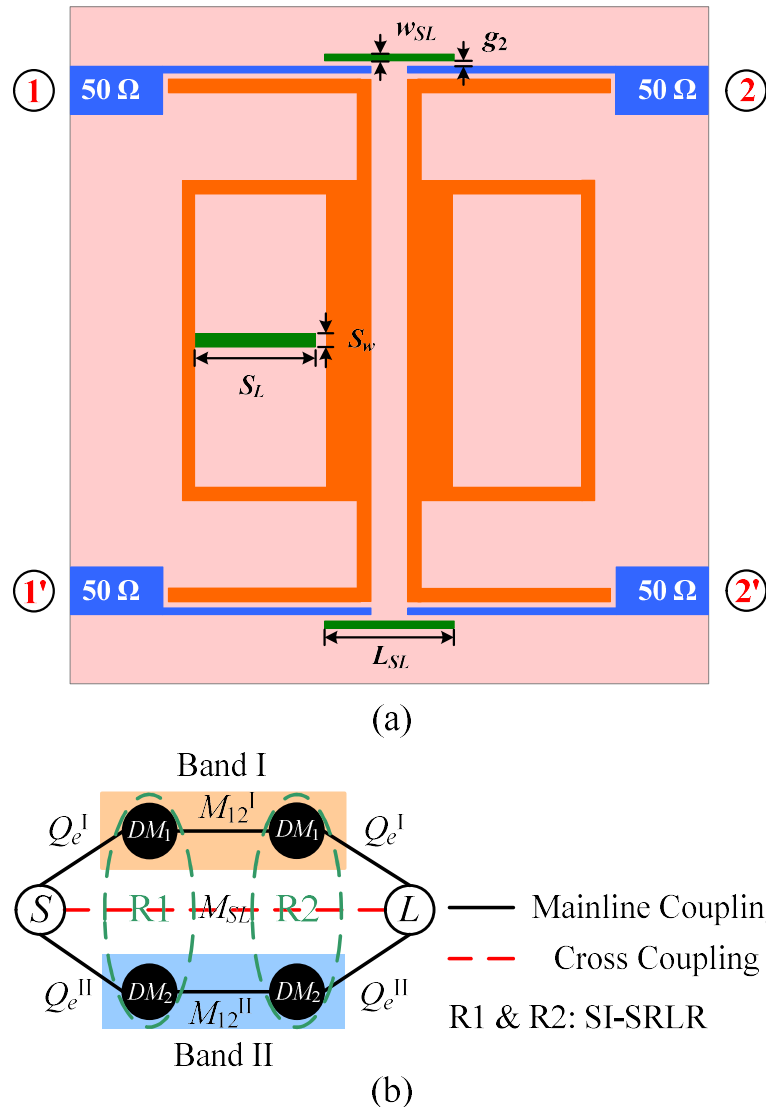
Fig. 3.12 (a) Configuration of the improved dual-band differential BPF.
(b) Coupling scheme of the improved BPF under DM condition.

wanted.

### 3.2.3 Performance Improvement

As shown in Fig. 3.8(a), the differential BPF has two identical SI-SRLRs, which have thereby identical DM and CM resonances. As a result, when DM resonances are well coupled to form the desired differential passbands, the CM noise will also be transmitted from the input to output by the built CM coupling path, thus incurring poor CM rejection.

As studied in [26], [29], the frequency discrepancy technique by separating the CM resonances in adjacent resonators is an effective method to block the transmission of CM signals. As illustrated in Fig. 3.7, it is obtained that the voltage on the center segment of resonator at two DMs are both near to null, while the voltage at CMs are strong, especially on
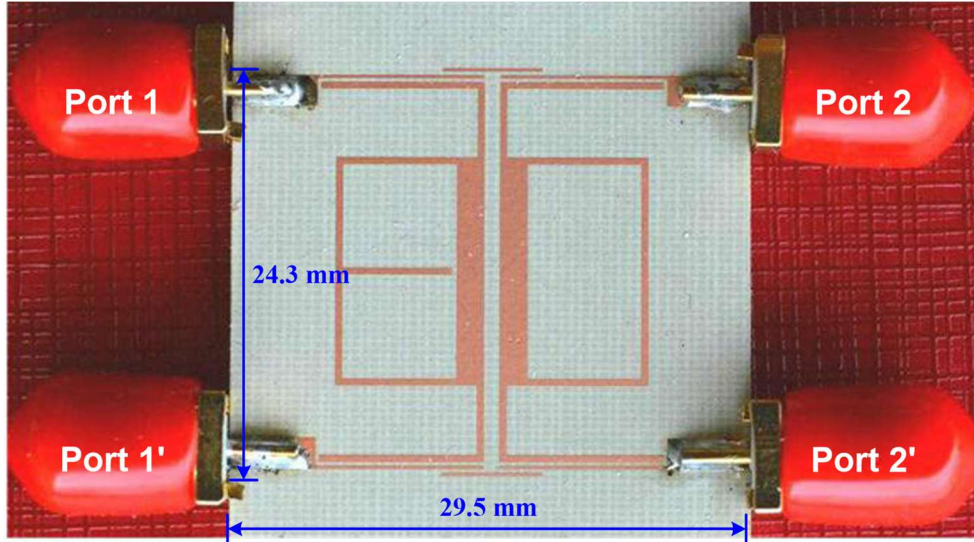
Fig. 3.13　Photograph of the fabricated dual-band differential BPF.

the high-impedance line segment. Therefore, the CM resonances will be shifted by inserting loaded elements at the symmetric plane while the DM resonances will be affected little. As shown in Fig. 3.12(a), an open stub with a length $S_L$ and a width $S_w$ is loaded at the center of the left SI-SRLR to shift its CM resonances. Then, the CM coupling between the left and right SI-SRLRs will be weaken, and the CM transmission will be reduced.

To enhance further the CM suppression within the DM passbands and improve the selectively of DM passbands, two short microstrip lines with a length $L_{SL}$ and a width $w_{SL}$ are added closely to the input and output feed lines, as shown in Fig. 3.12(a). Fig. 3.12(b) depicts the coupling scheme of the improved filter under DM excitation. Compared with the coupling scheme in Fig. 3.8(b), the coupling $M_{SL}$ between the source and load is introduced, which provides an additional transmission path. Based on the theory of transversal signal interference, multiple TZs will be produced and improve thereby the frequency selectivity of the BPF [76].

In addition, the introduced source-load coupling has also influence on the CM response as it changes the locations of TZs or produces new TZs under CM condition. With appropriate choice of the coupling strength, the CM TZs can be tuned to or produced at frequencies within the DM passbands, which will enhance significantly the CM rejection in the DM passbands. The parameterization and optimization tools of *Sonnet* are utilized to speed up the design process. After fine tuning, the dimensions for the loaded stub and the source-load coupling lines are finally determined as follows: $S_L$ = 5.9, $S_w$ = 0.4, $L_{SL}$ = 5.1, $w_{SL}$ = 0.2, and $g_2$ = 0.25 (unit: mm).
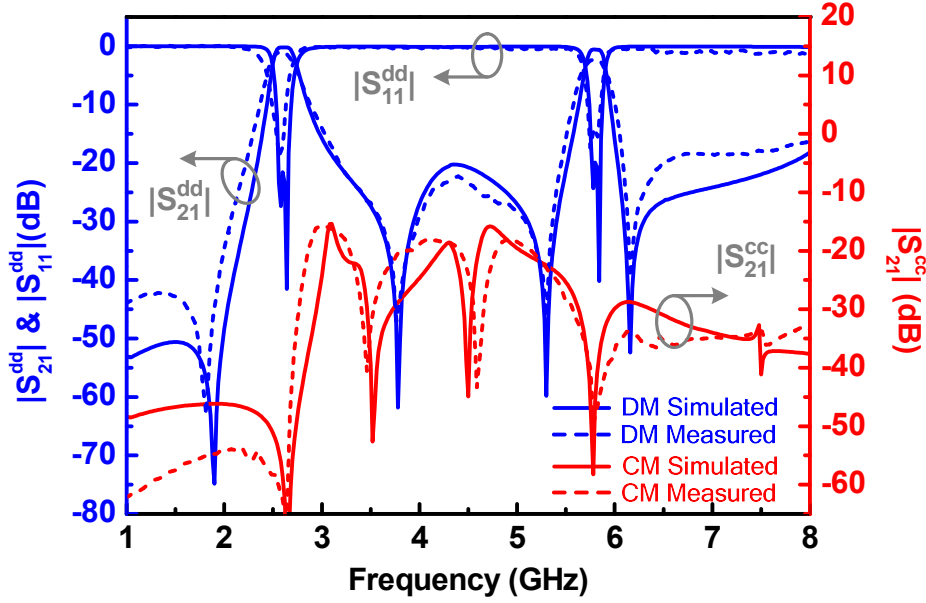
Fig. 3.14   Simulated and measured frequency responses of the BPF.

## 3.2.4 Experimental Results and Discussion

To verify the above design and the performance of the filter, the circuit shown in Fig. 3.12(a) is fabricated, and its photograph is shown in Fig. 3.13. The overall size (excluding the feed lines) is 18.2 mm × 24.0 mm, about 0.26 $\lambda_g$ × 0.34 $\lambda_g$, where $\lambda_g$ is the guide wavelength at 2.6 GHz. The filter measurement is executed on a four-port vector network analyzer, Agilent E5071C.

In Fig. 3.14 the simulated DM response is drawn by blue solid lines. Apparently, four DM TZs, located at 1.9 GHz, 3.78 GHz, 5.3 GHz, and 6.15 GHz, are located in the vicinities of the passbands, which highly improve the selectivity of two DM passbands. The simulated CM response is depicted in red solid line. It is observed that the minimum CM suppression within the DM passband are 60 dB for the first passband and 45 dB for the second passband. The dashed lines in Fig. 3.14 represent the measured responses of the filter, which agree reasonably with the simulated data. For the DM responses, the measured first and second passbands are centered at 2.58 and 5.79 GHz, respectively, with corresponding 3-dB frequency ranges of 2.44 - 2.71 GHz and 5.68 - 5.89 GHz. The measured minimum insertion losses are 1.1 dB and 2.1 dB for the first and the second passband, respectively. Four TZs, located at 1.8 GHz, 3.77 GHz, 5.3 GHz, and 6.17 GHz, are observed and improve significantly the passband selectivity. For CM response, the measured minimum CM insertion losses within the DM passbands are 62 dB for the first passband and 48 dB for the second passband, which show a good CM suppression level within DM passbands. Besides, CM suppression over 1 to 8 GHz is better than 15 dB. Deviations between the simulated and measured results are mainly due to the fabrication

Table 3.1

Comparison of Some Previous Dual-Band Differential/Balanced Filters

| Ref. | Center Frequency (GHz) | 3-dB FBW (%) | Line type of Resonators | Insertion Loss (dB) | CM Attenuation in Two DM Passbands (dB) | Number of TZs | Circuit Size ($\lambda_g \times \lambda_g$) |
|---|---|---|---|---|---|---|---|
| [25] | 2.45 / 5.25 | 9.8 / 4.6 | Microstrip | 2.4 / 2.82 | 53 / 45 | 0 | 0.38 × 0.42 |
| [26] | 2.46 / 5.56 | 16.3 / 6.7 | Microstrip & Lumped Elements | 1.9 / 1.9 | 36 / 31 | 4 | 0.31 × 0.41 |
| [27] | 2.5 / 5.6 | N/A | Microstrip & DGS | 1.29 / 1.97 | 34.7 / 24.1 | 1 | 0.15 × 0.27 |
| [40] | 2.5 / 5.8 | 12.9 / 4.5 | Microstrip | 0.77 / 1.56 | 42 / 38 | 0 | 0.15 × 0.37 |
| [29] | 1.8 / 5.8 | 4.5 / 1.8 | Microstrip | 1. 2 / 2.0 | 35 / 25 | 4 | 0.37 × 0.28 |
| [32] | 2.4 / 3.57 | 7.5 / 5.0 | Microstrip | 0.87 / 1.9 | 28 / 31 | 1 | 0.50 × 0.20 |
| [28] | 2.4 /5 | 16.4 / 8.6 | Microstrip | 1.78 / 2.53 | 32 / 32 | 1 | 0.50 × 0.70 |
| [33] | 2.44 / 5.19 | 18 / 8.7 | Microstrip & Slotline | 1.14 / 2.05 | 42 / 42 | 3 | N/A |
| [34] | 2.64 / 5.17 | 24.6 / 13.9 | Microstrip & Slotline | 0.88 / 1.51 | 65 / 52 | 2 | N/A |
| [19] | 2.45 / 5.85 | 6.5 / 3.0 | Microstrip & Lumped Elements | 1.06 / 2.04 | 25 / 25 | 1 | N/A |
| [35] | 0.9 / 2.49 | 3.6 / 2.1 | Microstrip | 2.67 / 4.65 | 30 / 40 | 3 | 0.53 × 1.10 |
| [37] | 9.47 / 9.96 | 2.9 / 3.1 | SIW | 1.89 / 1.73 | 30 / 30 | 1 | 2.87 × 2.95 |
| [38] | 9.23 / 14.05 | 2.8 / 5.6 | SIW & Slotline | 2.9 / 2.7 | 48 / 40 | N/A | 2.70 × 1.27 |
| [39] | 3.58 / 5.6 | 5.8 / 3.4 | Microstrip | 1.1 / 1.8 | 25 / 17 | 4 | 0.25 × 0.47 |
| This work | **2.6 / 5.8** | **10.4 / 3.6** | **Microstrip** | **1.1 / 2.15** | **62 / 48** | **4** | **0.26 × 0.34** |

tolerance and the parasitic effects from the solder connections. Moreover, the comparison of proposed dual-band filter with other differential dual-band filters is summarized in Table 3.1. It is seen that the proposed differential filter outperforms the works in [27] and [40] in terms of the

CM rejection and the selectivity of DM passbands. Also, the circuit size is found to be competitive when compared with the other designs.

## 3.3 Tri-Band Differential Bandpass Filter Based on Sext-Mode SI-SRLR

In this part, a compact tri-band differential BPF is developed by using the proposed sext-mode stepped-impedance square ring loaded resonators (SI-SRLR). The new SI-SRLR has six resonant modes, including three DMs and three CMs. Three DMs of the proposed resonator are used to build the triple DM passbands. Same as before, the appropriately admittance ratio $K$ of SI-SRLR is chosen to inhibit the CM signal in within three DM passbands for achieving a good CM suppression.

### 3.3.1 Analysis of Sext-Mode SI-SRLR

Fig. 3.15(a) depicts the transmission line model (TLM) of the proposed sext-mode SI-SRLR. The TLM consists of eight transmission line sections, with corresponding electrical lengths and characteristic admittances as $\theta_1$, $2\theta_2$, $\theta_3$, $\theta_4$, and $Y_1$, $Y_2$, $Y_3$, $Y_4$, respectively. Compared with the presented quadruple-mode SI-SRLR in [77], the proposed new SI-SRLR has two additional open-circuited stubs that loaded at upper two corners of square ring. Thus, two more resonances, total six resonant modes, are obtained. As conducted in [77], the even- and odd- mode method is used to analysis the symmetrical SI-SRLR. Under the even-/odd-mode excitation (with respective to CM case and DM case), the symmetrical plane (red dashed line) of the circuit behaves as a perfect magnetic wall or electric wall, respectively, and the DM and CM bisection of the SI-SRLR are shown in Fig. 3.15(b) and Fig. 3.15(c), respectively. Herein, $Y_1 = Y_2 = Y_4$ is assumed for simplification, and define $K = Y_1/Y_3$. Following the transmission line theory, the resonant condition can be written as

$$\text{Im}\left(Y_L + Y_R^{DM}\right) = 0 \text{ , DM case} \tag{3.7}$$

$$\text{Im}\left(Y_L + Y_R^{CM}\right) = 0 \text{ , CM case} \tag{3.8}$$

where $Y_L$, $Y_R^{DM}$, and $Y_R^{CM}$ are the input admittances of the corresponding TL counterparts, as denoted in Fig. 3.15(b) and 3.15(c) and given by
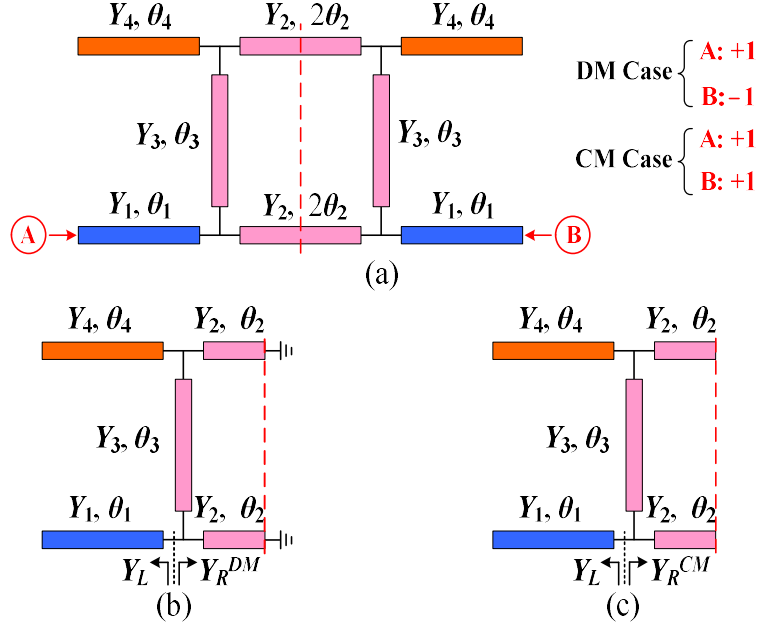
Fig. 3.15. (a) Transmission line model of the proposed SI-SRLR; (b) DM bisection; (c) CM bisection.

$$Y_L = jY_1 \tan\theta_1, \tag{3.9}$$

$$Y_R^{DM} = jY_1 \left[ \frac{\tan\theta_3 + K\tan\theta_4 - K\cot\theta_2}{K + K^2 \cot\theta_2 \tan\theta_3 - K^2 \tan\theta_3 \tan\theta_4} - \cot\theta_2 \right], \tag{3.10}$$

$$Y_R^{CM} = jY_1 \left[ \frac{\tan\theta_3 + K\tan\theta_2 + K\tan\theta_4}{K + K^2 \tan\theta_2 \tan\theta_3 + K^2 \tan\theta_3 \tan\theta_4} + \tan\theta_2 \right]. \tag{3.11}$$

Thus, the DM resonant frequencies and CM resonant frequencies can be found by solving (3.7) and (3.8). It is obvious that all of resonances can be varied by changing the electrical lengths and the admittance ratio $K$. As studied in [78], both the DM bisection and CM bisection of SI-SRLR behave as a triple-mode stub-loaded resonator. Three DM resonances and three CM resonances are denoted as $f_{d1}$, $f_{d2}$, $f_{d3}$, and $f_{c1}$, $f_{c2}$, $f_{c3}$, respectively. The typical frequency responses of the SI-SRLR obtained by using the ADS simulator and *sonnet* em simulator are drawn in Fig. 3.16. In the simulation, $\theta_1$, $\theta_2$, $\theta_3$, and $\theta_4$ are chosen as 48°, 53°, 37°, and 34°, respectively, at 1.9 GHz. $Y_1 = 0.01$ S and $K = 0.42$ are used. Based on the given electrical parameters, the microstrip line model of SI-SRLR with the optimized geometrical dimensions is obtained and shown the inserted configuration in Fig. 3.16. The used substrate is Roger RO4003C with $\varepsilon_r$ of 3.38 and thickness of 0.813 mm. As expected, six resonances are clearly observed in Fig. 3.16 and the EM simulation matches well with the TLM result. In addition, it
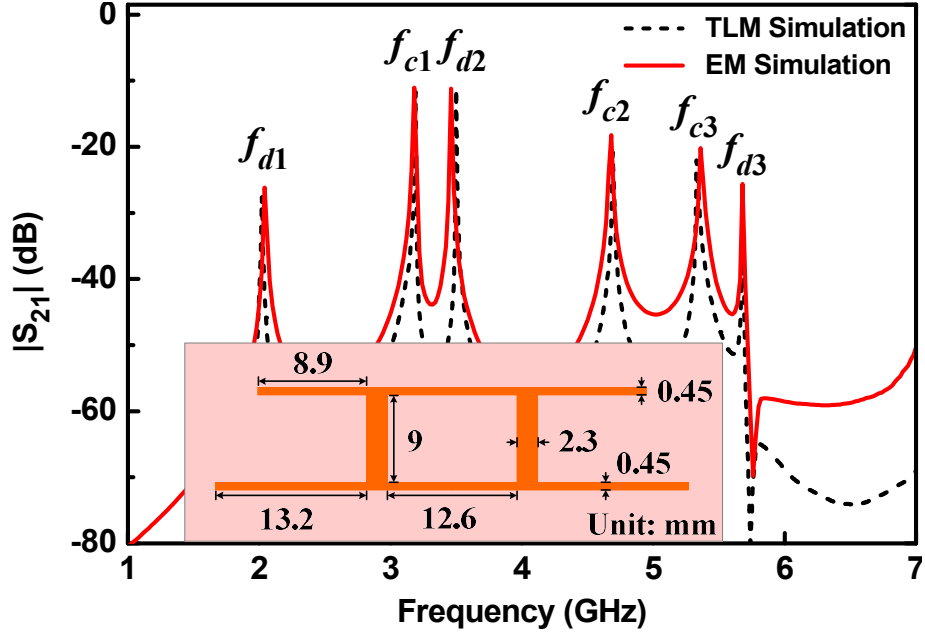
Fig. 3.16.    TLM and EM simulated results of the SI-SRLR under weak excitation.
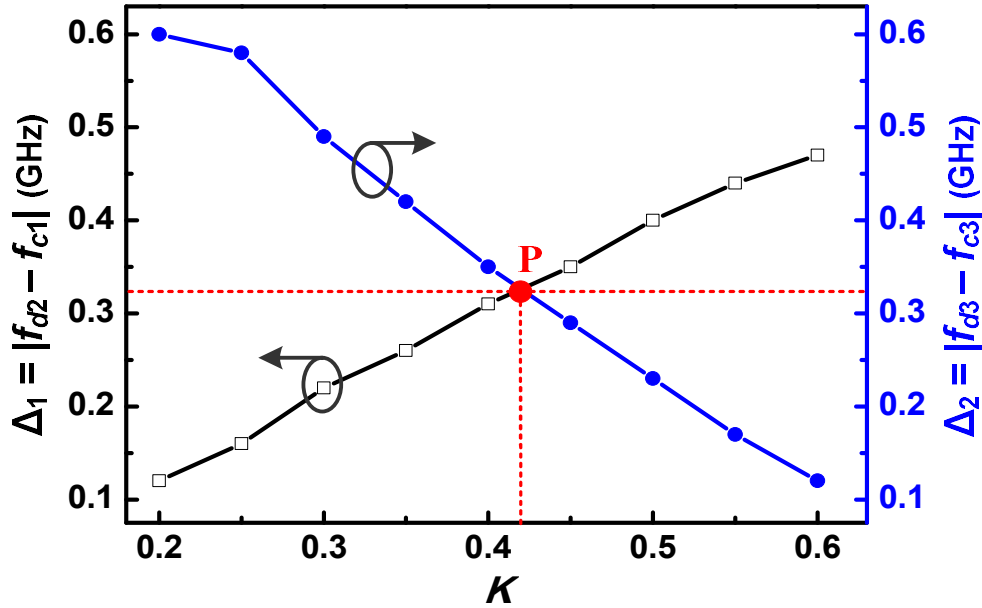


Fig. 3.17.    Variation of $\Delta_1$ and $\Delta_2$ with different admittance ratio $K$.

is found from the simulation that the frequency separations of between $f_{c1}$ and $f_{d2}$ and between $f_{c3}$ and $f_{d3}$ can be adjusted by changing $K$. We define $\Delta_1 = |f_{d2} - f_{c1}|$ and $\Delta_2 = |f_{d3} - f_{c3}|$, indicating the frequency separation between two pairs of the tightly adjacent DM and CM resonances. Fig. 3.17 shows the variation of $\Delta_1$ and $\Delta_2$ against the $K$. It is seen that $\Delta_1$ decreases while $\Delta_2$ increases with enlarged $K$. When $K = 4.2$, a balanced frequency separation of two pairs resonances is obtained, as indicated the red point P in Fig. 3.17. It is a key point to

achieve the desirable CM suppression both in the second and third DM passbands
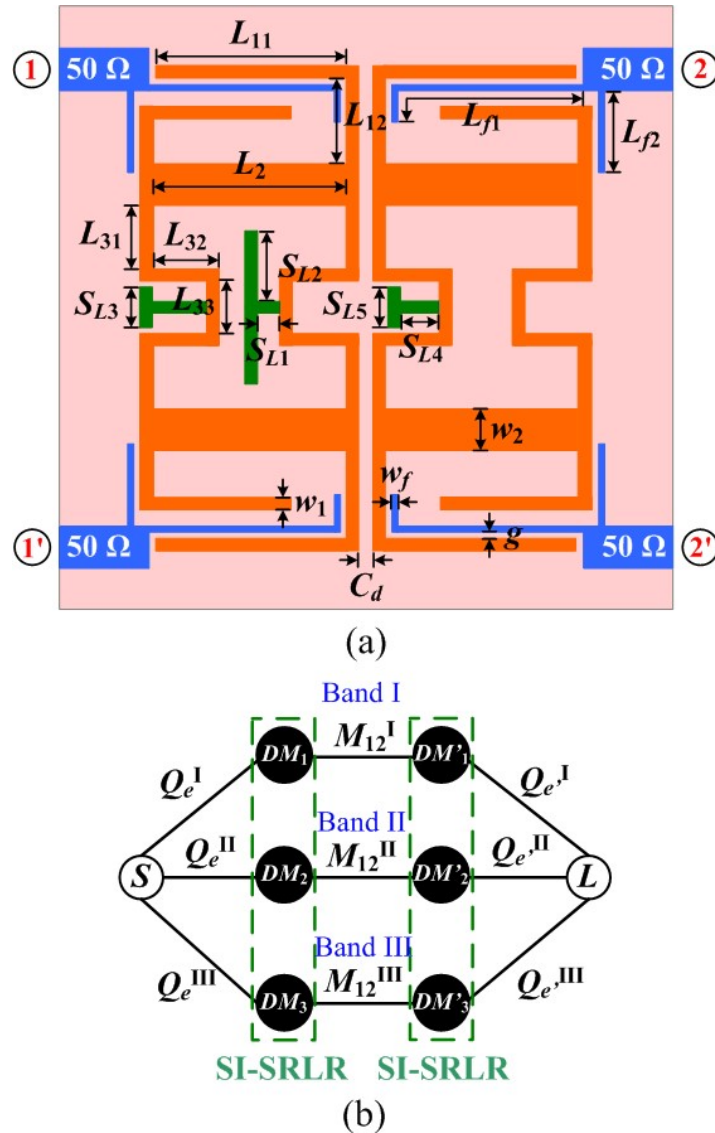


Fig. 3.18. (a) Configuration of the proposed balanced tri-band BPF.
(b) Coupling scheme of the BPF under DM operation.

simultaneously.

### 3.3.2 Tri-Band Differential Filter Design

Based on sext-mode SI-SRLR, a compact balanced tri-band BPF with three DM passbands centered at 1.9 GHz, 3.35 GHz, and 5.8 GHz, respectively, is designed. The configuration of the filter is given in Fig. 3.18(a). Four open-circuited stubs as well as the center lines of SI-SRLR are folded inner or meandered for compact size. Fig. 3.18(b) presents the coupling scheme of the BPF under DM excitation. There are three coupling paths, each path forms one DM passband. To obtained the required coupling coefficients of three passbands, the

geometrical parameters $L_{12}$, $L_{33}$, and $C_d$ are determined by simulated extraction. On the other
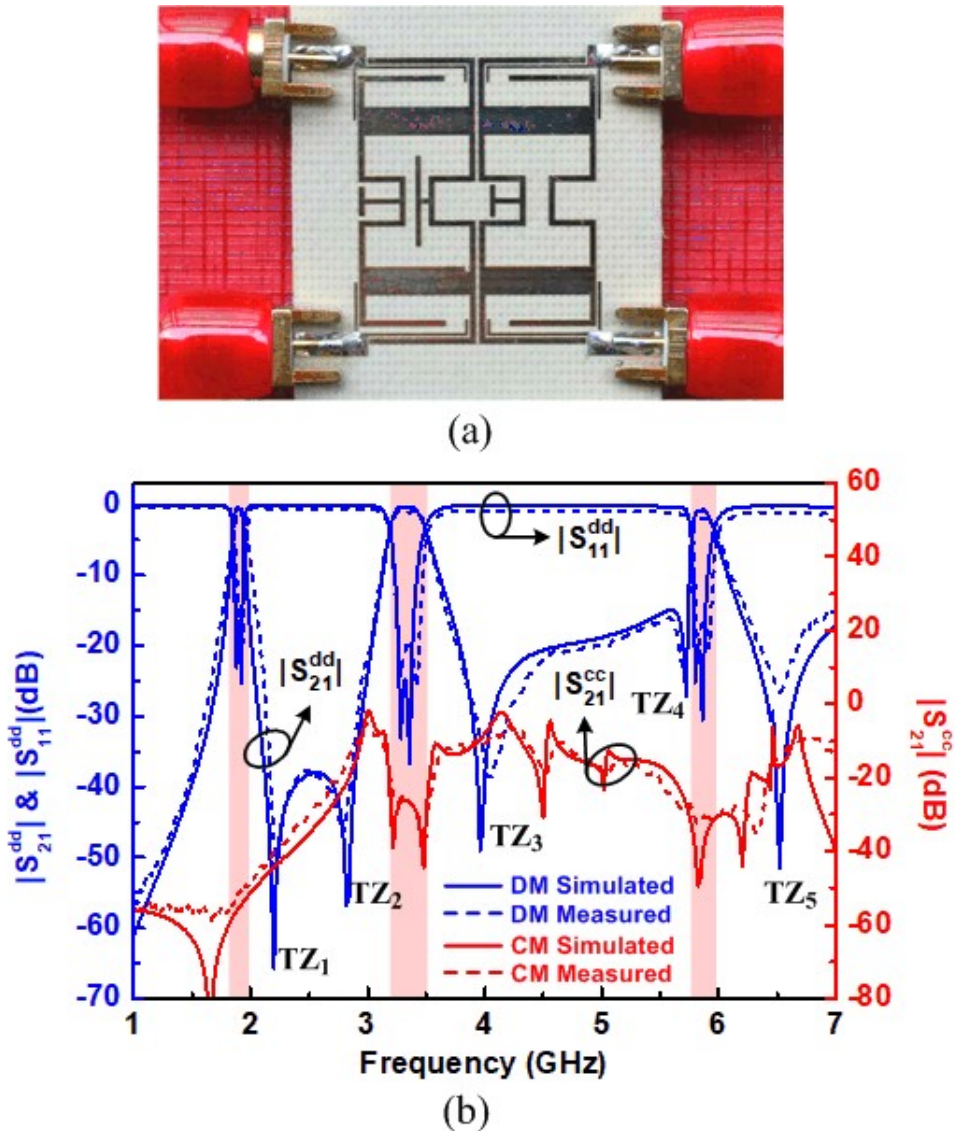


Fig. 3.19.   (a) Photograph of the designed balanced tri-band BPF. (b) Simulated and measured results and photograph of the fabricated balanced tri-band BPF.

hand, two high-impedance microstrip lines, act as the feeding line structures, with dimension $L_{f1}$, $L_{f2}$, $w_f$, and $g$ are tuned to meet the demanded external quality factors.

### 3.3.3 Performance Improvement

Moreover, three T-shaped stubs are loaded at the center of both two coupled SI-SRLRs to shift their CM resonances without affecting DM resonances, as shown in Fig. 3.18(a). Then, the CM coupling between two coupled SI-SRLRs will be weaken, and the CM transmission will be reduced. With the help of the parameterization and optimization tools of *Sonnet*, the dimensions of the designed filter are finally determined as follows: $L_{11} = 8.15$, $L_{12} = 3.55$, $L_2 = 9$, $L_{31} = 3.35$, $L_{32} = 3.3$, $L_{33} = 3.2$,   $L_{f1} = 9.3$, $L_{f2} = 4.2$, $S_{L1} = 0.65$, $S_{L2} = 3.5$, $S_{L3} = 2.4$, $S_{L4} = 2$, $S_{L5} = 2.6$, $w_1$

= 0.45, $w_2$ = 2.3, $w_f$ = 0.2, $g$ = 0.2, and $C_d$ = 0.3 (unit: mm).

Table 3.2  Compared with previous balanced tri-band BPFs

| Ref. | $f_0$ (GHz) | IL (dB) | $\left\|S_{21}^{cc}\right\|$ (dB) | TPs/TZs | Circuit Size ($\lambda_g \times \lambda_g$) |
|---|---|---|---|---|---|
| [40] | 2.5/3.5/5.8 | 0.8/2.3/2.4 | 32/31/32 | 4/2 | 0.18×0.38 |
| [41] | 1.23/2.39/3.5 | 1.09/2.15/1.33 | 25/21/28 | 6/3 | 0.20×0.42 |
| [42] | 1.57/2.48/3.5 | 0.45/0.38/1.4 | 45/41/40 | 3/3 | 0.14×0.22 |
| [43] | 2.4/3.51/5.2 | 2.43/3.5/3.6 | 46/38/33 | 6/3 | 0.25×0.25 |
| [44] | 1.57/2.4/3.89 | 1.37/0.42/0.32 | 50/48/50 | 5/4 | 0.21×0.28 |
| **This work** | **1.9/3.35/5.8** | **0.94/1.21/1.93** | **54/27/32** | **6/5** | **0.19×0.23** |

### 3.3.4 Experimental Results and Discussion

To verify the above design, the filter shown in Fig. 3.18(a) is fabricated, and its photograph is given in Fig. 3.19(a). The overall size is 19.1 mm × 23.4 mm (0.19 $\lambda g$ × 0.23 $\lambda g$), where $\lambda g$ is the guided wavelength at 1.9 GHz. The measurement is executed on a four-port vector network analyzer, Agilent E5071C.

The simulated results and measured results are illustrated in Fig. 3.19(b). The solid lines indicate the simulation and the dashed lines represent the measurement, and they are agree reasonably with each other. For DM response, the measured three passbands are centered at 1.92 GHz, 3.34 GHz, and 5.84 GHz, with a 3-dB fractional bandwidth of 4.74%, 8.61%, and 2.78%, respectively. The measured minimum in-band insertion losses are 0.94 dB, 1.21 dB, and 1.93 dB at the three passbands, respectively. Five transmission zeros (TZs, $TZ_1$-$TZ_5$) generated by SI-SRLR and signal cancellation between two coupling paths improves the selectively of DM passbands. For CM response, the measured minimum CM insertion losses within the three DM passbands are 54 dB, 27 dB, and 32 dB, respectively, which shows a good CM suppression within DM passbands. Besides, Table 3.2 gives a comparison of the proposed balanced tri-band BPF with other reference works. It is seen that the implemented balanced tri-band BPF has merits like the flatness of DM passbands, high selectivity, and compact circuit size.

## 3.4 Conclusion

In this chapter, a newly multimode SI-SRLR was proposed and used to construct a novel dual-band differential BPF and a tri-band differential BPF. DM and CM characteristics of the SI-SRLR are analyzed by the even- and odd-mode method. The admittance ratio $K$ of SI-SRLR is used to obtain balanced frequency separations of two/three pairs of DM and CM resonances, which is important to prevent the interference between DM and CM resonances. Furthermore, stub-loading and source-load coupling techniques are applied to improve the CM suppression in a wide frequency range and enhance the frequency selectivity of DM passbands. The designed dual-band/tri-band differential BPF has the advantages of small size, high performance DM passbands, and large CM suppression over a wide frequency range, which are attractive in the applications for differential multimode and multiband communication systems.

The work described in Section 3.2 have been published in the IEEE Access, and the design organized in Section 3.3 have been published in the IEICE Electronics Express.

# Chapter 4

# High-Order Dual-Band HTS Differential Bandpass Filters

## 4.1 Overview

From the literature review on multi-band differential bandpass filters (BPFs) in chapter 1 and two designed multi-band differential BPFs in chapter 3, it is known that though good DM transmission and CM noise rejection are achieved in these reports, these filters are suffering from the high insertion losses caused by the large surface resistance of normal copper board.

Instead of the normal conductors, high-temperature superconducting (HTS) materials can be used to realize low loss and better performance. Up to now, many types of dual-band HTS BPFs have been presented [79]-[82]. However, to our best knowledge, differential filters implemented with HTS technology have not been reported in public.

Multimode resonators are widely used to design dual-band differential BPFs in order to have compact circuit size, such as SIRs [25], [26], [27], and stub-loaded resonators [29], [36], [18]. However, these resonators are difficult to be used to design high-order dual-band BPFs with controllable midband frequencies and bandwidths. Although fourth-order differential BPFs are reported in [25], [26], [27], [37], and [38], only two or three poles are observed the passband, and optimal designs of these filters are not successfully achieved.

Therefore, in this chapter, two new multimode resonators, which can be use to construct high-order dual-band differential BPF conveniently, are proposed. Resonant characteristics of these two resonators are well analyzed by even-/odd-mode method and simulation technique in detail. The coupling properties, including the internal coupling of two adjacent resonators and the external coupling of between the first/last resonator and feed lines, are also discussed deeply. Some unique features of the proposed two resonators result in the controlling of midband frequencies and the bandwidths of two passbands independently. In addition, high-temperature superconducting (HTS) material, replaced the normal copper board, is adopted to reduce significantly the insertion loss. Finally, a fourth-order HTS dual-band
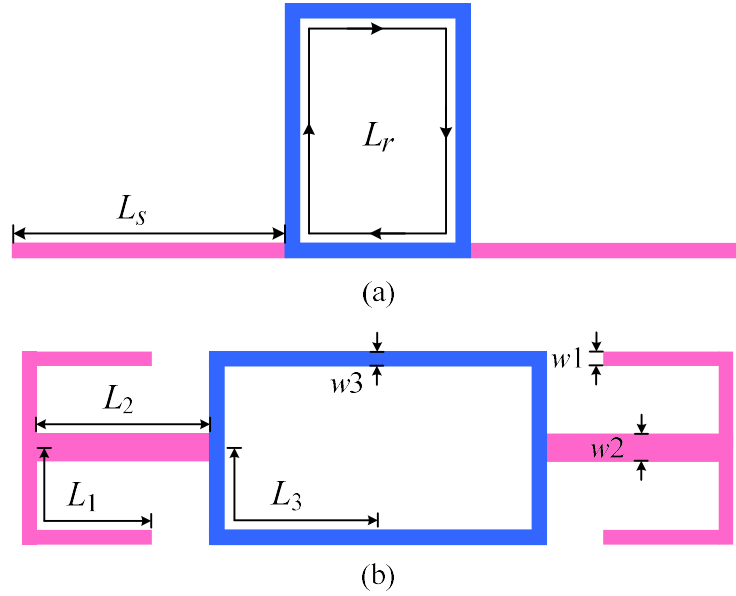
Fig. 4.1.    (a) Conventional SRLR. (b) The proposed modified multi-mode SRLR.

differential BPF and a eighth-order HTS dual-band differential BPF are designed, fabricated and measured to verify the proposed structure and design method.

## 4.2 Fourth-Order Dual-Band HTS Differential Bandpass Filter

In [83], a compact square ring loaded resonator (SRLR) is firstly presented and its multi-mode feature is then proven in [84]. Furthermore, a quadruple-mode SRLR unit cell is proposed and applied to design a compact and high-selectivity dual-band BPF [74], to design a quad-band HTS BPF with ultra-low insertion loss [76], and to design a second-order differential dual-band BPF [77]. The structure of the conventional quadruple-mode SRLR is shown in Fig. 4.1(a), which consists of a one-wavelength square ring resonator (blue line sections, $L_r$) and two open microstrip lines (pink line sections, $L_s$) which are attached to both sides of the ring. Because the SRLR in Fig. 4.1(a) is not a fully symmetric structure, it is actually difficult to be used to design high-order dual-band BPFs with desired dual passband properties.

In this section, a modified multimode SRLR is proposed and its configuration is presented in Fig. 4.1(b). Compared with the conventional one in Fig. 4.1(a), the proposed structure has two modifications. First, the uniform-impedance open microstrip lines in Fig. 4.1(a) are replaced by the T-shaped branches in Fig. 4.1(b). Second, the T-shaped branches are loaded at the center of the vertical sides of the square ring, and the new resonator becomes fully symmetric, which results    in    more    flexible    control    of    the    internal    coupling    between    two
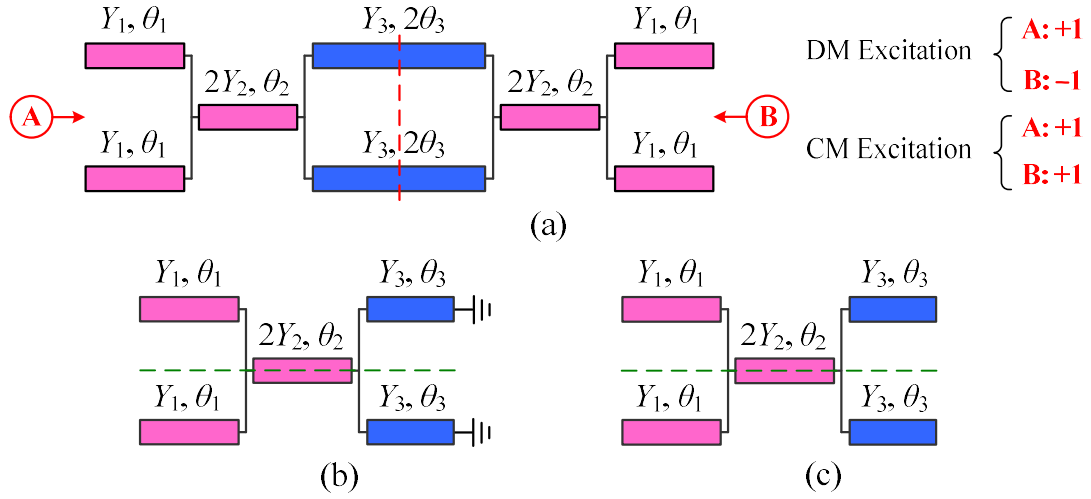
Fig. 4.2. (a) TLM of the proposed SRLR. (b) DM bisection. (c) CM bisection.

modified SRLRs at dual passbands and allows the proposed structure suitable for the design of high-order dual-band BPFs with desired midband frequencies and bandwidths.

To investigate the resonant characteristics of the modified SRLR, a transmission-line model (TLM) of the resonator is firstly built. By using the even-/odd-mode method twice, the DM and CM resonances of the resonator are analyzed in detail. Among the multiple resonances of the SRLR, two DM resonant modes are chosen for the design of dual-band BPFs. Furthermore, stepped impedance technique is applied to provide one more design freedom in controlling the DM resonances. Then, a fourth-order HTS dual-band BPF is designed based on the modified SRLR. Detailed design procedure, including the internal and external coupling design, is given, and from which, it is made clear that by using the proposed SRLRs, we can design dual-band BPFs with independent control of both the midband frequencies and the bandwidths of two passbands. Moreover, transmission zeros (TZs) are used to improve the selectivity of the filter, and the frequency dispersing technique is used widen the CM suppression range.

### 4.2.1 Analysis of the Modified SRLR

The TLM of the proposed modified SRLR in Fig. 4.1(b) is shown in Fig. 4.2(a). It consists of eight transmission-line (TL) sections, with $\theta_1$, $\theta_2$, and $\theta_3$ denote the electrical lengths corresponding respectively to the physical lengths of $L_1$, $L_2$, $L_3$ and are given by $\theta_1 = \beta L_1$, $\theta_2 = \beta L_2$, $\theta_3 = \beta L_3$, where $\beta$ is the propagation constant of the microstrip line. $Y_1$, $Y_2$, and $Y_3$ indicate the corresponding characteristic admittances with associated physical widths of $w_1$, $w_2$, and $w_3$. $\theta_1 = \theta_2$ and $Y_1 = Y_2$ are assumed to simplify the analysis and design below.
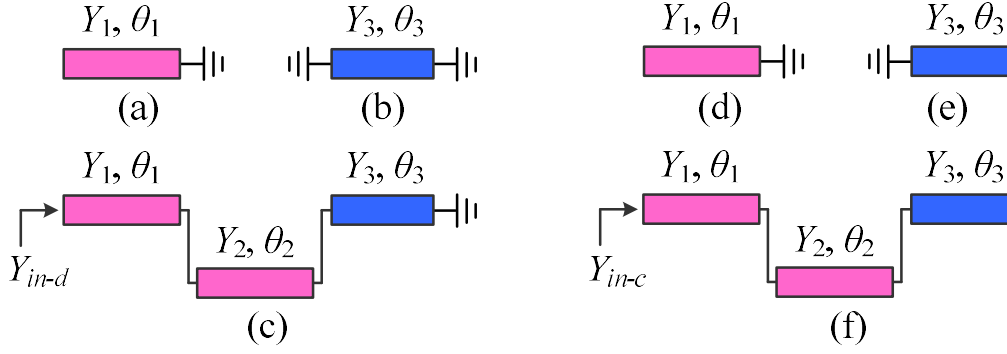
Fig. 4.3.　(a) Odd-mode EC I, (b) Odd-mode EC II, and (c) Even-mode EC of the DM bisection. (d) Odd-mode EC I, (e) Odd-mode EC II, and (f) Even-mode EC of the CM bisection.

Since the circuit in Fig. 4.2(a) is a symmetric structure, it can be readily analyzed by using the well-known even- and odd-mode method. In the case of odd-mode excitation (with respective to DM excitation), the symmetrical plane (red dashed line) of the circuit is an electrical wall (E.W.), and the circuit is simplified as shown in Fig. 4.2(b). For the even-mode excitation (with respective to CM excitation), the symmetrical plane is a magnetic wall (M.W.), and the simplified circuit is given in Fig. 4.2(c). It is interesting to note that these DM and CM bisection circuits are still symmetric structures with respective to the dashed lines in Figs. 4.2(b) and (c), so the even-and odd-mode operation can be conducted again in the second-round of analysis. The corresponding odd- and even-mode equivalent circuits (ECs) of the DM and CM bisections are depicted in Figs. 4.3(a)-4.3(f). After two rounds of even- and odd-mode operation, much simplified transmission line circuits of the proposed resonator are obtained in Figs. 4.3(a)-4.3(f), and they will be analyzed in detail below.

## 4.2.1.1 Analysis of the DM Resonances

The circuits in Figs. 4.3(a)-4.3(c) of the DM bisection are studied first to investigate DM resonances. It is seen from Fig. 4.3 that the former two ECs are the basic uniform-impedance resonators (UIR), and their corresponding DM frequencies, indicated as $f_{d1}$ and $f_{d2}$, are expressed by

$$f_{d1} = \frac{c}{4L_1\sqrt{\varepsilon_{eff}}} \tag{4.1}$$

$$f_{d2} = \frac{c}{2L_3\sqrt{\varepsilon_{eff}}} \tag{4.2}$$
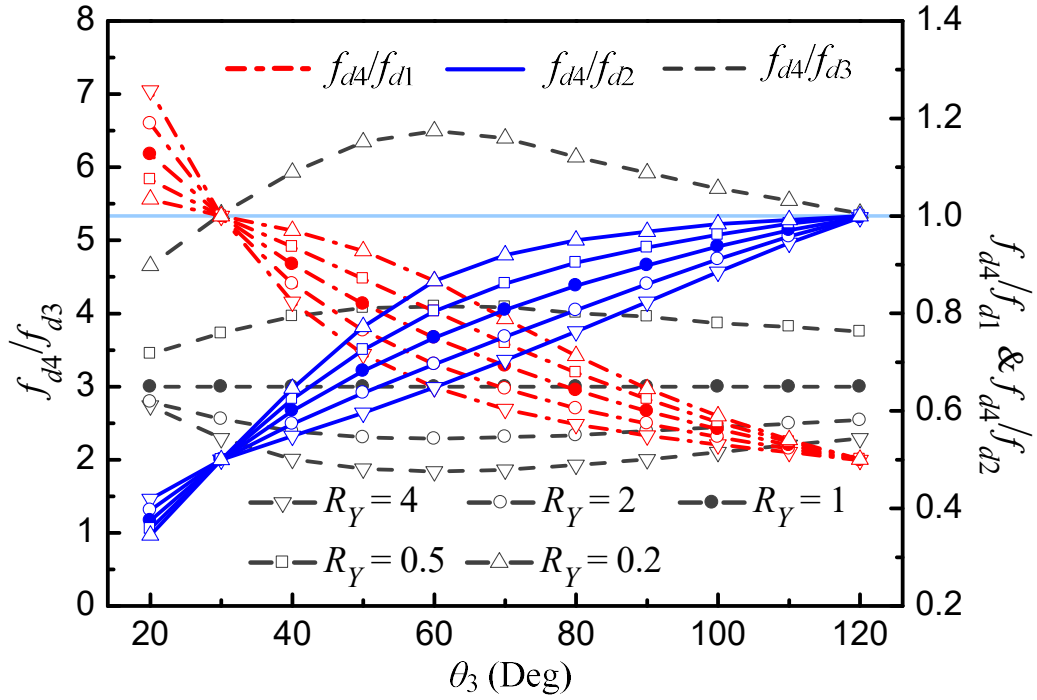
Fig. 4.4. Variations of the frequency ratios ($f_{d4}/f_{di}$, $i = 1, 2, 3$) of DM resonances versus $\theta_3$ with $\theta_1 = 30°$ and different $R_Y$.

where $c$ is the speed of light in the free space and $\varepsilon_{eff}$ is the effective dielectric constant of the substrate. For the even-mode case, as shown in Fig. 4.3(c), the EC is a stepped-impedance resonator (SIR). Its one port input admittance can then be derived as

$$Y_{in-d} = Y_1 \frac{Y_L + jY_1 \tan(2\theta_1)}{Y_1 + jY_L \tan(2\theta_1)} \tag{4.3}$$

where

$$Y_L = -jY_3 \cot\theta_3. \tag{4.4}$$

Submitting (4) into (3) and let $Y_{in-d} = 0$, the resonant condition of the third DM resonator in Fig. 3(c) are deduced as

$$\tan(2\theta_1)\tan\theta_3 = Y_3 / Y_1 = R_Y \tag{4.5}$$

The first two solutions of (4.5), indicated as $f_{d3}$ and $f_{d4}$, are the DM resonant frequencies of the SIR in Fig. 4.3(c), and are determined by both the electric lengths, $\theta_1$ and $\theta_3$, and the admittance ratio $R_Y$.

From (4.1), (4.2) and (4.5), we can obtain four DM resonances, from which we need to

Table 4.1

Specific Cases for DM Frequencies Comparison With Different Electrical Length And Admittance Ratio Combinations From Fig. 4.4.

| TLM No. & Type | TLM1, UIR | TLM2, UIR | TLM3, SIR |
|---|---|---|---|
| Structure | $Y_1, \theta_1$ | $Y_3, \theta_3$ | $Y_1, 2\theta_1$ $Y_3, \theta_3$ |
| Resonance | $f_{d1}$ | $f_{d2}$ | $f_{d3}$ & $f_{d4}$ ($f_{d3} < f_{d4}$) |
| Case 1 | $R_Y = 1, \theta_3 \leq 2\theta_1 \leq 2\theta_3$ | | $f_{d4} = 3f_{d3} \leq f_{d1} \leq f_{d2}$ |
| Case 2 | $R_Y = 1, \theta_3/2 \leq 2\theta_1 < \theta_3$ | | $f_{d4} = 3f_{d3} \leq f_{d2} < f_{d1}$ |
| Case 3 | $R_Y > 1, \theta_3 \leq 2\theta_1 \leq 2\theta_3$ | | $f_{d4} < 3f_{d3}$ & $f_{d4} \leq f_{d1} \leq f_{d2}$ |
| Case 4 | $R_Y > 1, \theta_3/2 \leq 2\theta_1 < \theta_3$ | | $f_{d4} < 3f_{d3}$ & $f_{d4} \leq f_{d2} < f_{d1}$ |
| Case 5 | $R_Y < 1, \theta_3 \leq 2\theta_1 \leq 2\theta_3$ | | $f_{d4} > 3f_{d3}$ & $f_{d4} \leq f_{d1} \leq f_{d2}$ |
| Case 6 | $R_Y < 1, \theta_3/2 \leq 2\theta_1 < \theta_3$ | | $f_{d4} > 3f_{d3}$ & $f_{d4} \leq f_{d2} < f_{d1}$ |
| Case 7 | $\theta_1 > \theta_3$ | | $f_{d3} < f_{d1} < f_{d4} < f_{d2}$ |

choose the lowest two modes to form the DM dual passbands. Based on (4.1), (4.2), and (4.5), the variation of frequency ratios ($f_{d4}/f_{di}$, $i = 1, 2, 3$) of DM resonances versus $\theta_3$ with $\theta_1 = 30°$ and different $R_Y$ are provided in Fig. 4.4. All electrical lengths are given at $f_0 = 2.325$ GHz, which is the midband frequency of the lower passband of the dual-band BPF to be designed. It is observed that $f_{d4}/f_{d2}$ is always smaller than or equal to 1 while $f_{d4}/f_{d1}$ is larger than 1 with $\theta_3 < 30°$ and $f_{d4}/f_{d1}$ is smaller than or equal to 1 with $\theta_3 \geq 30°$. Also, $f_{d4}/f_{d3}$ is larger than 3 when $R_Y$ is smaller than 1 as well as $f_{d4}/f_{d3}$ is smaller than 3 when $R_Y$ is larger than 1. For convenience, seven typical cases are concluded from Fig. 4.4 and illustrated in Table 4.1. Thus, one available case with determination of the former two lower DM resonances can be chosen from Table 4.1 based on the design requirement.

### 4.2.1.2 Analysis of the CM Resonances

The ECs of CM bisection are shown in Fig. 4.3(d), (e), and (f) after the second even- and odd-mode operation. Apparently, the former two ECs are the quarter-wavelength UIRs and the third one is a SIR. Naturally, they will generate multiple CM resonant frequencies, which degrading the holistic performance of the differential system. An effective way is to offset the CM

resonances with the DM resonances through appropriate design of the resonator. From
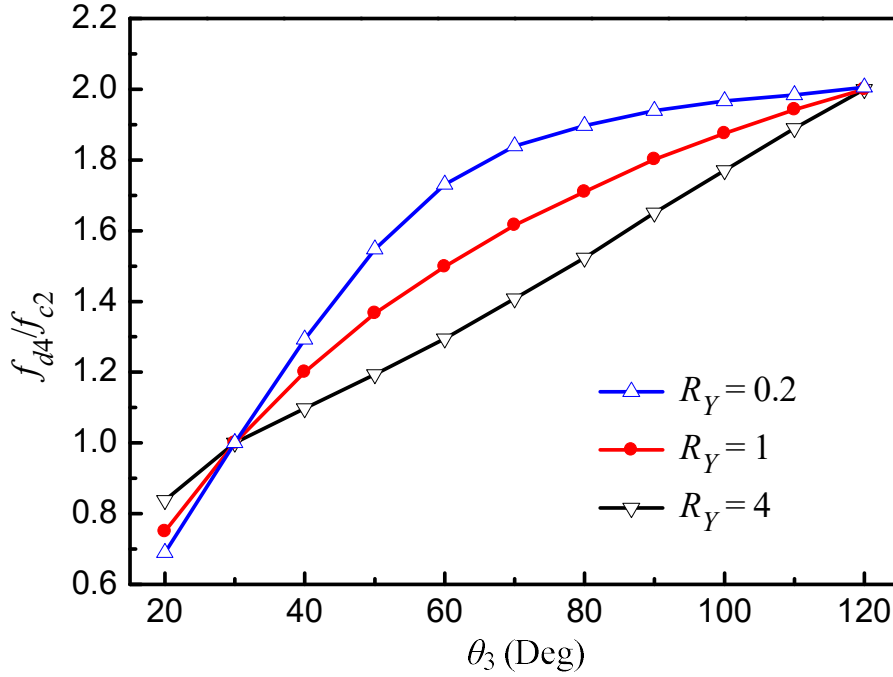


Fig. 4.5.    Variation of $f_{d4}/f_{c2}$ versus $\theta_3$ under different $R_Y$ with $\theta_1 = 30°$.

the solutions of the equations for the CM resonances and DM resonances discussed above, it is found that the DM resonance of Fig. 4.3(c), indicated by $f_{d4}$, and the CM resonance of Fig. 4.3(e), indicated as $f_{c2}$, may happen to occur most closely. Fig. 4.5 illustrates the variation of frequency ratio ($f_{d4}/f_{c2}$) versus $\theta_3$ when $R_Y$ is equal to 0.2, 1 and 4, respectively. It is clear to see that $f_{d4}/f_{c2}$ is equal to 1 when $\theta_3$ is chosen to be 30°. This means that $f_{c2}$ will be shifted to $f_{d4}$ when $\theta_3$ approaches to 30°, and in our design, $\theta_3$ should be chosen a value far from 30°.

In addition, it is obvious that Fig. 4.3(a) and Fig. 4.3(d) have the same EC, which means the DM frequency $f_{d1}$ of Fig. 4.3(a) is equal to the CM frequency $f_{c1}$ of Fig. 4.3(d). From the view of CM suppression, $f_{d1}$ is not a suitable resonance to constitute the DM passband.

### 4.2.1.3 Behaviors of the Holistic Resonator

For demonstration, Case 1 in Table 4.1 is chosen to examine the frequency property of the proposed modified multimode SRLR. According to the limitation for electrical lengths in Case 1, we assume $\theta_1 = \theta_2 = 30°$, $\theta_3 = 42°$, and $Y_1 = Y_2 = 0.0143$ S. $Y_3$ is then 0.0143 S as $R_Y = 1$. The substrate used in this paper is MgO with a relative dielectric constant of 9.78 and a thickness of 0.5 mm. From the above electrical parameters, and by using the commercial simulation tool Advance Design System (ADS) and the Electromagnetic (EM) simulator *Sonnet* em, the

microstrip configuration of the modified SRLR is drawn in Fig. 4.6(a) with its
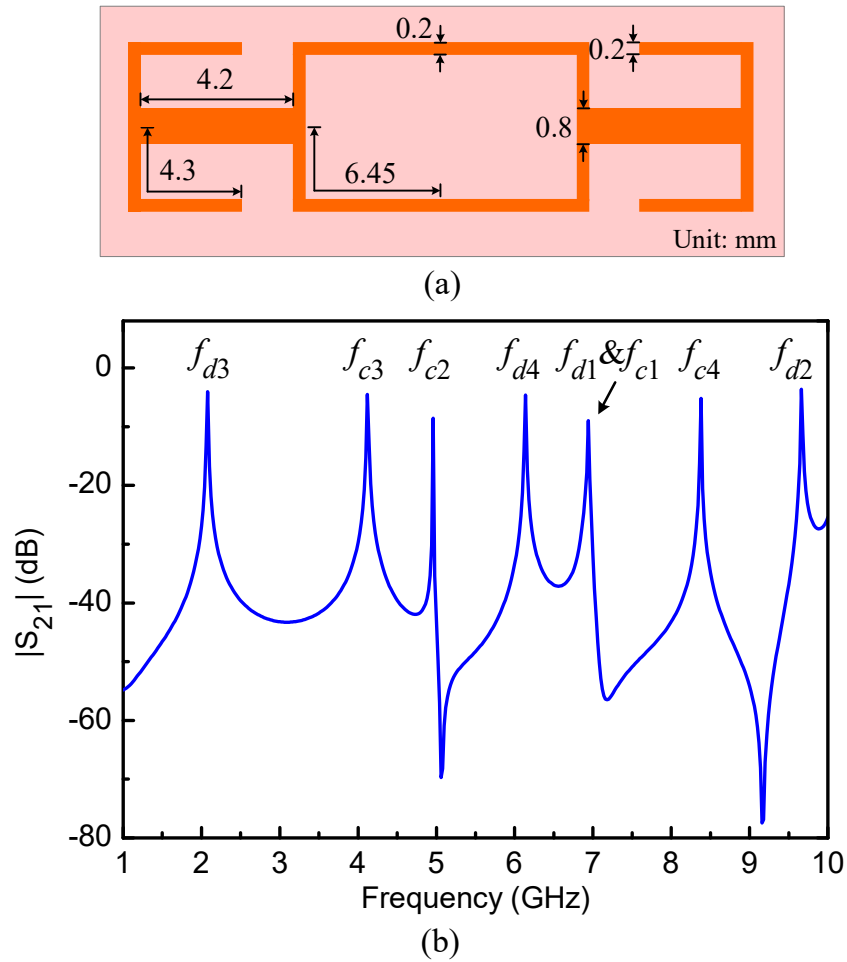


Fig. 4.6.　(a) Unit Configuration of the proposed modified SRLR.
(b) |S₂₁| of the proposed modified SRLR under weak coupling.

geometrical dimensions. Fig. 4.6(b) plots its frequency response under weak coupling. It is shown that four DM resonances, indicated as $f_{d3}$, $f_{d4}$, $f_{d1}$, $f_{d2}$ in sequence, and four CM resonances, identified as $f_{c3}, f_{c2}, f_{c1}, f_{c4}$ in turn, are observed. The four DM resonances occur in a sequence as given in Table I, and $f_{d1}$ and $f_{c1}$ happen at the same position. The EM simulated frequencies of the seven DM and CM modes, as shown Fig. 4.6(b), are 2.06, 4.12, 4.96, 6.14, 6.95, 8.38, and 9.66 GHz, respectively. On the other hand, the calculated seven frequencies from the derived equations based on the ECs in Fig. 4.3(a)-4.3(f) are 2.05, 4.10, 4.98, 6.15, 6.96, 8.20, and 9.96 GHz. Thus, good agreement is observed between the analytical calculation and the EM simulation results. Larger discrepancies between the last two modes are found because of the parasitic effect and loading effect of the proposed resonator in microstrip configuration.

It is interesting to note that some of the above DM and CM resonances cannot be well
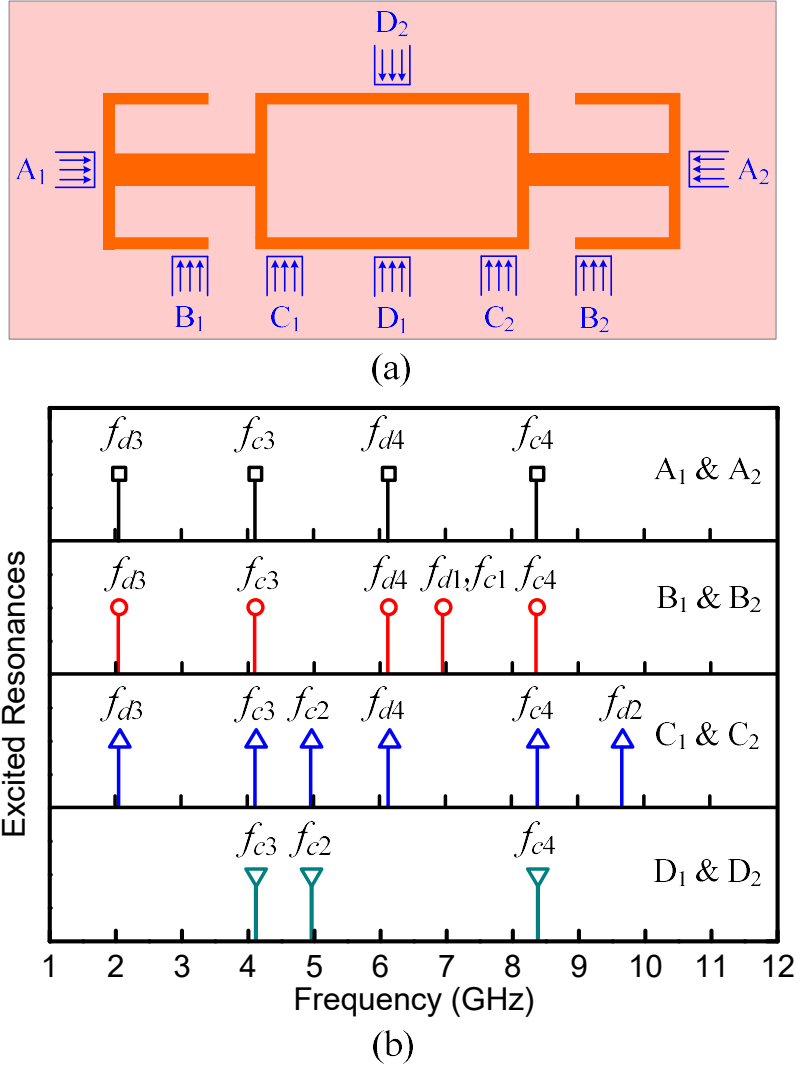
Fig. 4.7.   (a) Schematic of four pairs of positions of I/O port on the proposed modified SRLR. (b) Excited resonances of   the modified SRLR when using four different pairs of feeding points with weak coupling.

excited when the feeding point of the resonator is placed at a null-voltage position of the associated resonant modes. By referring to the ECs shown in Fig. 3, four pairs of feeding points, i.e., $A_1$ & $A_2$, $B_1$ & $B_2$, $C_1$ & $C_2$, and $D_1$ & $D_2$, are chosen to excite the proposed resonator, as shown in Fig. 7(a). The dimensions of resonator are the same as the ones illustrated in Fig. 6(a). By using these different pairs of feeding points, different resonances of the modified SRLR are excited, as shown in Fig. 7(b). When the feeding pairs are $D_1$ & $D_2$, all DM resonances are not excited because the symmetrical plane (the broken line) of the DM bisection of the SRLR in Fig. 2(b) becomes an electrical wall or a magnetic wall with the symmetrical feedings at points $D_1$ & $D_2$. Therefore, $D_1$ & $D_2$ will not be considered as feeding points in the following design. Mode $f_{d3}$, $f_{c3}$, $f_{d4}$, and $f_{c4}$, are well excited with any feeding pairs except $D_1$ & $D_2$. On the other hand, mode $f_{d1}$ and $f_{c1}$ (circuit Fig. 3(a) and (d)) are excited
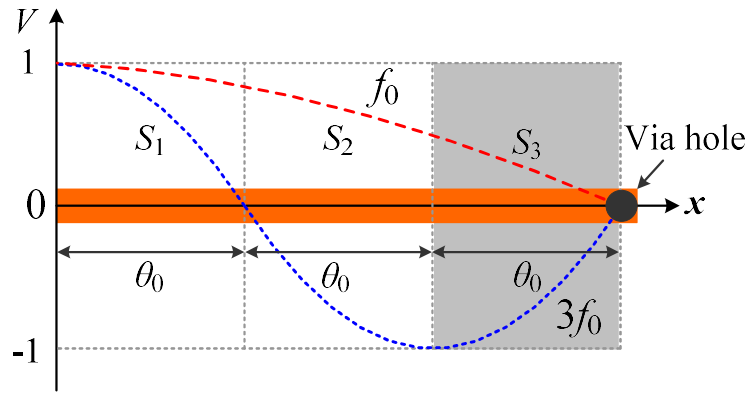
Fig. 4.8.    Voltage distributions of the fundamental mode $f_0$ and the first-order harmonic $3f_0$ on a quarter-wavelength UIR.

only when the feeding pairs are $B_1$ & $B_2$, at which the open stubs are excited. Also, when the feeding pairs are $C_1$ & $C_2$, mode $f_{d2}$ (circuit Fig. 3(b)) will appear, because the square ring can be stimulated with feedings at $C_1$ & $C_2$. The above discussion is very important to determine the I/O structure for realizing the desired DM response while reducing CM resonances in a wide frequency range.

### 4.2.2 Fourth-Order Dual-Band HTS Differential Filter Design

In this part, the modified multimode SRLR is employed to constitute a high-performance dual-band differential BPF with two passbands operating at 2.325 GHz and 4.900 GHz, respectively. Below are detailed descriptions on the design of the resonator, the internal coupling between two adjacent resonators, the external coupling between the resonator and the feed line, as well as discussions on the CM suppression.

#### 4.2.2.1 Design of the Resonator

As a result of the investigation in Section 4.2.1, mode $f_{d3}$ and $f_{d4}$ are chosen to form the two passbands of the dual-band differential BPF. So, at first, we need to design the modified SRLR with its mode $f_{d3}$ and $f_{d4}$ resonating at 2.325 GHz and 4.900 GHz, respectively. From Fig. 4.4, we see that $R_Y$ can be chosen as 3 as $f_{d4} / f_{d3} = 2.1 < 3$. Since $R_Y$ is larger than 1, then from Table 4.1, it is seen that both Case 3 and Case 4 are suitable solutions. Then if we choose $w_1 = 0.2$ mm and $R_Y = 3$, we get $w_3 = 1.7$ mm. The resonator as shown in Fig. 4.1(b) will be very large when the strip width $w_3$ of the ring is 1.7 mm. In order to avoid the large circuit size of the circuit, we made further modification of the resonator as follows.
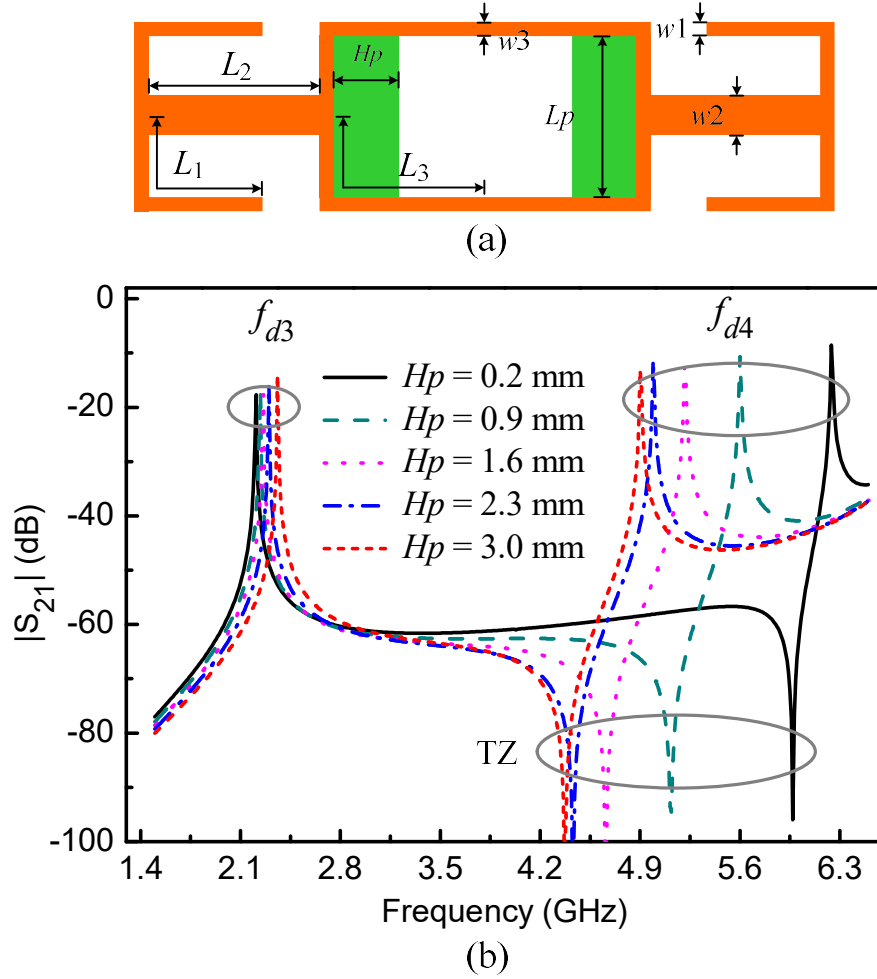
Fig. 4.9.  (a) The structure of the modified SRLR with two tunable metal patches.
(b) $H_p$-dependence of $|S_{21}|$ under DM weak excitation.

Firstly, we assumed $R_Y = Y_3/Y_1 = 1$, then the transmission circuit corresponding to mode $f_{d3}$ and $f_{d4}$, as shown in Fig. 4.3(c) (where we have assumed $Y_2 = Y_1$), becomes a quarter-wavelength UIR, as redrawn in Fig. 4.8. The red dashed line and the blue dotted line indicate the voltage distributions of the fundamental mode $f_0$ ($f_{d3}$) and the first higher harmonic $3f_0$ ($f_{d4}$) on the resonator, respectively. It is seen that the voltage distribute of the fundamental mode $f_0$ in the gray region $S_3$ near the short-circuited end is very small. Therefore, by loading metal patches in region $S_3$, it will have little effect on the fundamental mode, but will change the first harmonic mode significantly.

Based on the above discussion, two metal tuning patches are symmetrically loaded to the square ring of the previously proposed SRLR, and the new configuration of the resonator is depicted in Fig. 4.9(a). $L_p$ and $H_p$ are the width and length of loaded patch, respectively. In the design, $L_p$ is kept unchanged and is equal to the width of square ring, while $H_p$ is changeable
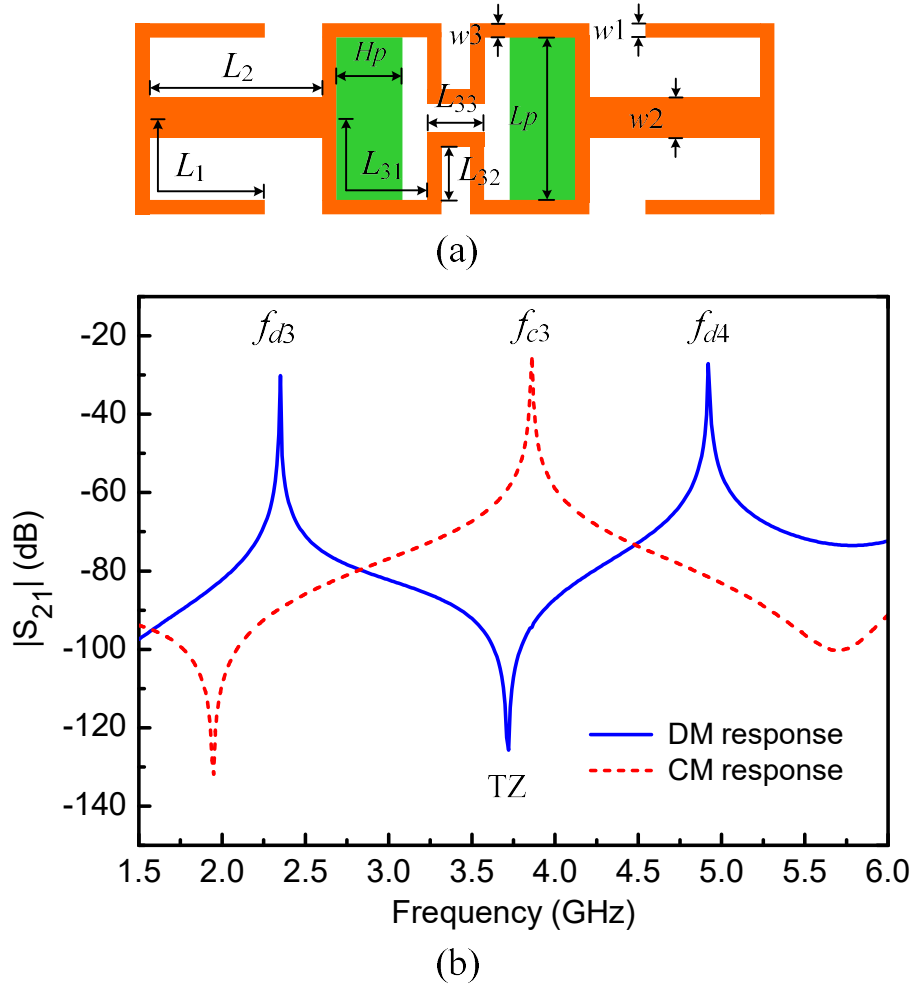
Fig. 4.10.    (a) Unit configuration of the compact modified SRLR. (b) Frequency response of $S_{21}$ magnitude under DM and CM weak excitation when $Hp$ = 2.8 mm.

and used to control $f_{d4}$. Following the design considerations in in Part 4.2.1.3, we use the initial values of $\theta_1 = \theta_2 = 30°$, $\theta_3 = 42°$, $R_Y = 1$ and $Y_1 = Y_2 = 0.0143$ S to continue the design of the resonator. Then $L_1$, $L_2$, $L_3$, $w_1$, $w_2$, and $w_3$ in Fig. 4.9(a) are determined readily with mode $f_{d3}$ occurring at about 2.325 GHz. Fig. 4.9(b) illustrates the variation of $|S_{21}|$ of the new resonator under weak feeding versus different length $H_p$ of the loaded patch. It is obvious that $f_{d4}$ reduces significantly while $f_{d3}$ increases a little as $H_p$ is increased, and this agrees with the above discussion. It also verifies the validity of the proposed tuning method of the resonant mode frequencies, and suggests that we can make independent controllable of the two desired DM frequencies ($f_{d3}$ and $f_{d4}$) of the modified SRLR with two tuning patches.

To further reduce the resonator size, the central parallel strips of the ring are folded as shown in Fig. 4.10(a). After optimized design by *Sonnet em*, the dimensions noted in Fig.
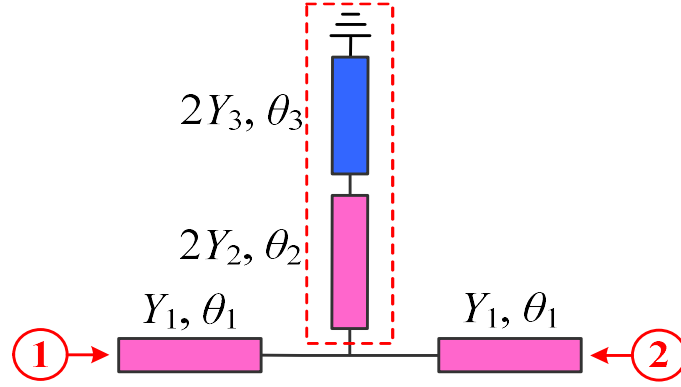
Fig. 4.11.  Simplified TLM for production of the inherent TZ.

4.10(a) are obtained as follows: $L_1 = 4.2$, $L_2 = 3.8$, $L_{31} = 4.9$, $L_{32} = 1$, $L_{33} = 1.3$, $w_1 = 0.2$, $w_2 = 0.5$, $w_3 = 0.2$, $H_p = 2.8$, and $L_p = 3$ (unit: mm). Under DM and CM excitation of this resonator, the corresponding DM and CM frequency responses are obtained and drawn in Fig. 4.10(b). It is observed that two desired DM resonances, $f_{d3}$ and $f_{d4}$, operating at 2.325 GHz and 4.900 GHz are got, which meet the design specifications well. Meanwhile, one transmission zero (TZ) in between two DM resonances is also observed, which is the inherent TZ of the proposed modified SRLR. Fig. 4.11 exhibits the simplified TLM for production of the inherent TZ, which is developed from the circuit of DM bisection shown in Fig. 4.2(b). It is seen that this TLM behaves as a basic center-stub-loaded resonator and one TZ will therefore be produced by the loaded stub [66]. The location of this TZ is determined by the size of loaded stub, that is the size of the square ring ($2Y_3$, $\theta_3$) and part of the loaded stub ($2Y_2$, $\theta_2$) in this design. In addition, the CM resonance $f_{c3}$, occurring at about 3.800 GHz, is unwanted, and its suppression will be discussed later.

Fig. 4.12 exhibits the distribution of electric-field density of the proposed SRLR at different resonant modes. It is shown that at $f_{d3}$, the electric-field is mainly concentrated on the loaded stubs at the two sides of the resonator, whereas at $f_{d4}$, strong field distributions are observed at both the loaded stubs and the loaded patches. At both DM resonances, $f_{d3}$ and $f_{d4}$, very weak field distribution is found at the central part of the resonator, which is due to the short-circuited end of the circuit in Fig. 4.3(c) for mode $f_{d3}$ and $f_{d4}$. In contrary, at the CM resonance $f_{c3}$, strong field distribution is also found at the central part of the resonator, which is due to the right open-circuited end of the circuit in Fig. 4.3(f) for mode $f_{c3}$ and $f_{c4}$. This discrepancy of field distribution between the DM and CM resonances will be utilized to suppress CM resonances later by adding some auxiliary stubs to the resonator at its central
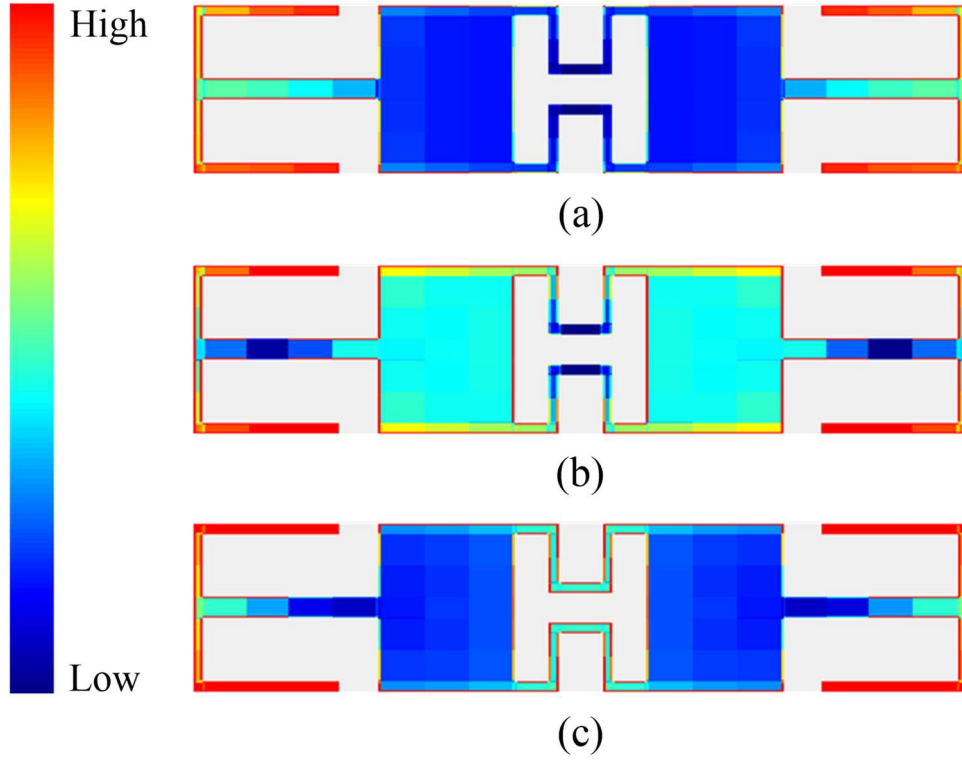
Fig. 4.12. Simulated electric-field density distributions of the resonator at resonance of (a) $f_{d3}$ = 2.325 GHz, (b) $f_{d4}$ = 4.900 GHz, and (c) $f_{c3}$ = 3.800 GHz.

part.

## 4.2.2.2 Design of the Internal Coupling between two SRLRs

After the above comprehensive study on the modified SRLR, a fourth-order dual-band differential BPF will be designed. The two DM passbands having Chebyshev response with 0.04321-dB ripple level are specified at 2.325 GHz and 4.900 GHz, with corresponding fractional bandwidth (FBW) of 3.9% and 4.9%, respectively. The microstrip configuration of the filter is shown in Fig. 4.13(a), and its coupling scheme under DM operation is in Fig. 4.13(b), where nodes $S$ and $L$ denote input and output ports, respectively. Nodes $DM_1$ and $DM_2$ represent the two DMs of the modified SRLR at $f_{d3}$ and $f_{d4}$. R1, R2, R3, and R4 indicate the four SRLRs. There are two coupling paths in the figure, corresponding to the two passbands, Band I and Band II, of the dual-band BPF. Based on the general procedure of filter synthesis in [85], the normalized coupling matrix can be obtained as:

$$M_N = \begin{bmatrix} 0 & M_{s1} & 0 & 0 & 0 & 0 \\ M_{1s} & 0 & M_{12} & 0 & 0 & 0 \\ 0 & M_{21} & 0 & M_{23} & 0 & 0 \\ 0 & 0 & M_{32} & 0 & M_{34} & 0 \\ 0 & 0 & 0 & M_{43} & 0 & M_{4L} \\ 0 & 0 & 0 & 0 & M_{L4} & 0 \end{bmatrix}$$

$$= \begin{bmatrix} 0 & 1.0362 & 0 & 0 & 0 & 0 \\ 1.0362 & 0 & 0.91162 & 0 & 0 & 0 \\ 0 & 0.91162 & 0 & 0.70048 & 0 & 0 \\ 0 & 0 & 0.70048 & 0 & 0.91162 & 0 \\ 0 & 0 & 0 & 0.91162 & 0 & 1.0362 \\ 0 & 0 & 0 & 0 & 1.0362 & 0 \end{bmatrix}. \quad (4.6)$$

From (4.6), the required coupling parameters shown in Fig. 4.13(b) are obtained as: the coupling coefficients $m_{12}^{I} = m_{34}^{I} = 0.0355$, $m_{23}^{I} = 0.0273$, $m_{12}^{II} = m_{34}^{II} = 0.0446$ and $m_{23}^{II} = 0.0343$, the external quality factors $Q_{ex}^{I} = 23.9$ and $Q_{ex}^{II} = 19$, where the superscript I and II indicate the first and second passband, respectively. Below we will describe in sequence the design of the internal coupling space between two modified SRLRs and the resonator feeding structure by using *Sonnet em*, in order to realize the wanted coupling coefficients and external $Q$ values.

Fig. 4.14(a) shows the coupling structure of two adjacent SRLRs, in which $g_1$ is the space between the loaded stubs, and $g_2$ is the space between the loaded patches, and they are both used to adjust the coupling strength between two resonators. The field distributions in Fig. 4.12(a) and (b) for mode $f_{d3}$ and $f_{d4}$ suggest that the space $g_1$ between the loaded stubs will have influence on both mode $f_{d3}$ and $f_{d4}$, while the space $g_2$ between the loaded patches will have influence on mode $f_{d4}$ (Band II) but little influence on mode $f_{d3}$ (Band I). So, we can determine $g_1 = g_2$ at first to meet the coupling strength of Band I, and then vary $g_2$ to satisfy the coupling strength of Band II. Fig. 4.14(b) provides the computed variation of coupling coefficients versus the coupling space $g_1 = g_2$. It is seen that the coupling coefficients of both DM passbands decrease monotonously as $g_1 = g_2$ increases. From this figure, the space $g_{11}$ and $g_{12}$ shown in Fig. 4.13(a) are quickly obtained as 0.13 mm and 0.15 mm to obtain the
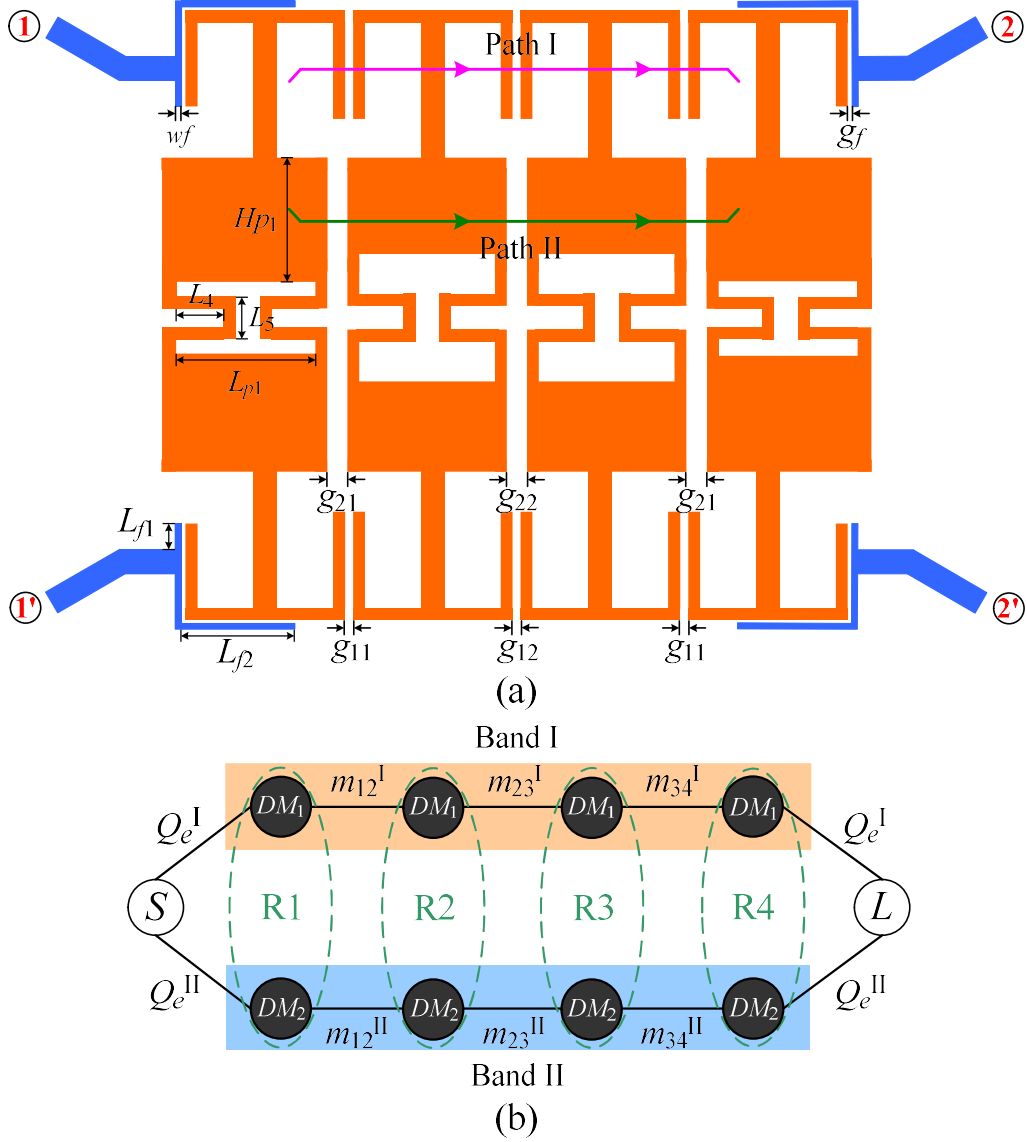
Fig. 4.13.    (a) Layout of the designed dual-band HTS differential filter. (b) Coupling diagram of the fourth-order dual-band filter under DM operation.

required $M_{12}^{I} = M_{34}^{I} = 0.0355$ and $M_{23}^{I} = 0.0273$ for Band I performance.

Fig. 4.15(a) and (b) show the simulated coupling coefficients curves of Band I and Band II versus the space $g_2$ when $g_1 = 0.13$ mm and $g_2 = 0.15$ mm, respectively. In both cases, the coupling coefficient of Band I varies little, while that of Band II decreases quickly. From these curves, the space $g_{21}$ indicated in Fig. 4.12(a) can be chosen as 0.26 mm and $g_{22}$ as 0.23 mm to realize the required $M_{12}^{II} = M_{34}^{II} = 0.0446$ and $M_{23}^{II} = 0.0343$ for Band II performance. In the above design, the space $g_1$ between the loaded stubs of two SRLRs is determined first with the assumption $g_1 = g_2$. Then the space $g_2$ between the loaded patches of two SRLRs is re-adjusted by moving the loaded patches. So, the loading positions of the stubs to the patches
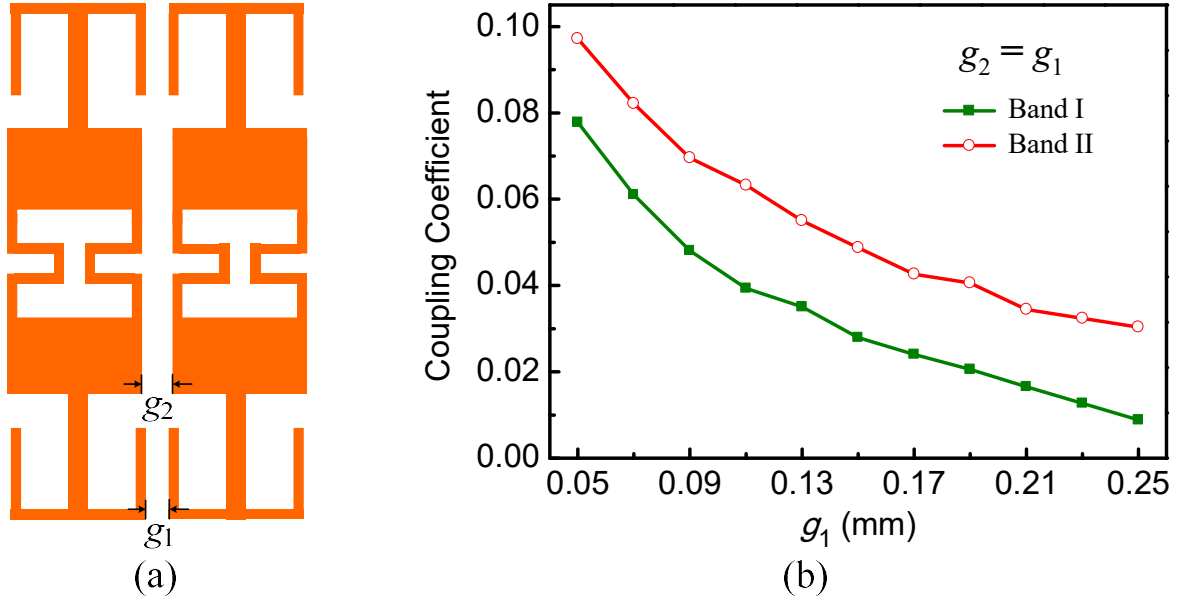
Fig. 4.14.    Configuration of two coupled modified SRLRs. (b) Coupling coefficients as a function of the coupling space $g_1 = g_2$ under weak DM excitation.

are changed with the variation of $g_2$. Fig. 4.16(a) displays the schematic diagram of the SRLR loaded with two movable T-shaped stubs, where $t$ denotes the loading position of the stub. The frequency variation of $f_{d3}$ and $f_{d4}$ versus $t$ is exhibited in Fig. 4.16(b). It is seen that the frequencies of both DM resonances are almost unchanged with $t$. This means that in the design of the internal coupling coefficients between two SRLRs by varying the space $g_1$ and $g_2$, the resonant frequencies of the two DMs, which are the midband frequencies of the two passbands, are kept unchanged. This is a very advantageous property of the newly proposed resonator.

### 4.2.2.3 Design of the External Coupling Structure

The following is to design the external coupling structure to meet the desired $Q_{ex}$ values of two passbands simultaneously. As shown in Fig. 4.17, the microstrip parallel coupled-lines are employed as the feeding structure in this design to provide enough design flexibility. From Fig. 4.7(b), it is seen that to suppress CM resonance excitation, feeding pairs at points $A_1$ & $A_2$, $B_1$ & $B_2$, in Fig. 4.7 are suitable choices. However, in the case of mode $f_{d4}$ (Band II), as displayed in Fig. 4.12(b), the field distribution at points $A_1$ & $A_2$ is very weak. So, it will difficult to acquire the desired $Q_{ex}$ for the second passband if the feeding points are placed at points $A_1$ & $A_2$. So, the points $B_1$ & $B_2$ are preferably chosen.

In the following design, as shown in Fig. 4.17, the line width $w_f$ of the coupling arm and the
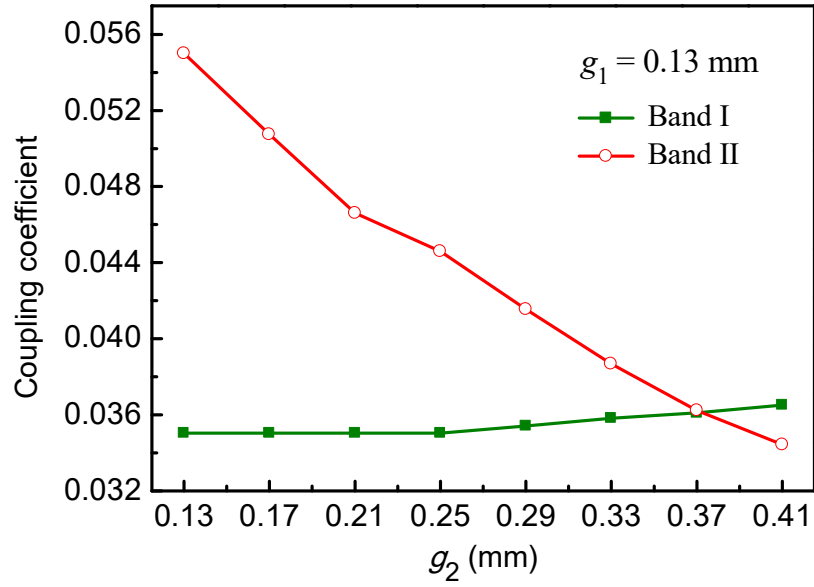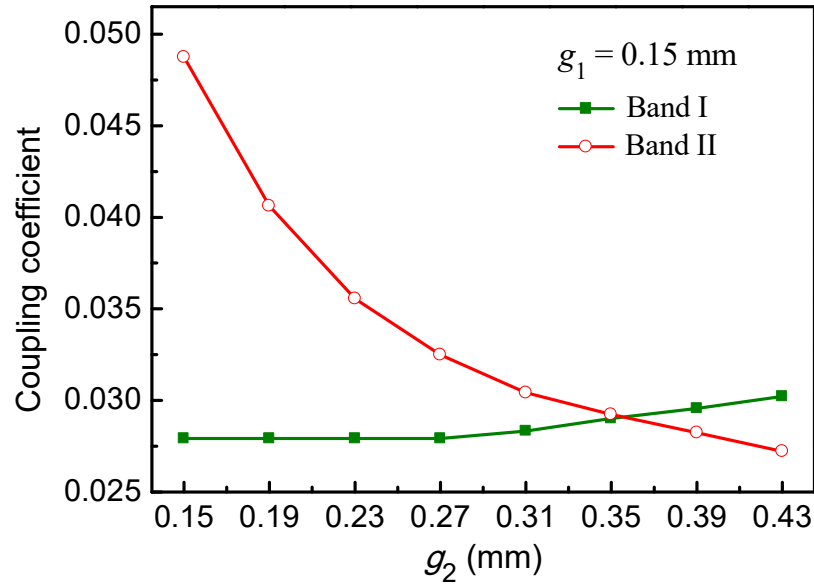
Fig. 4.15.   Simulated coupling coefficients as a function of $g_2$

(a) when $g_1$ =0.13 mm, and (b) when $g_1$ =0.15 mm.

coupling gap $g_f$ are fixed as 0.05 mm and 0.1 mm, respective. $L_{f1}$ and $L_{f2}$ represent the feeding position and the coupled-line length, respectively. Fig. 4.18 illustrates the design graph of $Q_{ex}$ for our dual-band BPF, where the superscript I and II of $Q_{ex}$ denote the first and second passband, respectively. From Fig. 4.18, proper combination of $L_{f1}$ and $L_{f2}$ can be chosen to meet the target external couplings at both passbands. Although the illustrated tuning ranges of $Q_{ex}^{I}$ and $Q_{ex}^{II}$ in Fig. 4.18 are limited, more design data can be extracted by choosing different
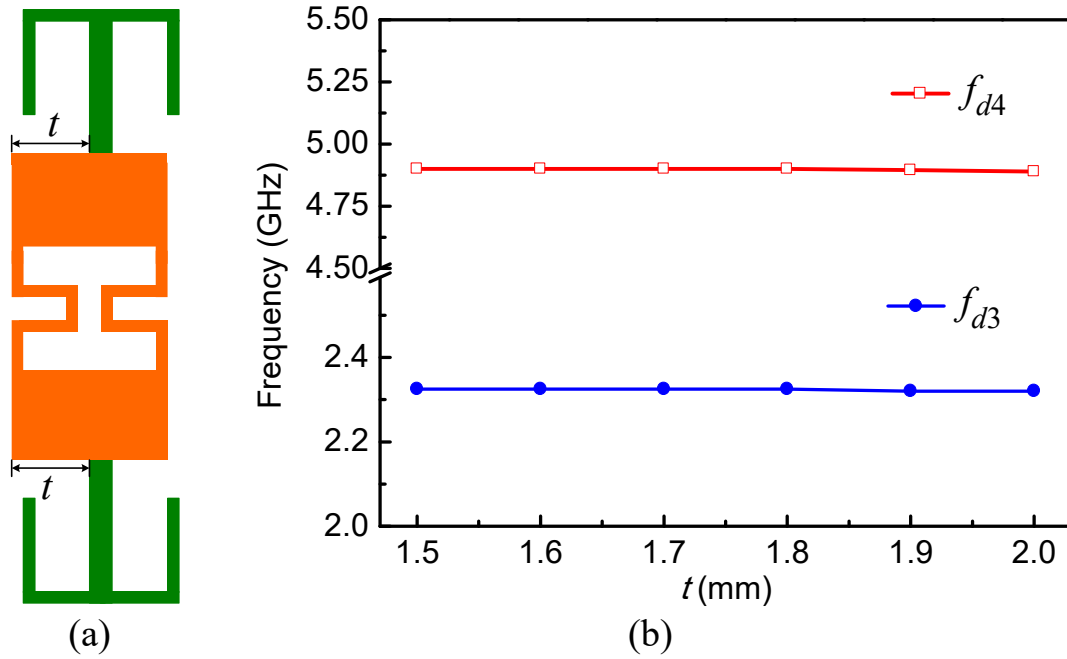
Fig. 4.16. (a) Schematic diagram of the modified SRLR with movable T-shaped stubs. (b) Frequency variation of the two DM resonances versus the loading position of $t$ of the stubs.
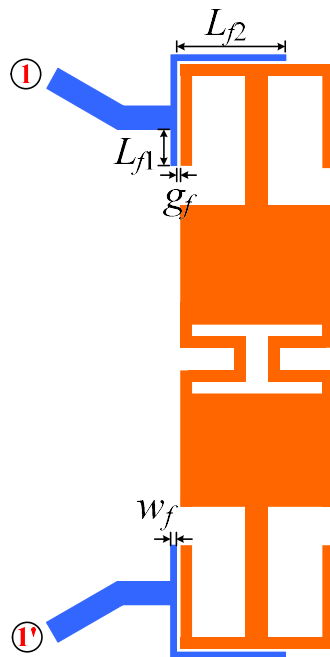


Fig. 4.17. Parallel coupled-line feeding structure of the proposed SRLR.

combinations of $L_{f1}$, $L_{f2}$, $w_f$, and $g_f$ when needed. Based on the required values of $Q_{ex}^{I}$ and $Q_{ex}^{II}$, $L_{f1}$ and $L_{f2}$ are finally determined as 0.9 mm and 2.8 mm, as shown in Fig. 4.18 by the red solid dot in the net-type graph. Residual geometrical parameters in the filter circuit indicated
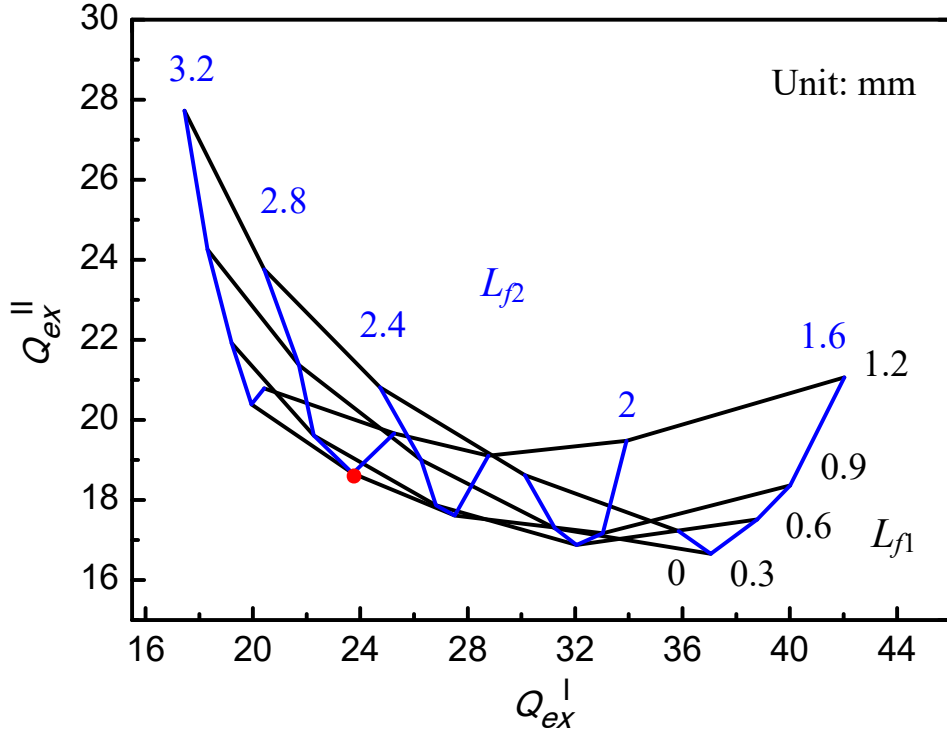
Fig. 4.18.   Simulated external quality factors of the two DM passbands with different feeding position $L_{f1}$ and coupled-line length $L_{f2}$, where $w_f = 0.1$ mm and $g_f = 0.05$ mm.

in Fig. 4.13(a) are optimized by *Sonnet em* as follows: $L_4 = 1.2$, $L_5 = 0.9$, $L_{p1} = 3.2$, and $H_{p1} = 3.5$, all in mm.

### 4.2.2.3 Design of the Fourth-Order Dual-Band Differential BPF

The design procedure of a dual-band differential BPF using the proposed modified SRLRs is summarized as follows.

1) In Fig. 4.9(a), deducing the physical length $L_3$ of the square ring with assumed $L_1$ and $L_2$, based on the required center frequency of the first passband and the separation between the CM and DM resonant frequencies. Then, adjusting the width $H_p$ of the inserted patches to get the location of the second passband.

2) Based on the desired coupling coefficients of two passbands, tuning the coupling space between the loaded stubs of SRLRs to meet the required bandwidth of the first passband at first. Then, tuning the coupling distance between the loaded patches of SRLRs to satisfy the bandwidth of the second passband.

3) Selecting proper feeding line structure and its geometrical parameters to meet the required external coupling of both passbands simultaneously.
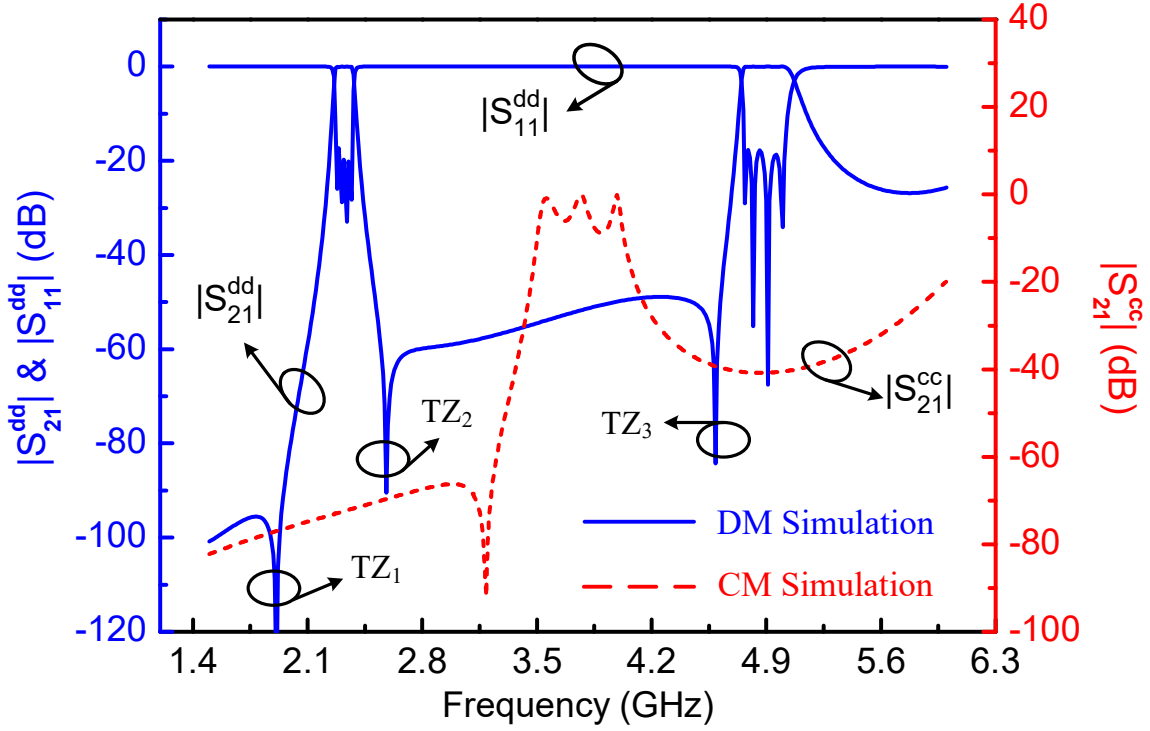
Fig. 4.19.    Simulated frequency response of the designed dual-band BPF.

4) Optimizing the overall filter circuit to obtain the desired performance of the designed BPF.

The finally simulated frequency response of the designed BPF under lossless condition is illustrated in Fig. 4.19. The solid blue lines represent the DM response and the dashed red line indicates the CM interference. It is observed from the DM response that two passbands are centered at 2.325 GHz and 4.900 GHz, and their corresponding FBW is 4% and 4.92%, respectively, which agree well with the desired specifications. Four reflection zeros are observed in each passband the return losses are better than 18 dB. In addition, three DM TZs, indicated by $TZ_1$, $TZ_2$, and $TZ_3$, are found in the vicinities of the DM passbands. Among them, $TZ_3$ is the inherent TZ of the proposed modified SRLR, as shown in Fig. 4.9(b), while $TZ_1$ and $TZ_2$ are produced by the transversal signal interference. As indicated in Fig. 4.13(a), there are two signal transmission paths, i.e., Path I and Path II, for each DM passband. When the phase difference of these two paths is 180° or odd times of 180°, a TZ will be created. From the electric-field distributions in Fig. 4.12(a) and (b), we judged that the adjacent coupled SRLRs operating at $f_{d3}$ provides an electric-coupling for Path I and a magnetic-coupling for Path II. While working at $f_{d4}$, the coupled resonators manifest an electric-coupling for both Path I and Path II. Table II lists the phase shifts for each signal path of the designed

Table 4.2

Phase Shifts of Each Path of The Fourth-Order Filter in Fig. 4.13

| | | | R1 | $M_{12}$ | R2 | $M_{23}$ | R3 | $M_{34}$ | R4 | Results |
|---|---|---|---|---|---|---|---|---|---|---|
| Band I | Below Resonance | Path I | +90° | -90° | +90° | -90° | +90° | -90° | +90° | 540° Out of Phase |
| | | Path II | +90° | +90° | +90° | +90° | +90° | +90° | +90° | |
| | Above Resonance | Path I | -90° | -90° | -90° | -90° | -90° | -90° | -90° | 540° Out of Phase |
| | | Path II | -90° | +90° | -90° | +90° | -90° | +90° | -90° | |
| Band II | Below Resonance | Path I | +90° | -90° | +90° | -90° | +90° | -90° | +90° | 0° In Phase |
| | | Path II | +90° | -90° | +90° | -90° | +90° | -90° | +90° | |
| | Above Resonance | Path I | -90° | -90° | -90° | -90° | -90° | -90° | -90° | 0° In Phase |
| | | Path II | -90° | -90° | -90° | -90° | -90° | -90° | -90° | |

fourth-order BPF. It is seen that at below resonance of the first passband, the two paths are out of phase and the same at above resonance. Two TZs will be generated on the low skirt and upper skirt of the first passband, as shown by $TZ_1$ and $TZ_2$ in Fig. 4.19. But for the second passband, the two paths are in phase wherever at below resonance or above resonance, leading to a Chebyshev response.

In view of the CM response in Fig. 4.19, it is observed that the minimum CM suppression is 72 dB within the first DM passband and 41 dB within the second DM passband. Unfortunately, there is CM resonance peaks between the two passbands, degrading the overall CM performance of the differential system. Therefore, the CM suppression of the filter in a wide frequency range need to be improved.

## 4.2.3 Wideband CM Suppression

As discussed in Section II, the proposed SRLR provides DM and CM resonances simultaneously. Consequently, both the DM and CM signals are transmitted from the input to output by the formed coupling paths, as illustrated in Fig. 4.13(a), resulting in thereby the poor CM suppression. Fortunately, the transmission of CM signals will be blocked when the
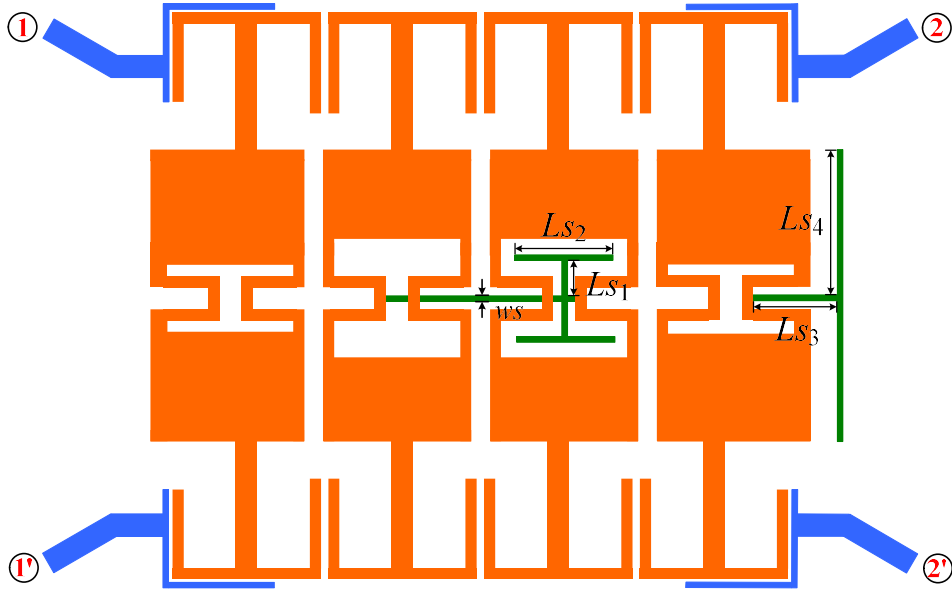
Fig. 4.20. Layout of the designed dual-band HTS differential BPF with multiple stubs loaded at the central symmetrical parts of the SRLRs.

CM resonances in adjacent resonators are separated by the frequency discrepancy technique, as studied in [25], [29], and [77].

Fig. 4.12 presents the simulated electric-field distributions of the proposed SRLR at three resonant modes. It is observed that the electric-field on the central part of resonator at two DMs are both near to null, while the electric-field at CM is relatively strong. Therefore, by loading microstrip stubs at the symmetric plane of the resonator, the CM resonances will be shifted while the DM resonances will be affected little.

Fig. 4.20 shows the sketch of the designed dual-band HTS differential BPF with multiple stubs loaded at the central symmetrical parts of the SRLRs. To enlarge the frequency discrepancy of two adjacent CMs, the second and third SRLRs are centrally connected by a narrow microstrip line. The third SRLR is loaded with two T-shaped stubs. The fourth SRLR is loaded with a longer T-shaped stub. Thus, the CM resonant frequencies of the four SRLRs are made all different, weakening the coupling strength among CM resonances. Then, the CM transmission is expected to reduce.

After optimized by the EM simulator *Sonnet em*, the parameters of the loaded stubs specified in Fig. 4.20 are obtained as follow: $L_{s1} = 0.9$, $L_{s2} = 2.3$, $L_{s3} = 2.4$, $L_{s4} = 4.1$, and $w_s = 0.1$ (unit: mm). The expected improved CM response is shown as the red solid line in Fig. 4.21. It is seen that the proposed approach achieves a favorable CM suppression of better than 20 dB in a wide frequency spectrum (from DC to 6 GHz). As predicted, the DM response in
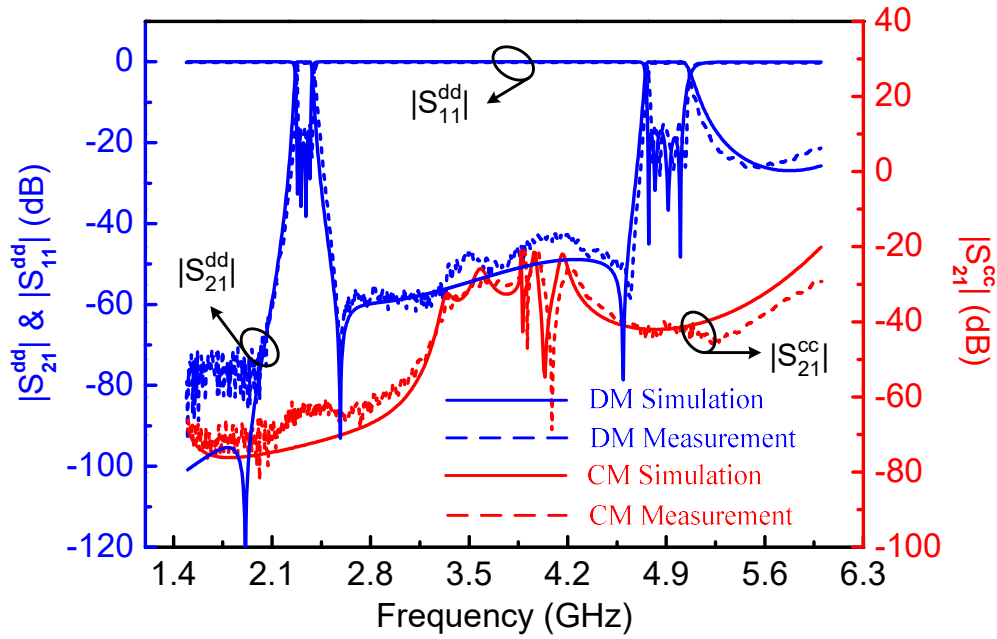
Fig. 4.21. Simulated and measured frequency responses of the final dual-band HTS BPF.
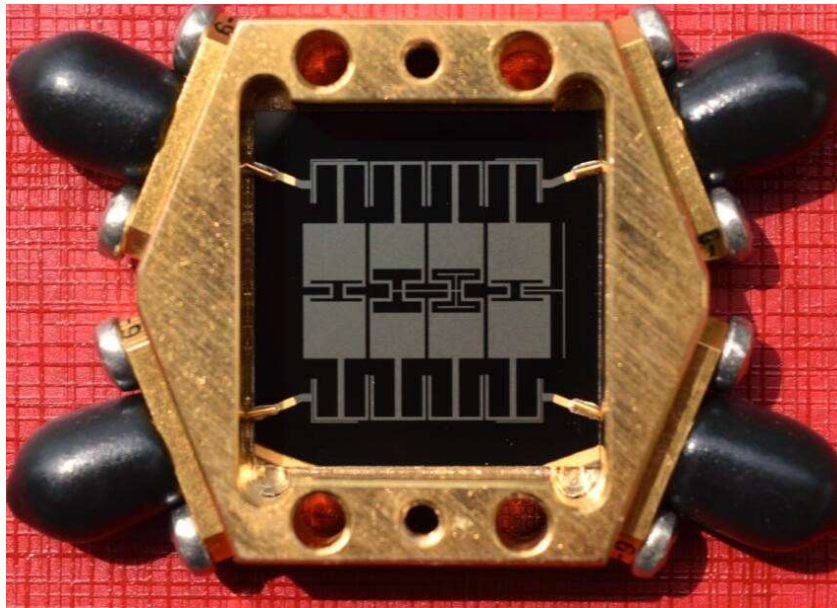


Fig. 4.22. Photograph of the fabricated HTS differential BPF with cover opened.

blue lines remains almost unchanged.

## 4.2.4 Experimental Results and Discussion

To verify the above design and the performance of the fourth-order differential BPF, the circuit shown in Fig. 4.20 is fabricated on a 0.5-mm-thick MgO wafer with double-sided YBCO films. The ion etching technology is used to etch the front-side film to form the circuit

Table 4.3

Comparison of Previous Fourth-Order Dual-Band Differential/Balanced Filters

| Ref. | Center Frequency (GHz) | 3-dB FBW (%) | Insertion Loss (dB) | In-Band CM Attenuation (dB) | Number of Pole In Passbands | Circuit Size ($\lambda_g \times \lambda_g$) | Controllable of Frequencies/ Bandwidths |
|---|---|---|---|---|---|---|---|
| [5] | 2.45 / 5.25 | 9.8 / 4.6 | 2.4 / 2.82 | 53 / 45 | 2 / 2 | 0.38 × 0.42 | Y / N |
| [6] | 2.46 / 5.56 | 16.3 / 6.7 | 1.9 / 1.9 | 36 / 31 | 3 / 2 | 0.31 × 0.41 | Y / N |
| [7] | 1.4 / 1.84 | 5.9 /5 | 1.95 / 2.32 | 25.5 / 25.4 | 2 / 1 | 0.25 × 0.21 | Y / Y |
| [7] | 1.835 / 2.45 | N/A | 2.2 / 2.6 | 20.5 / 20 | 2 / 2 | 0.19 × 0.29 | Y / Y |
| [11] | 2.4 /5 | 16.4 / 8.6 | 1.78 / 2.53 | 32 / 32 | 3 / 2 | 0.50 × 0.70 | Y / N |
| [15] | 9.47 / 9.96 | 2.9 / 3.1 | 1.89 / 1.73 | 30 / 30 | N/A | 2.87 × 2.95 | Y / N |
| [16] | 9.23 / 14.05 | 2.8 / 5.6 | 2.9 / 2.7 | 48 / 40 | 2 / 2 | 2.70 × 1.27 | Y / N |
| This work | 2.325 / 4.900 | 3.9 / 4.9 | **0.13 / 0.16** | **63 / 40** | **4 / 4** | 0.32 × 0.31 | Y / Y |

structure, and the circuit is mounted on a gold-plated metal carrier and then carefully packaged into a shield box. The photograph of the fabricated HTS BPF with cover opened is shown in Fig. 4.22. The fabricated filter, with the feeding lines excluded, occupies 16.1 × 15.9 mm$^2$, about 0.32 $\lambda_g$ × 0.31 $\lambda_g$, where $\lambda_g$ is the guide wavelength at 2.325 GHz.

The packaged dual-band differential BPF is cooled down to a temperature of 77 K in a cryogenic cooler and measured by a four-port vector network analyzer, Agilent E5071C. The measured results are drawn as blue and red broken lines in Fig. 4.21, which agree well with the simulated lines. For the DM response, the measured first and second passbands are centered at 2.325 and 4.900 GHz, respectively, with corresponding 3-dB passbands covering 2.26 - 2.38 GHz and 4.75 - 5.07 GHz, respectively. The maximum in-band insertion loss is approximately 0.13 dB and 0.16 dB, respectively, showing the low-loss superiority of the HTS technology. The measured return loss is better than 16 dB in both passbands. For the CM response, the measured minimum CM insertion loss is 63 dB in the first passband and 40 dB in the second passband, which show a good CM suppression level within DM passbands.
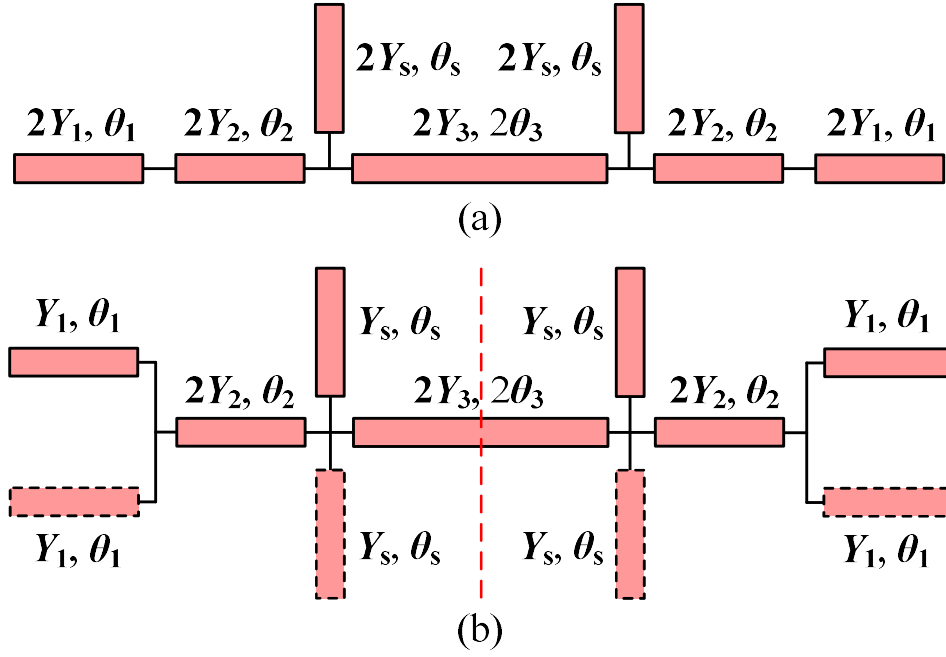
Fig. 4.23. (a) Conventional SLR. (b) The proposed modified SSLR.

Besides, from DC to 6 GHz, the CM suppression is better than 21 dB. Some slight deviation between the measurement and simulation is mainly due to the possible differences between the nominal and real values of the dielectric constant and substrate thickness.

In addition, a comparison of the proposed differential BPF with previous fourth-order dual-band differential filters is summarized in Table 4.3. It reveals that the proposed filter outperforms the others in terms of the insertion loss of DM passbands, in-band CM rejection, flatness of passbands, and the design flexibility.

## 4.3 Eighth-Order Dual-Band HTS Differential Bandpass Filter

From Fig. 4.21, it is observed that there is no transmission zero in the upper size of the second passband, resulting in a poor selectivity of the upper stopband. Also, the steepness of slope of the passbands as well as the attenuation in the stopband need to be improved. For these requirements, a novel multimode symmetric-stub-loaded resonator (SSLR) is proposed in this section and used to constitute an eighth-order dual-band HTS differential BPF with sharp rate of attenuation near the passband and deep CM suppression.

### 4.3.1 Analysis of the Multimode SSLR

The TLM model of the proposed multimode SSLR is shown in Fig. 4.23(b), which is developed from the conventional stub-loaded resonator (SLR) that given in Fig. 4.23(a). $\theta_1$, $\theta_2$,

Table 4.4. List of the obtained sub-circuits and the corresponding resonances

| DM/CM Analysis | DM Operation | CM Operation |
|---|---|---|
| DM/CM Bisection | $Y_1, \theta_1$   $Y_s, \theta_s$   $2Y_2, \theta_2$   $2Y_3, \theta_3$   $Y_1, \theta_1$   $Y_s, \theta_s$ | $Y_1, \theta_1$   $Y_s, \theta_s$   $2Y_2, \theta_2$   $2Y_3, \theta_3$   $Y_1, \theta_1$   $Y_s, \theta_s$ |
| Sub-Circuit Analysis | Even-mode Operation | Even-mode Operation |
| Even-mode Circuit of DM/CM Bisection | $Y_{d\text{-}in}$   $Y_1, \theta_1$   $Y_2, \theta_2$   $Y_s, \theta_s$   $Y_3, \theta_3$ | $Y_{c\text{-}in}$   $Y_1, \theta_1$   $Y_2, \theta_2$   $Y_s, \theta_s$   $Y_3, \theta_3$ |
| Even-mode Resonance | $f_{d1}, f_{d2}$   $(f_{d1} < f_{d2})$ | $f_{c1}, f_{c2}$   $(f_{c1} < f_{c2})$ |
| Sub-Circuit Analysis | Odd-mode Operation | Odd-mode Operation |
| Odd-mode Circuit of DM/CM Bisection | $Y_1, \theta_1$  \|  $Y_s, \theta_s$ | $Y_1, \theta_1$  \|  $Y_s, \theta_s$ |
| Odd-mode Resonance | $f_{d3}$  \|  $f_{d4}$ | $f_{c3}$  \|  $f_{c4}$ |

$\theta_3$, and $\theta$s denote the electrical lengths and $Y_1$, $Y_2$, $Y_3$, and $Y_s$ indicate the corresponding characteristic admittances. It is seen that two transmission line (TL) section ($2Y_1$, $\theta_1$) at two sides and two TL section ($2Y_s$, $\theta_s$) in the middle are respective split into four TL section ($Y_1$, $\theta_1$) and four TL section ($Y_s$, $\theta_s$) and such that a fully symmetric resonator is obtained. Thus, more flexible control of the internal coupling between two SSLR are thereby obtained and allows the proposed structure suitable for the design of high-order dual-band BPFs with desired bandwidths.

Since the circuit in Fig. 4.23(b) is a symmetric structure, it can be readily analyzed by using the well-known even- and odd-mode method. In the case of odd-mode excitation (with respective to DM excitation), the symmetrical plane (red dashed line) of the circuit is an electrical wall (E.W.), and the circuit is simplified as shown as Row 2 (R.2), Column 2 (C.2) in

Table 4.4. For the even-mode excitation (with respective to CM excitation), the symmetrical plane is a magnetic wall (M.W.), and the simplified circuit is given as R. 2, C. 3 in Table 4.4. It is interesting to note that these DM and CM bisection circuits are still symmetric structures with respective to the green dashed lines in Table 4.4, so the even-and odd-mode operation can be conducted again in the second-round of analysis. The corresponding odd- and even-mode equivalent circuits (ECs) of the DM and CM bisections are depicted in Table 4.4. After two rounds of even- and odd-mode operation, much simplified transmission line circuits of the proposed resonator are obtained, and they will be analyzed in detail below.

From Table 4.4, it is know that there are four DM resonances and four unwanted CM resonances in total. For constructing dual-band differential BPF, two of four DM resonances should be chosen appropriately. Because the odd-mode circuits of DM and CM bisections share the same TL counterparts, thus $f_{d3}$ and $f_{d4}$ are equal to $f_{c3}$ and $f_{c4}$, respectively. From the view of CM suppression, both $f_{d3}$ and $f_{d4}$ are not the suitable resonances to form the DM passbands. So, the former two DM resonances (indicated by $f_{d1}$ and $f_{d2}$), generated by the even-mode circuit of DM bisection, are used to constitute the dual DM passbands.

Based on the basic TL theory, the input admittance of the even-mode circuit of DM bisection, $Y_{d\text{-}in}$, can be derived as

$$Y_{d-in} = Y_1 \frac{Y_{L1} + jY_1 \tan\theta_1}{Y_1 + jY_{L1} \tan\theta_1} \tag{4.7}$$

where

$$Y_{L1} = Y_2 \frac{Y_{L2} + jY_2 \tan\theta_2}{Y_2 + jY_{L2} \tan\theta_2} \tag{4.8}$$

where

$$Y_{L2} = jY_s \tan\theta_s - jY_3 \cot\theta_3. \tag{4.9}$$

From the resonant condition of $Y_{d\text{-}in} = 0$, the DM resonant frequencies can be deduced as follows:

$$Y_2(Y_1 \tan\theta_1 + Y_2 \tan\theta_2) + (Y_2 - Y_1 \tan\theta_1 \tan\theta_2) \times (Y_s \tan\theta_s - Y_3 \cot\theta_3) = 0 \tag{4.10}$$

For simplification, let $Y_1 = 2Y_2 = 2Y_3 = Y_s$ and $\theta_3 = \theta_s$. Thus, (3) can be reformulated as

$$(2\tan\theta_1 + \tan\theta_2) + (1 - 2\tan\theta_1 \tan\theta_2) \times (2\tan\theta_3 - \cot\theta_3) = 0 \tag{4.11}$$
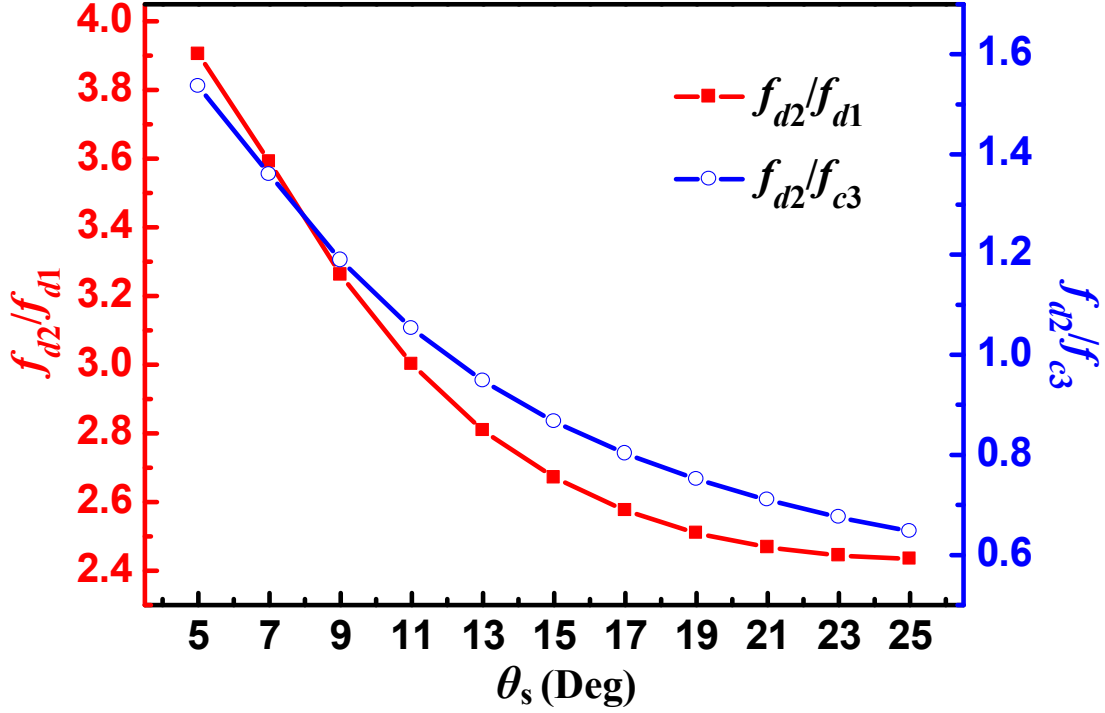
Fig. 4.24. Variations of the frequency ratios ($f_{d2}/f_{d1}$ and $f_{d2}/f_{c3}$) of DM resonances versus $\theta_s$ with $\theta_1 = 28°$, $\theta_2 = 23°$, $Y_1 = 2Y_2 = 2Y_3 = Y_s$, and $\theta_3 = \theta_s$.

Thus, $f_{d3}$ and $f_{d4}$ are the first two solutions of (4.11) and determined by the electric lengths $\theta_1$, $\theta_2$, and $\theta_3$.

Similarly, the resonant condition of two CM resonances ($f_{c1}$ and $f_{c2}$) can be obtained as

$$(2\tan\theta_1 + \tan\theta_2) + 3\tan\theta_3 \times (1 - 2\tan\theta_1\tan\theta_2) = 0 \qquad (4.12)$$

Because $\theta_3 = \theta_s$, the even-mode circuit of CM bisection will behaves as a classical center-stub-loaded resonator when we assume $Y_s = Y_3$. At this time, $f_{c2}$ is equal to $f_{c4}$. Moreover, when we continue assume $\theta_s$ to be a very small electric length, the even-mode circuits of DM and CM bisection can be treated as a quarter-wavelength resonator and a half-wavelength resonator, respectively, leading to the frequency relationship of $f_{d1} \approx 1/2f_{c1} \approx 1/3f_{d2} \approx 1/4f_{c2}$. So, the open-circuited stub ($Y_s$, $\theta_s$) has the ability to adjust the ratio of these four resonances but can not change the size of them.

From the solutions of the equations for the CM resonances and DM resonances discussed above, it is found that the DM resonance $f_{d2}$ and the CM resonance $f_{c3}$ may happen to occur most closely. The variation of frequency ratio ($f_{d2}/f_{c3}$) versus $\theta_s$ with $\theta_1 = 28°$ and $\theta_2 = 23°$, when $Y_1 = 2Y_2 = 2Y_3 = Y_s$ and $\theta_3 = \theta_s$ is illustrated as the open circle dotted blue line in Fig. 4.24. All electrical lengths are given at $f_0 = 1.9$ GHz, which is the midband frequency of the
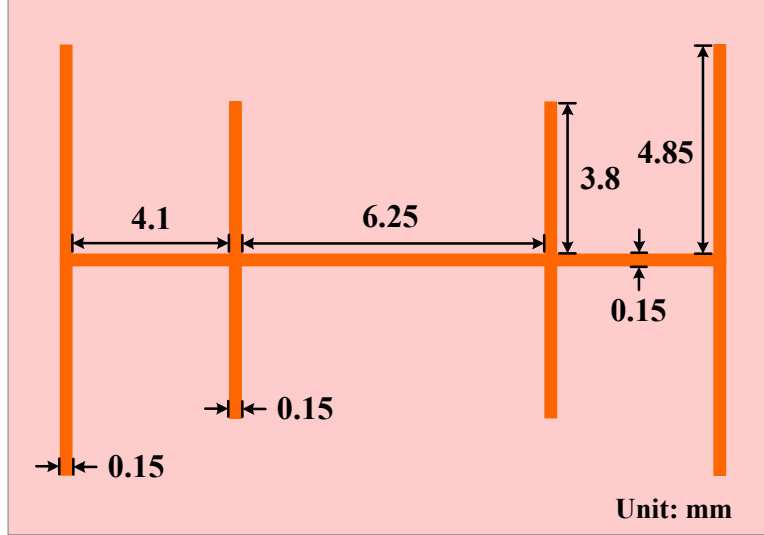
Fig. 4.25. Unit Configuration of the proposed multimode SSLR..

lower passband of the dual-band BPF to be designed.

It is clear to see from Fig. 4.24 that $f_{d2}/f_{c3}$ is equal to 1 when $\theta_s$ is chosen to be 12°. This means that $f_{c3}$ will be shifted to $f_{d2}$ when $\theta_s$ approaches to 12°, and in our design, $\theta_s$ should be chosen a value far from 12°. Besides, it is know from (4.11) that $\theta_s$ has influence on the two desired DM resonant frequencies, $f_{d1}$ and $f_{d2}$. So, the variation of frequency ratio ($f_{d2}/f_{d1}$) versus $\theta_s$ is plotted as the solid square dotted red line in Fig. 4.24. It is seen that $f_{d2}/f_{d1}$ decrease monotonously as $\theta_s$ increases.

### 4.3.2 Eighth-Order Dual-Band HTS Differential Filter Design

In this part, the proposed multimode SSLR is employed to constitute a eighth-order dual-band HTS differential BPF with two passbands operating at 1.9 GHz and 4.9 GHz, respectively. Below are detailed descriptions on the design of the resonator, the internal coupling between two adjacent resonators, the external coupling between the resonator and the feed line, as well as discussions on the CM suppression.

#### 4.3.2.1 Design of the Resonator

As a result of the investigation in Section 4.3.1, mode $f_{d1}$ and $f_{d2}$ are chosen to form the two passbands of the dual-band differential BPF. So, at first, we need to design the multimode SSLR with its mode $f_{d1}$ and $f_{d2}$ resonating at 1.9 GHz and 4.9 GHz, respectively. So, the frequency ratio of two desired DM resonances is obtained as: $f_{d2} / f_{d1} = 4.9 / 1.9 \approx 2.58$. From Fig. 4.24, we found that $f_{d2} / f_{d1}$ is equal to 2.58 when $\theta_s$ is set to be 17°. Incidentally, $f_{d2} / f_{c3}$ is fortunately found at about 0.8, away from 1 and it meets the requirement of CM suppression,
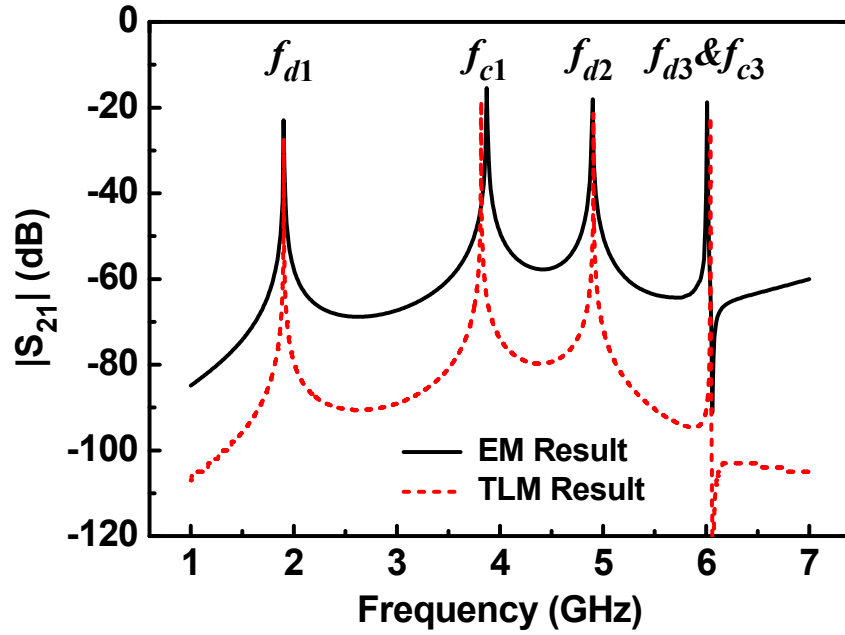
Fig. 4.26. EM and TLM simulated results of the SSLR under weak excitation.

when $\theta_s$ equals to 17°.

Fig. 4.25 presents the configuration of the SSLR obtained with the initial values of $\theta_1 = 28°$, $\theta_1 = 23°$, $\theta_3 = \theta_s = 17°$, $Y_1 = 2Y_2 = 2Y_3 = Y_s = 0.013$ S. The optimized geometrical dimensions of the corresponding TL section are indicated in the figure. Its frequency response under weak coupling by electromagnetic software *Sonnet em* is plotted as the black solid line in Fig. 4.26. For comparison, the simulated result of the SSLR TLM by ADS simulator under weak excitation is portrayed the red dashed-line in Fig. 4.26. Good agreement is observed to verify the validity of the designed resonator.

To miniature the circuit size of the proposed resonator, four open-circuited stubs are folded inner and a new configuration of the resonator is depicted in Fig 4.27(a). After optimized design by *Sonnet em*, the dimensions noted in Fig. 4.27(a) are obtained as follows: $L_1 = 4.1$, $L_2 = 6.3$, $L_3 = 1.05$, $L_4 = 3.7$, $L_5 = 0.7$, $L_6 = 1.05$, $L_7 = 2.45$ (unit: mm). Under DM excitation of this resonator, the DM frequency response are obtained and drawn in Fig. 4.27(b). It is observed that two desired DM resonances, $f_{d1}$ and $f_{d2}$, operating at 1.9 GHz and 4.9 GHz are got, which meet the design specifications well.

### 4.3.2.2 Design of the Internal Coupling Between Two SSLRs

After the above comprehensive study on the multimode SSLR, an eighth-order dual-band differential BPF will be designed. The two DM passbands having Chebyshev response with
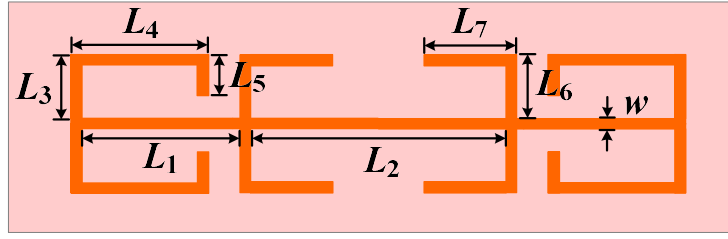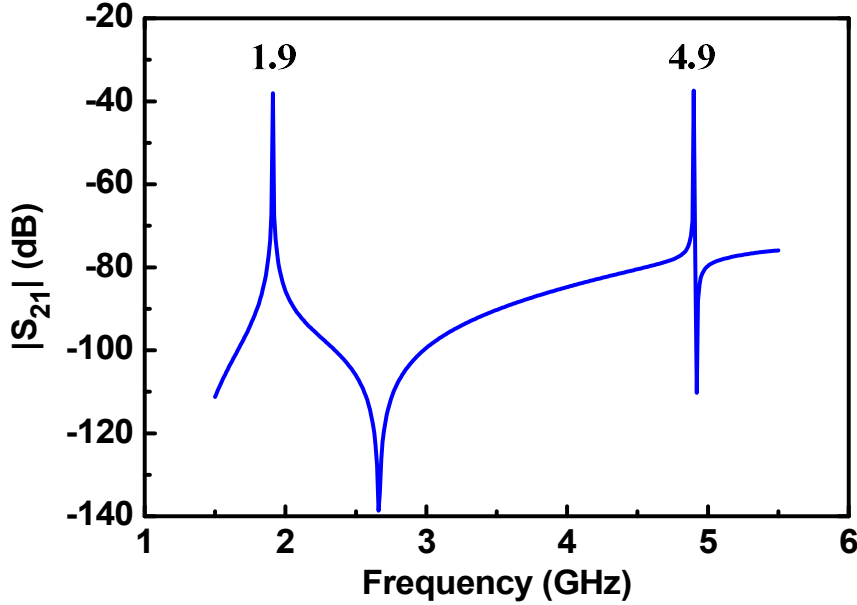
Fig. 4.27. (a) Unit configuration of the compact folded SSLR. (b) Frequency response of $S_{21}$ magnitude under DM weak excitation.

0.04321-dB ripple level are specified at 1.9 GHz and 4.9 GHz, with corresponding fractional bandwidth (FBW) of 3.16% and 4.08%, respectively. The microstrip configuration of the filter is shown in Fig. 4.28. There are two coupling paths in the figure, corresponding to the two passbands, Band I and Band II, of the dual-band BPF. From the above design specifications and the well-known design method of direct coupled resonator filters [28], the required coupling parameters are: the coupling coefficients $M_{12}^{I} = M_{78}^{I} = 0.026$, $M_{23}^{I} = M_{67}^{I} = 0.0187$, $M_{34}^{I} = M_{56}^{I} = 0.0175$, $M_{45}^{I} = 0.0173$, $M_{12}^{II} = M_{78}^{II} = 0.0336$, $M_{23}^{II} = M_{67}^{II} = 0.0241$, $M_{34}^{II} = M_{56}^{II} = 0.0226$, $M_{45}^{II} = 0.0223$, the external quality factors $Q_{ex}^{I} = 32.2$ and $Q_{ex}^{II} = 24.9$, where the superscript I and II indicate the first and second passband, respectively. Below we will describe in sequence the design of the internal coupling space between two SSLRs and the resonator feeding structure by using *Sonnet em*, in order to realize the wanted coupling
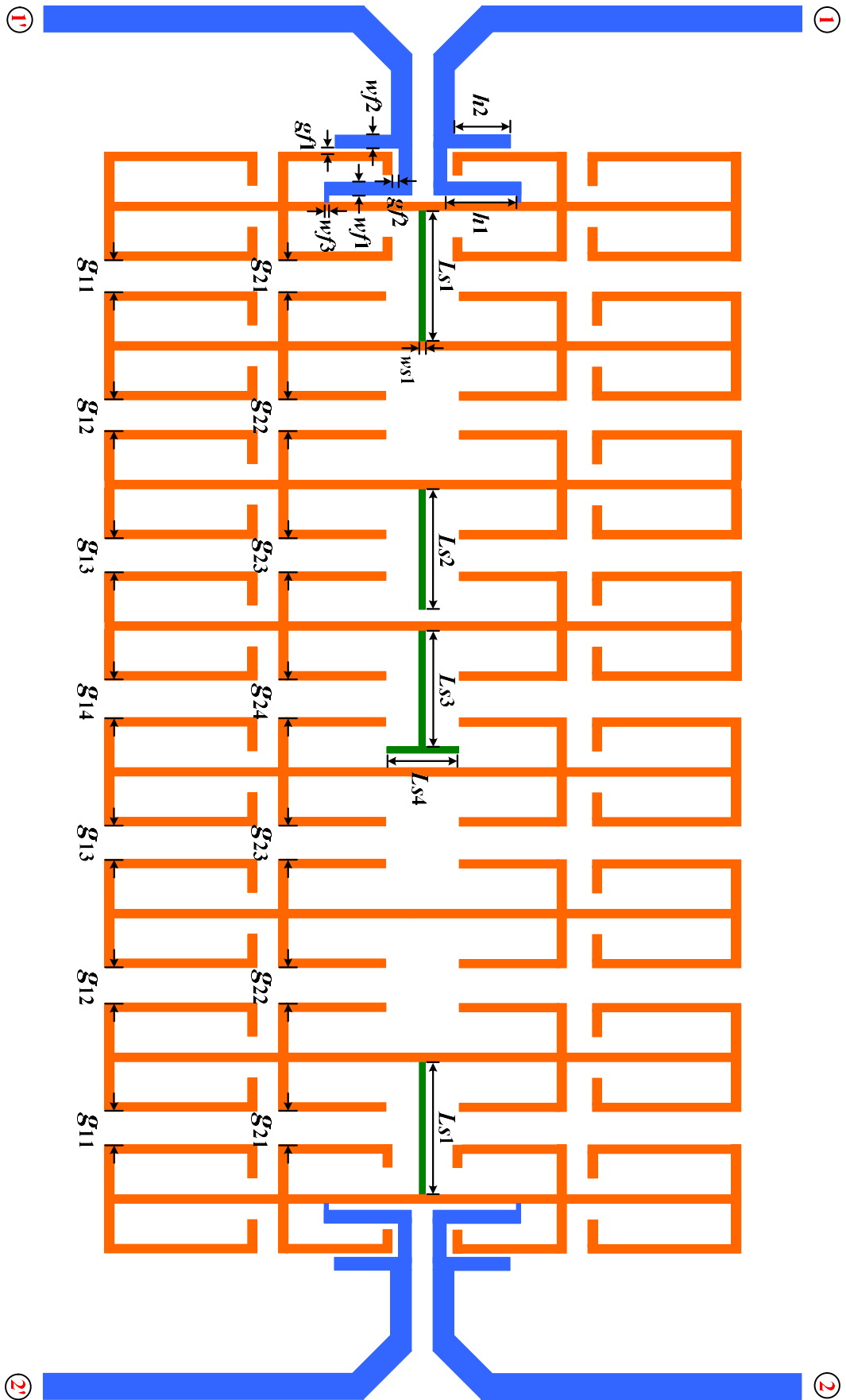
Fig. 4.28.   Layout of the designed eighth-order dual-band HTS differential filter.
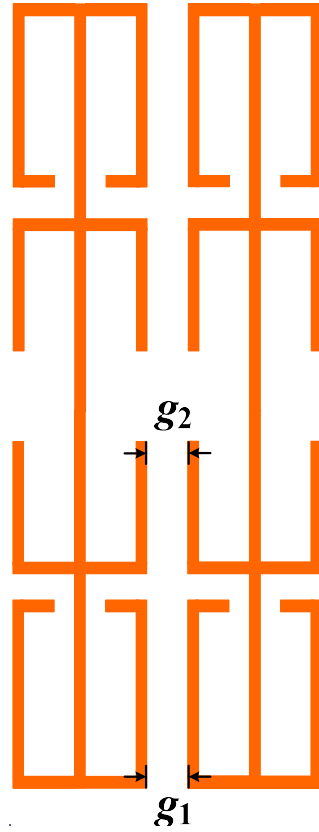
Fig. 4.29.   Configuration of two coupled SSLRs.
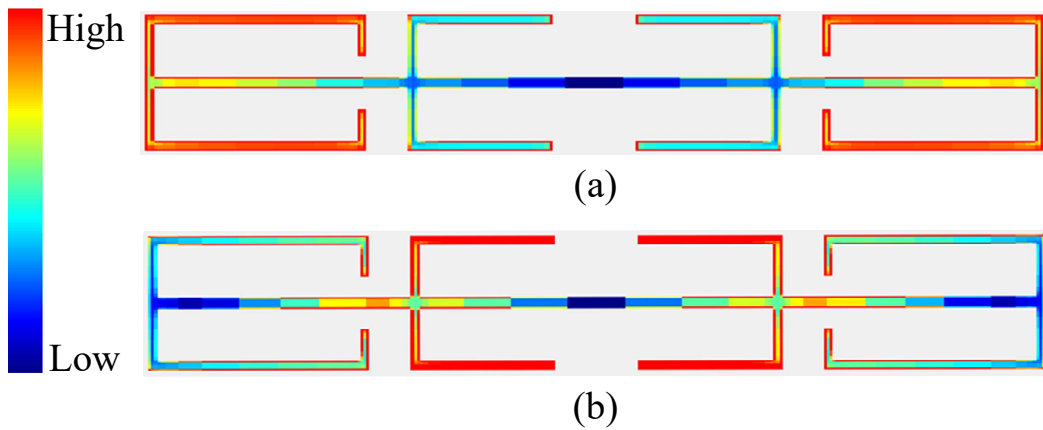


Fig. 4.30.   Simulated electric-field density distributions of the resonator at resonance of (a) $f_{d1}$ = 1.9 GHz and (b) $f_{d2}$ = 4.9 GHz.

coefficients and external $Q$ values.

Fig. 4.29 shows the coupling structure of two adjacent SSLRs, in which $g_1$ is the space between the stubs at two sides, and $g_2$ is the space between the stubs in the middle, and they are both used to adjust the coupling strength between two resonators. Fig. 4.30 exhibits the distribution of electric-field density of the proposed SSLR at two DM resonant frequencies. It is shown that at $f_{d1}$, the electric-field is mainly concentrated on the folded open stubs at the
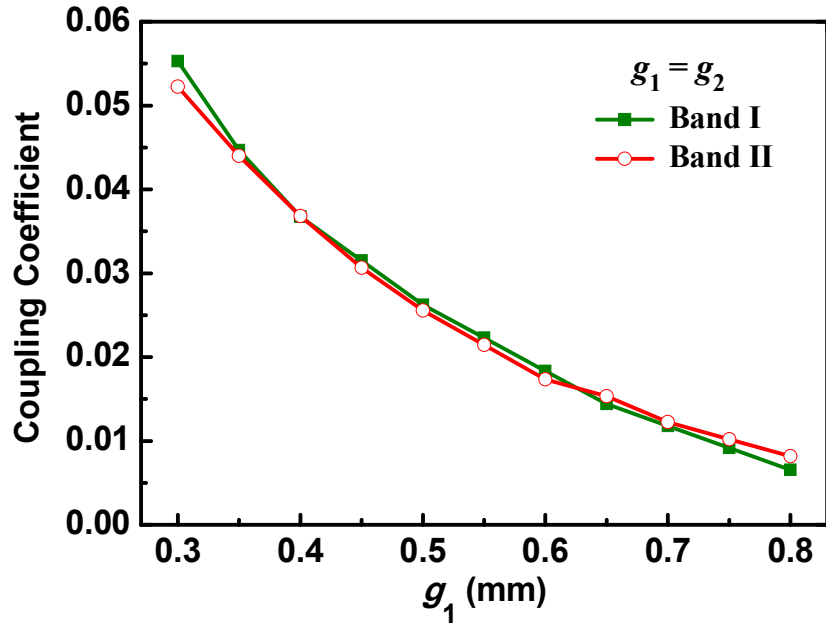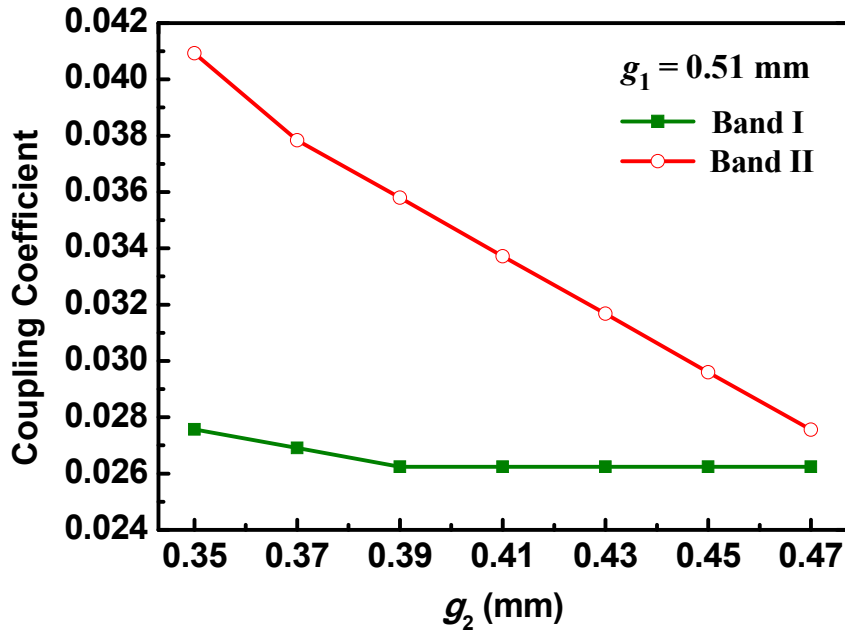
Fig. 4.31.   Simulated coupling coefficients as a function of (a) the coupling space $g_1$ (= $g_2$) and (b) the coupling space $g_2$ when $g_1 = 0.51$ mm under weak DM excitation.

two sides of the resonator, whereas at $f_{d2}$, strong field distributions are observed at both the stubs at two sides and the stubs in the middle. The field distributions in Fig. 4.30 (a) and (b) for mode $f_{d1}$ and $f_{d2}$ suggest that the space $g_1$ between the stubs at two sides will have influence on both mode $f_{d1}$ and $f_{d2}$, while and the space $g_2$ between the stubs in the middle will have influence on mode $f_{d2}$ (Band II) but little influence on mode $f_{d1}$ (Band I). So, we can determine $g_1 = g_2$ at first to meet the coupling strength of Band I, and then vary $g_2$ to satisfy the coupling strength

95

of Band II. It should be clarified that the variation of $g_2$ attributes to the change of $L_6$ (indicated in Fig. 4.27(a)), which leads to the inevitable shift of DM resonant frequencies. So, the associated physical parameter $L_7$ shown in Fig. 4.27(a) would be adjusted to compensate the offset of the DM resonant frequencies.

Fig. 4.31(a) provides the computed variation of coupling coefficients versus the coupling space $g_1 = g_2$. It is seen that the coupling coefficients of both DM passbands decrease monotonously as $g_1 = g_2$ increases. From this figure, the space $g_{11}$, $g_{12}$, $g_{13}$, and $g_{14}$ shown in Fig. 4.28 are quickly obtained as 0.51 mm, 0.59 mm, 0.61 mm, and 0.61 mm, respectively,   to obtain the required coupling coefficients for Band I performance.

Fig. 4.31(b) shows the simulated coupling coefficients curves of Band I and Band II versus the space $g_2$ when $g_1 = 0.51$ mm. It is seen that the coupling coefficient of Band I varies little, while that of Band II decreases quickly. From the curves, the space $g_{21}$ indicated in Fig. 4.28 can be chosen as 0.4 mm to realize the required $M_{12}^{II} = M_{78}^{II} = 0.0336$ for Band II performance. In the same way, the space $g_{23}$, $g_{34}$, and $g_{45}$ can be determined to be 0.52 mm, 0.53 mm, and 0.53 mm, respectively.

### 4.3.2.3 Design of the External Coupling Structure

The following is to design the external coupling structure to meet the desired $Q_{ex}$ values of two passbands simultaneously. As shown in Fig. 4.32, the dual-feeding external coupling structure, which includes a tap feeding counterpart and a coupled-line feeding counterpart, is employed as the feeding structure in this design to provide enough design flexibility. In the following design, as shown in Fig. 4.32, the line widths $w_{f1}$ and $w_{f2}$ of the tapped-line and $w_{f3}$ of the coupled-line arm and the coupling gap $g_{f1}$ and $g_{f2}$ are fixed as 0.2 mm, 0.1 mm, 0.25 mm, 0.1 mm, and 0.25 mm, respectively. $h_1$ and $h_2$ represent the tapped position the coupled-line length, respectively. Fig. 4.33(a) and (b) illustrate the design graph of $Q_{ex}$ for the dual-band BPF as a function of $h_1$ and $h_2$, respectively, where the superscript I and II of $Q_{ex}$ denote the first and second passband, respectively. It is observed from Fig. 4.33(a) that though $Q_{ex}^{I}$ decreases slightly, the $Q_{ex}$ values of both DM passbands decrease monotonously as $h_1$ increases. But from Fig. 4.33(a), it shows that $Q_{ex}^{II}$ increases largely as $h_2$ enlarged with the fixed $h_1$ while $Q_{ex}^{I}$ remains a constant. So, we can determine $h_1$ at first to meet the feeding strength of Band I, and then tune $h_2$ to satisfy the feeding strength of Band II.
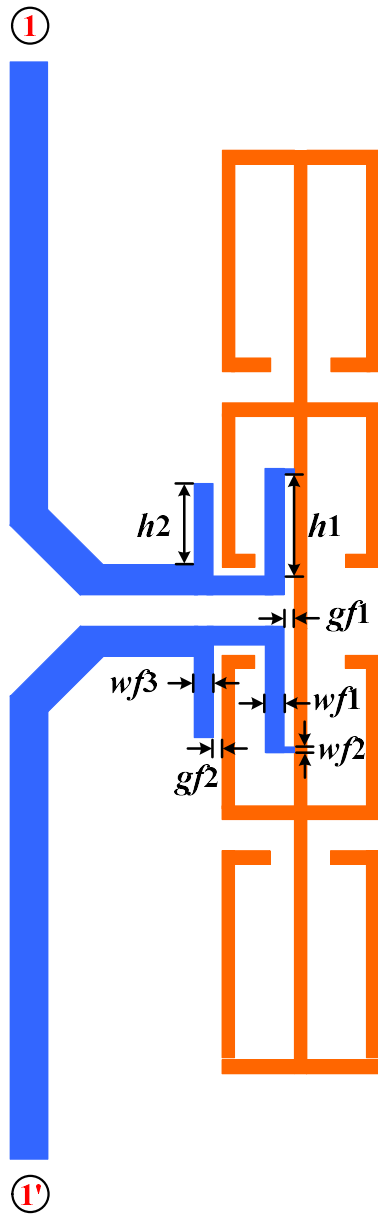
Fig. 4.32.　Dual-feeding structure of the proposed SSLR.

### 4.3.2.4 Wideband CM Suppression

As discussed in Section 4.2, the unwanted CM resonances will inevitable transmitted from the input to output by the formed coupling paths, resulting in thereby the poor CM suppression. Fortunately, the frequency discrepancy technique has the ability to separate the CM resonances in adjacent resonators and therefore block the transmission of CM signals.

As shown in Fig. 4.28, multiple stubs are loaded at the central symmetrical parts of the SSLRs. To enlarge the frequency discrepancy of two adjacent CMs, the first and second SSLRs as well as the seventh and eighth SSLRs are centrally connected by a narrow microstrip line. The third SSLR is loaded with a open-circuited subs. The fourth SSLR is
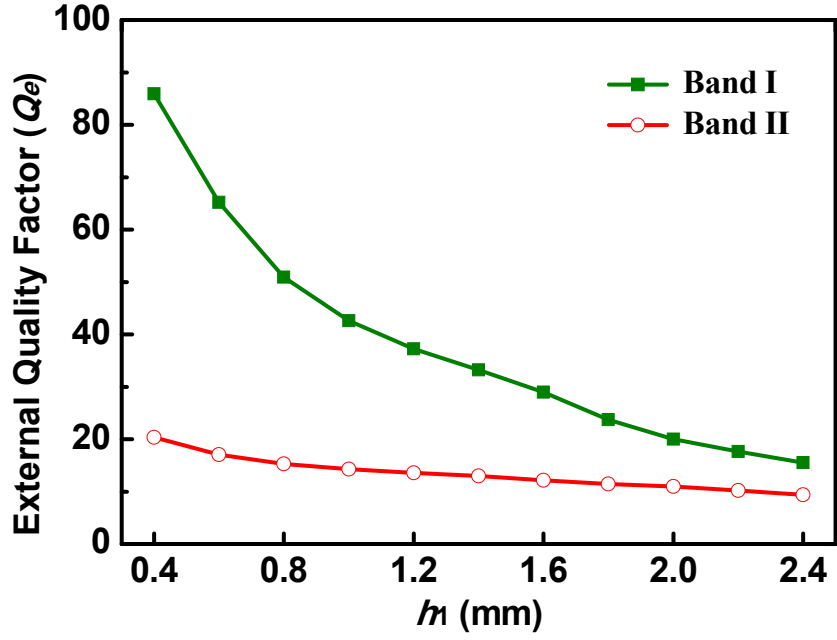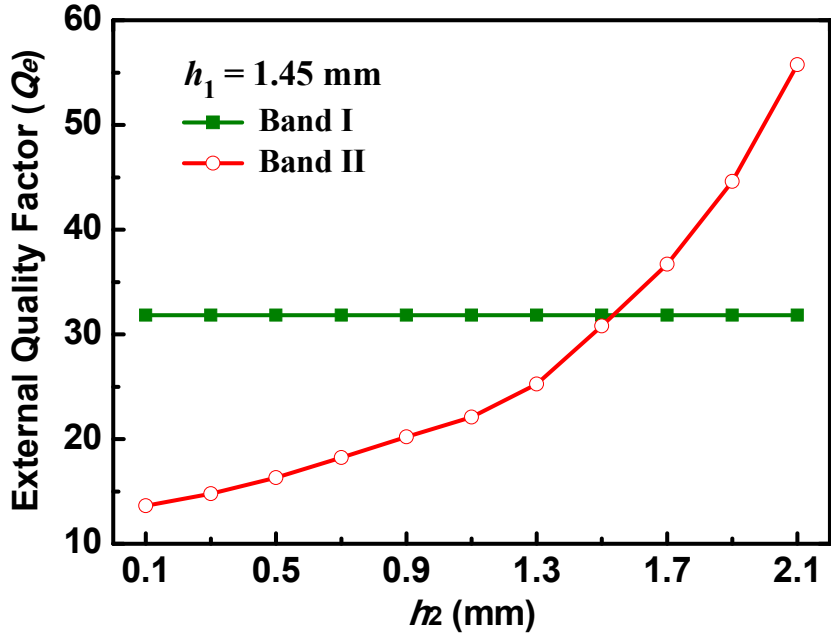
Fig. 4.33.  Simulated external quality factors of the two DM passbands with (a) different tapped position $h_1$ when $h_2 = 0$ and (b) coupled-line length $h_2$ when $h_1 = 1.45$ mm.

loaded with the T-shaped stub. Thus, the CM resonant frequencies of the most of adjacent SSLRs are made different, weakening the coupling strength among CM resonances. Then, the CM transmission is expected to reduce. After optimized by the EM simulator *Sonnet em*, the parameters of the loaded stubs specified in Fig. 4.28 are obtained as follow: $L_{s1} = 2.6$, $L_{s2} = 2.35$, $L_{s3} = 2.2$, $L_{s4} = 0.9$, and $w_{s1} = 0.1$ (unit: mm).
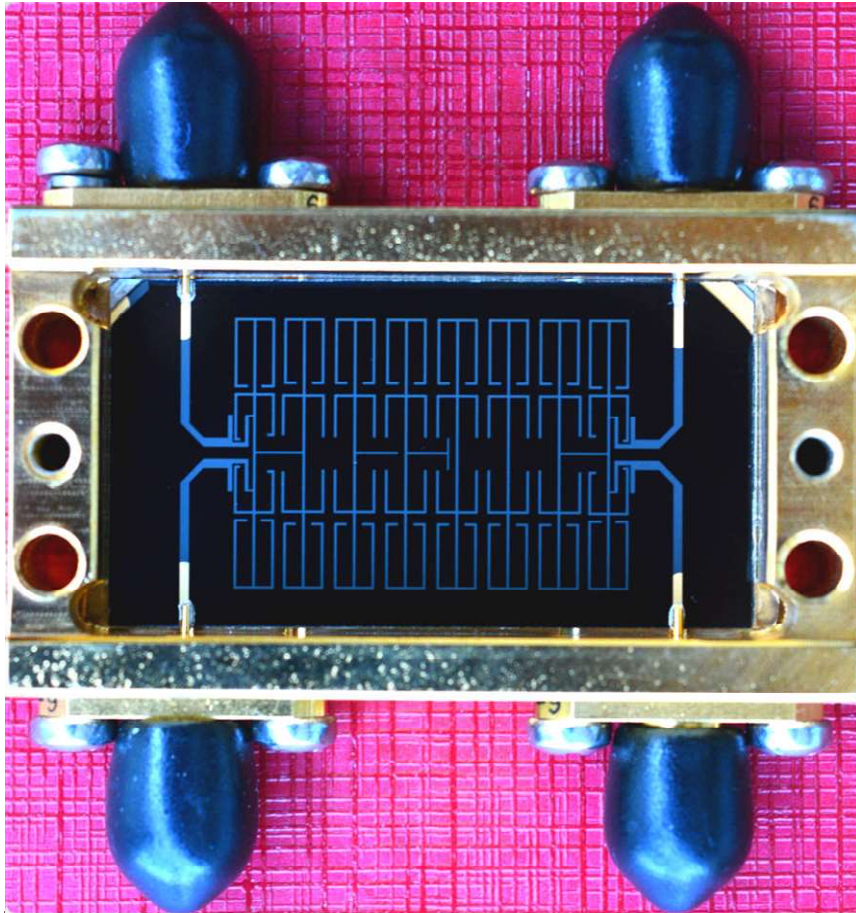
Fig. 4.34.　Photograph of the fabricated HTS differential BPF with cover opened.

### 4.3.3 Experimental Results and Discussion

To verify the above design and the performance of the eighth-order differential BPF, the circuit shown in Fig. 4.28 is fabricated on a 0.5-mm-thick MgO wafer with double-sided YBCO films. The ion etching technology is used to etch the front-side film to form the circuit structure, and the circuit is mounted on a gold-plated metal carrier and then carefully packaged into a shield box. The photograph of the fabricated HTS BPF with cover opened is shown in Fig. 4.34. The fabricated filter, with the feeding lines excluded, occupies $28.03 \times 19.5$ mm$^2$, about $0.45\,\lambda_g \times$ $0.31\,\lambda_g$, where $\lambda_g$ is the guide wavelength on the used substrate at 1.9 GHz.

The packaged dual-band differential BPF is cooled down to a temperature of 77 K in a cryogenic cooler and measured by a four-port vector network analyzer, Agilent E5071C. The simulated and measured results are drawn in Fig. 4.35, which agree well with each other. For the DM response, the measured first and second passbands are centered at 1.905 and 4.905 GHz, respectively, with corresponding 3-dB passbands covering 1.87 - 1.94 GHz and 4.807 -
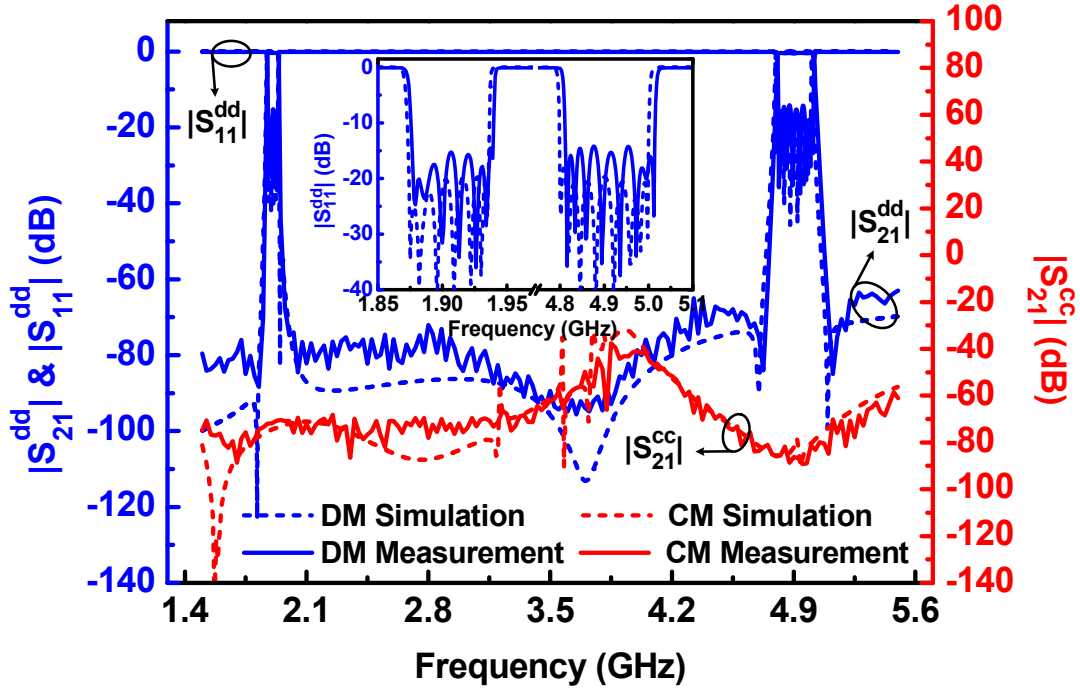
Fig. 4.35.   Simulated and measured results.

5.017 GHz, respectively. The maximum in-band insertion loss is approximately 0.3 dB and 0.35 dB, respectively, showing the low-loss superiority of the HTS technology. The measured return loss is better than 15 dB in both passbands. For the CM response, the measured minimum CM insertion loss is 70 dB in the first passband and 78 dB in the second passband, which show a good CM suppression level within DM passbands. Besides, from DC to 5.5 GHz, the CM suppression is better than 31 dB. Some slight deviation between the measurement and simulation is mainly due to the possible differences between the nominal and real values of the dielectric constant and substrate thickness.

In addition, benefiting from the created four transmission zeros and high-order design, high selectivity of two passbands are obtained. The roll-off rate $\zeta_{ROR}$ can be expressed as

$$\zeta_{ROR} = \frac{\left| \delta_{-20\,dB} - \delta_{-3\,dB} \right|}{\left| f_{-20\,dB} - f_{-3\,dB} \right|} \tag{4.13}$$

where $\delta_{-20}$ dB and $\delta_{-3}$ dB is the 20-dB and 3-dB attenuation point, respectively, $f_{-20}$ dB and $f_{-3}$ dB is the 20-dB and 3-dB stopband frequency, respectively. The calculated $\zeta_{ROR}$ in upper side and low side of two passbands are 2833, 5666, 1307, and 1307, respectively.

## 4.4 Conclusion

Two high-order dual-band HTS differential BPFs are developed based on the proposed multimode resonators in this chapter. The operating mechanism of the DM and CM circuits of the proposed resonators are well-studied by the even-/odd-mode method. Due to the unique property of proposed resonators and adding some adjustable elements, independent control of both the midband frequencies and the bandwidths of the dual-band BPFs are achieved. With a combined use of the appropriately selected feeding structure and the frequency discrepancy technique, a favorable CM suppression over a wide frequency range is obtained. Detailed design process is described. Benefiting from the HTS technology, the fabricated filters have ultra-low in-band insertion losses and high selectivity. With these features, the proposed filters are attractive for applications in multiband communication systems requiring high-sensitivity and high anti-interference properties.

The work described in Section 4.2 have been published in the IEEE Transactions on Microwave and Techniques, and the part of design work in Section 4.3 have been published in the Proceedings of 2018 Asia-Pacific Microwave Conference (APMC 2018).

# Chapter 5
## Compact Diplexer Using Hybrid Resonant Structure

### 5.1 Overview

From the discussion in chapter 1, it is known that diplexer is one type of essential components in RF front-end transceivers and much attention has been paid to design diplexers with merits of compact size and high port isolation. For example, a high isolation diplexer is realized by connecting two individual BPFs with an optimized T-junction [55], but circuit size is large. To achieve a compact design, multimode resonators [57]-[59], common resonator replaced the matching circuit [55] and an asymmetric transmission zeros (Tzs) technique [60] are utilized to constitute the diplexer with the desired port isolation. However, these designs are implemented by the microstrip line structures.

Recently, to make full use of the limited space in integrated circuit board, slotlines or defected ground structures etched on the ground plane are popular used in designing microwave circuits with compact size [86]-[89]. For example, the miniaturized dual-band BPFs were constituted by combining the slotline and microstrip resonators [86]-[88], or adopting the purely two sets of coupled slotline resonators [89]. In addition, by adding an additional matching network, such as the T-junction, several compact diplexers were constructed by the slotline structures. However, most of the used slotline resonators behave the property of single mode.

In this chapter, a slotline stub-loaded dual-mode resonator (SSLDR) as well as a microstrip stub-loaded dual-mode resonator (MSLDR) are proposed and discussed firstly. The proposed MSLDR and SSLDR provide two independent paths for signal transmission without extra combination circuits. By using these two signal paths, a compact and high selectivity dual-band BPF with two controllable passbands is designed for demonstration at first. Then the proposed BPF is further modified to design a compact diplexer with an isolation larger than 28 dB. The simulation and measurement are conducted and the results agree well with each other, which verify the proposed structure and design method.
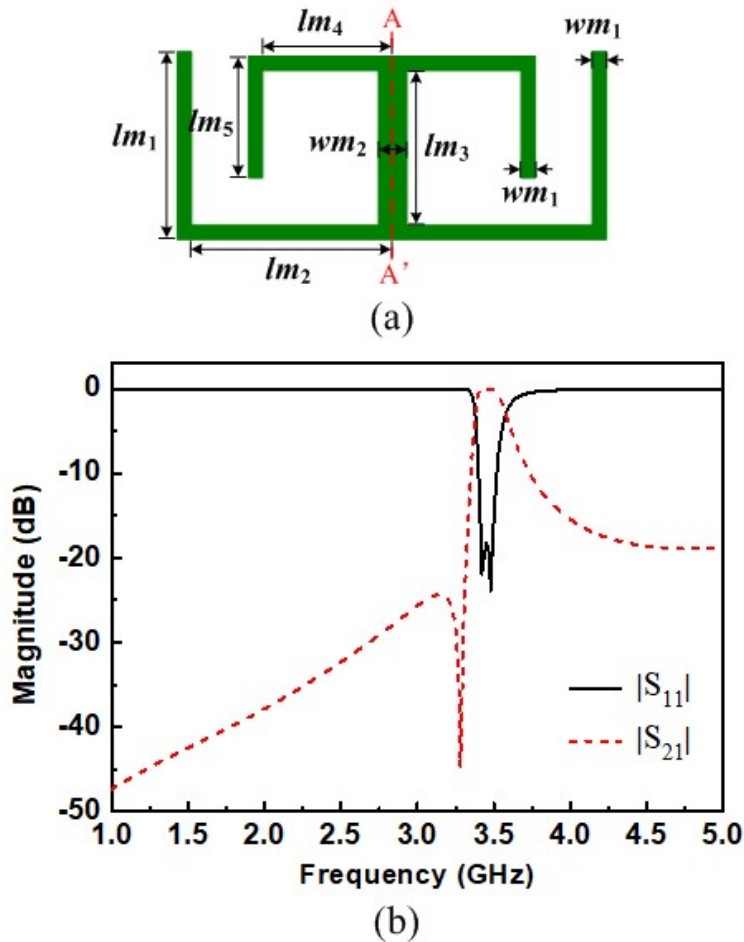
Fig. 5.1 (a) Schematic structure of the MSLDR and its (b) Simulated frequency response under tight coupling.

## 5.2 Diplexer Using MSLDR and SSLDR

### 5.2.1 Analysis of MSLDR

Fig. 5.1(a) shows the schematic of the MSLDR, which consists of a folded half-wavelength resonator and a center loaded T-shaped stub. The line lengths and widths of microstrip lines are indicated as $l_{mi}$ and $w_{mi}$, $i = 1, 2, 3....$ The typical frequency response of the MSLDR is shown in Fig. 5.12(b). It is seen that the resonator has two resonant modes. Since the MSLDR is a symmetric structure, it can be readily analyzed by using the even- and odd-mode method. In the case of odd-mode excitation, the symmetrical plane (red dashed line AA') is an electrical wall (E.W.), and the circuit is simplified as shown in Fig. 5.2(a). For the even-mode excitation, the symmetrical plane is a magnetic wall (M.W.), and the simplified circuit is given in Fig. 5.2(b). If we assume $w_{m2} = 2w_{m1}$, the odd-mode equivalent circuit of the MSLDR
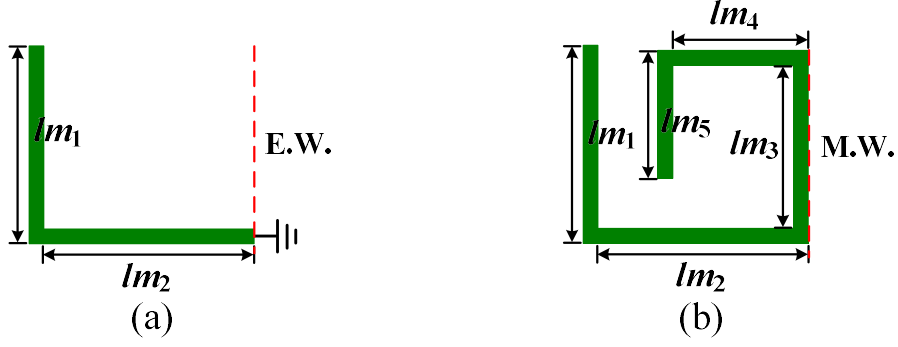
Fig. 5.2 (a) Odd-mode equivalent circuit of the MSLDR,

(b) Even-mode equivalent circuit of the MSLDR.

is a quarter-wavelength uniform-impedance resonator (UIR) and the even-mode equivalent circuit is a half-wavelength UIR. Thus, two resonant frequencies ($f_{om}$, $f_{em}$) of MSLDR can be easily expressed as

$$f_{om} \approx \frac{c}{4\left(l_{m1} + l_{m2}\right)\sqrt{\varepsilon_{effm}}}$$

(5.1)

$$f_{em} \approx \frac{c}{2\left(l_{m1} + l_{m2} + l_{m3} + l_{m4} + l_{m5}\right)\sqrt{\varepsilon_{effm}}}$$

(5.2)

where $c$ is the speed of light in the free space, $\varepsilon_{effm}$ denotes the effective dielectric constant of the microstrip line. From (1) and (2), these two frequencies can be changed easily and separately by varying the lengths of the half-wavelength resonator and the T-stub. In addition, as can be seen from Fig. 5.1(b), the MSLDR has also one transmission zero (TZ) which can be located at the lower or upper side if the two resonant modes by varying the length of the T-stub [90]. The location of the TZ, can be given by

$$f_z \approx \frac{c}{4\left(l_{m3} + l_{m4} + l_{m5}\right)\sqrt{\varepsilon_{eff}}} \, .$$

(5.3)

## 5.2.2 Analysis of SSLDR

Compared with the above MSLDR that is formed on the top plane of the substrate, the proposed SSLDR is etched on the ground plane, as shown in Fig. 5.3(a). $l_{si}$ and $w_{si}$, $i$ = 1, 2,
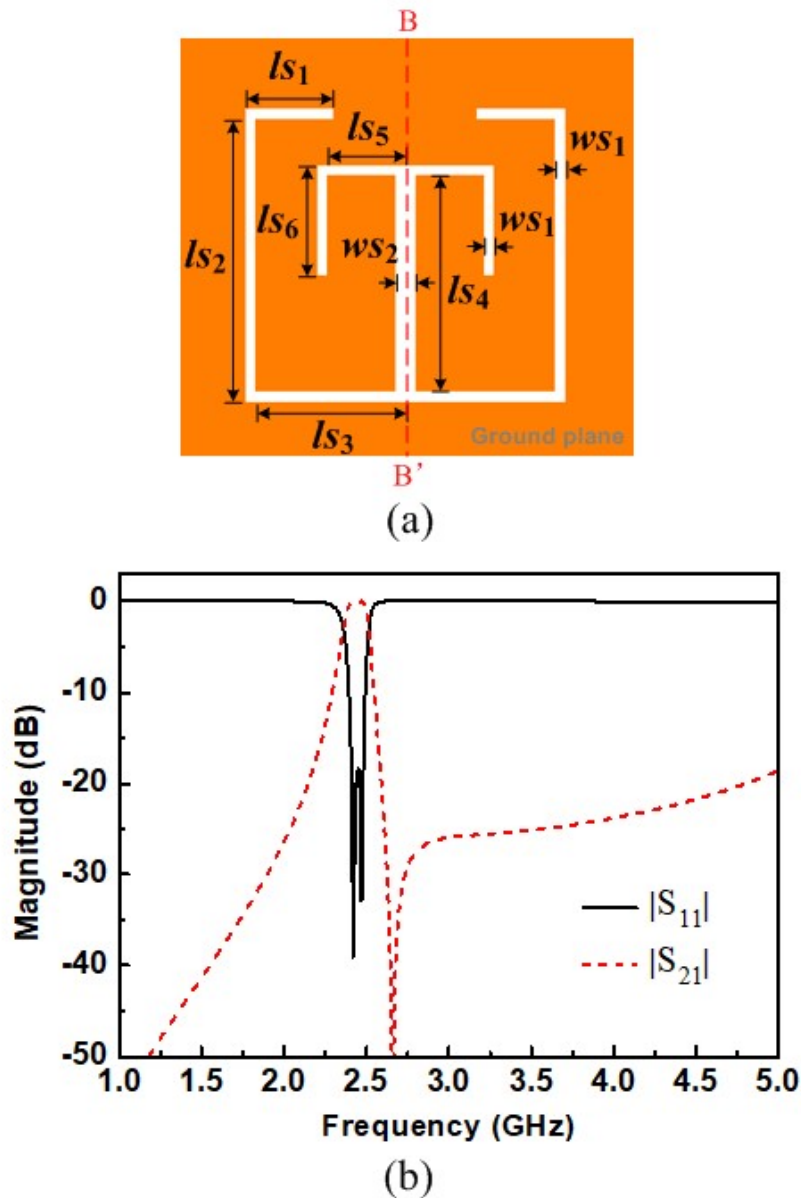
Fig. 5.3 (a) Schematic structure of the SSLDR and its (b) Simulated frequency response of the SSLDR under tight coupling.

3..., denote the line lengths and widths of slotlines, respectively. The typical frequency response of the SSLDR under the lossless condition is shown in Fig. 5.3(b). The configuration of the SSLDR and its operation mechanism are the similar as those of the MSLDR. The resonator has also two resonant modes and one TZ, which can be varied easily and separately by changing the lengths of the slotlines, as descried for the MSLDR. Similarly, the odd-mode and even-mode equivalent circuits of the SSLDR are obtained and respect illustrated in Fig. 5.4(a) and Fig. 5.4(b) after used the even- and odd-mode method. It is interesting found that the loaded slotline stub of the SSLDR is existed in odd-mode equivalent circuit while the
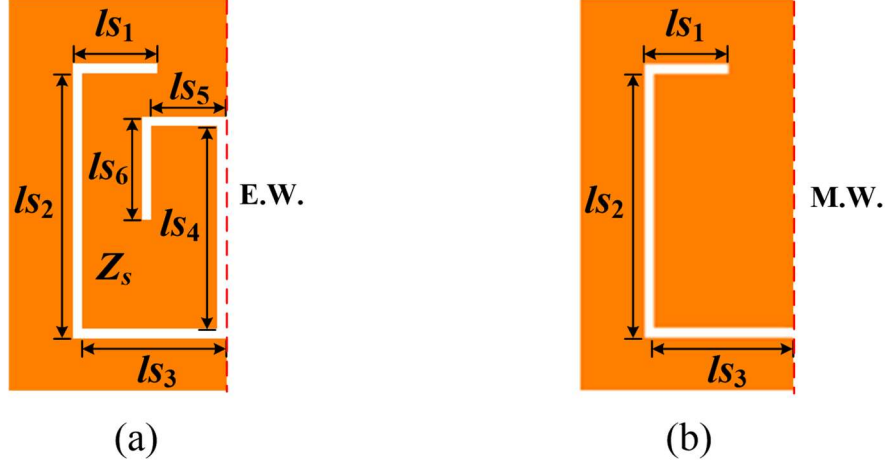
Fig. 5.4 (a) Odd-mode equivalent circuit of the SSLDR, (b) Even-mode equivalent circuit of the SSLDR.

microstrip line stub is owned by the even-mode equivalent circuit of the MSLDR. Two resonances ($f_{os}$, $f_{es}$) of the SSLDR can be estimated as

$$f_{os} \approx \frac{c}{2\left(l_{s1} + l_{s2} + l_{s3} + l_{s4} + l_{s5} + l_{s6}\right)\sqrt{\varepsilon_{effs}}} \qquad (5.4)$$

$$f_{es} \approx \frac{c}{4\left(l_{s1} + l_{s2} + l_{s3}\right)\sqrt{\varepsilon_{effs}}} \qquad (5.5)$$

where $\varepsilon_{effs}$ indicates the effective dielectric constant of the slotline [91].

### 5.2.3 Dual-Band Bandpass Filter Design

For demonstration, a novel compact dual-band BPF is designed by the proposed MSLDR and SSLDR. Fig. 5.5(a) shows the configuration of the proposed dual-band BPF. It consists of two dual-mode resonators and a pair of microstrip T-shaped feed lines. On the top plane of the substrate is the proposed MSLDR, and on the ground plane is the proposed SSLDR. These two resonators provide two signal transmission paths for dual-band frequency response. Based on (5.1), (5.2), (5.4), and (5.5), the center frequencies of two passbands, denoted as $f_{c1}$ and $f_{c2}$, can be determined as

$$f_{c1} = \frac{f_{os} + f_{es}}{2} \qquad (5.6)$$
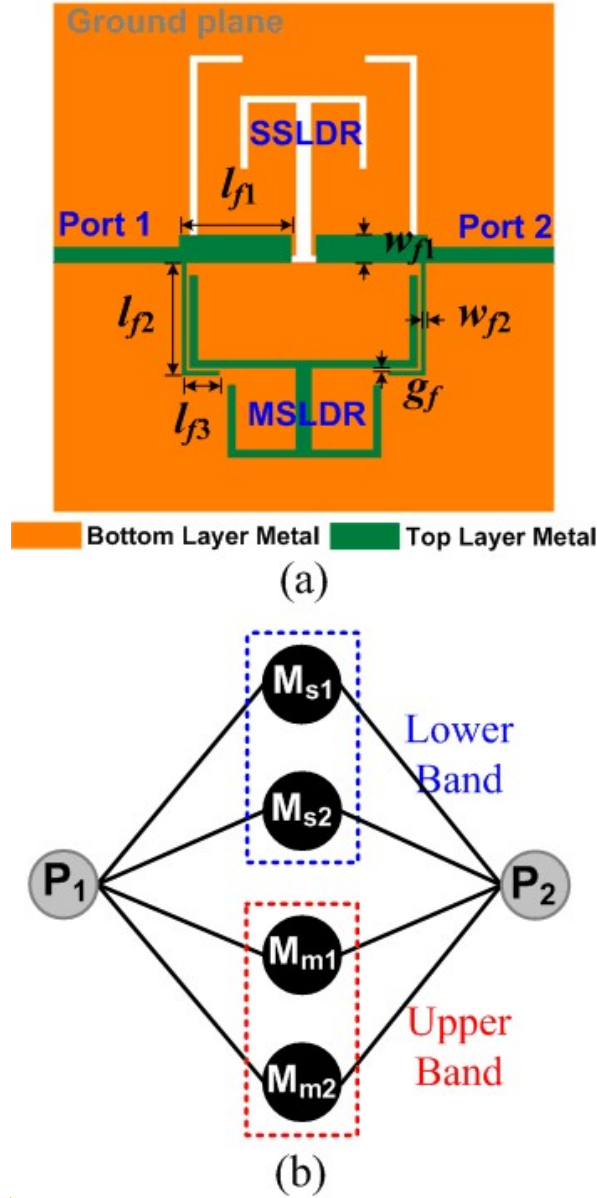
Fig. 5.5 (a) Configuration of the proposed dual-band BPF and (b) its coupling diagram.

$$f_{c2} = \frac{f_{om} + f_{em}}{2}.$$ (5.7)

The signal of the first passband is transmitted to the background SSLDR through the parallel wide microstrip lines of T-shaped feedlines. The signal of the second passband is directly coupled to the MSLDR through the gaps between the parallel narrow microstrip lines. The coupling diagram is depicted in Fig. 5.5(b). The center frequencies and its corresponding fractional bandwidth (FBW) of two passbands are 2.45 GHz (6%) and 3.45 GHz (3%), respectively. A substrate with a relative dielectric constant of 10.2 and a thickness of 0.635 mm is used. To realize the desired passband, the optimized dimensions of the MSLDR as
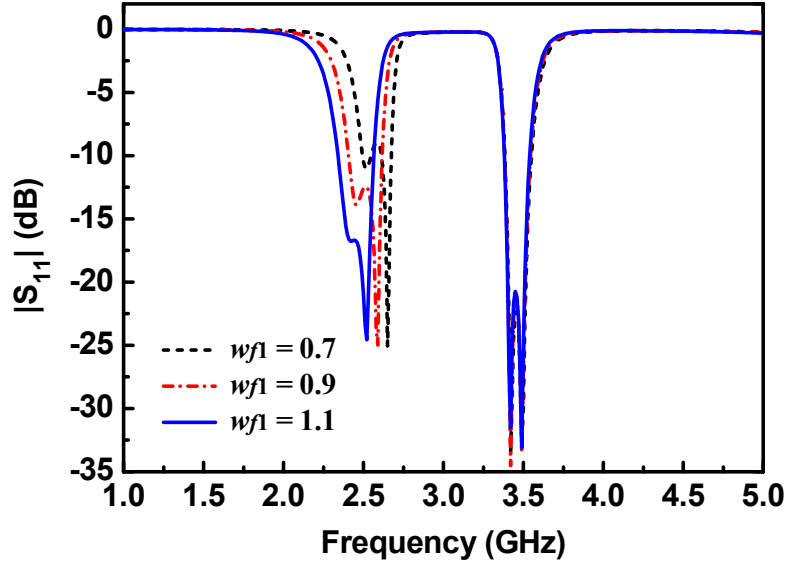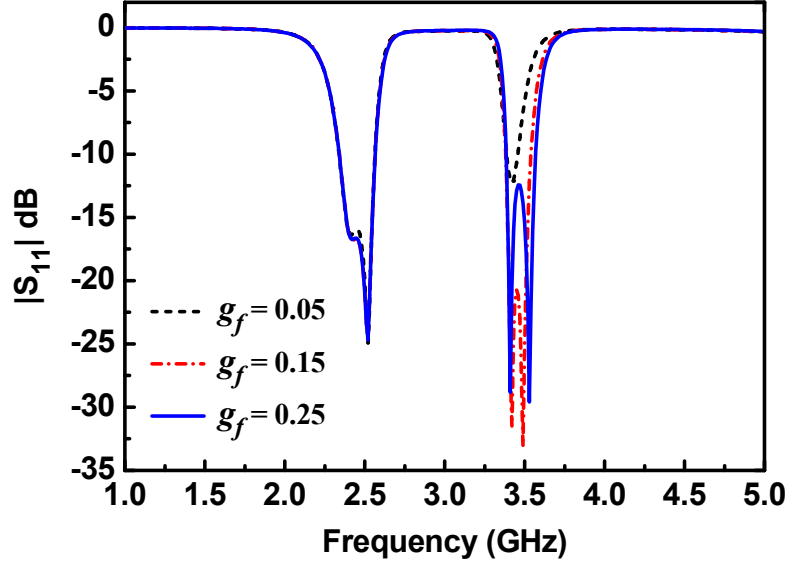
Fig. 5.6　Variation of $|S_{11}|$ of the dual-band BPF with different (a) $w_{f1}$ and

(b) $g_f$ when the other parameters keep unchanged.

indicated in Fig. 5.1(a) and the SSLDR as indicated in Fig. 5.3(a) are: $w_{m1} = 0.3$, $w_{m2} = 0.6$, $l_{m1} = 3.95$, $l_{m2} = 4.2$, $l_{m3} = 3.3$, $l_{m4} = 2.75$, $l_{m5} = 2.65$, $w_{s1} = 0.3$, $w_{s2} = 0.6$, $l_{s1} = 2.5$, $l_{s2} = 8.25$, $l_{s3} = 4.2$, $l_{s4} = 6.05$, $l_{s5} = 2.2$, and $l_{s6} = 3.1$, all in mm. Fig. 5.1(b) and Fig. 5.3(b) show the simulated frequency responses of the designed MSLDR and SSLDR, respectively.

The element values for a Chebyshev prototype with 0.04321 dB ripple are $g_0 = 1$, $g_1 = 0.6648$, $g_2 = 0.5445$, and $g_3 = 1.2210$ [66]. Based on (8), the required external quality factors ($Q_e$) of the first passband and the second passband are determined as $Q_{e1} = 11.1$ and $Q_{e2} = 22.2$.

$$Q_e = \frac{g_0 g_1}{FBW} \cdot \qquad (5.8)$$

In this design, the wide microstrip line with the length $l_{f1}$ and width $w_{f1}$ is adjusted to achieve the desired $Q_{e1}$ for the SSLDR filter (lower passband), while the $Q_{e2}$ for MSLDR filter (upper passband) is realized by using the narrow microstrip line with the length ($l_{f2}+l_{f3}$), width $w_{f2}$ and coupling gap $g_f$. Fig. 5.6 illustrates the variations of $|S_{11}|$ with different $w_{f1}$ and $g_f$ of the feedlines. It is observed from Fig. 5.6(a) that the decreases of $w_{f1}$ will increases the return loss of the lower passband but the second passband remains almost unchanged. While the response of the second passband is influenced by the varied $g_f$, as portrayed in Fig. 5.6(b). So, it is concluded that two passbands of the proposed dual-band BPF constructed by SSLDR and MSLDR can be designed independently. The finally optimized dimensions of the feedlines are: $l_{f1}$ = 4.4, $w_{f1}$ = 1.1, $l_{f2}$ = 4.45, $l_{f3}$ = 1.3, and $w_{f2}$ = $g_f$ = 0.15, all in mm. The design procedure of a dual-band BPF using the proposed SSLDR and MSLDR is summarized as follows.

1) Based on the desired center frequency and bandwidth of the first passband, deducing the physical length $ls_1$ to $ls_6$ of the SSLDR with assumed slotline widths and (5.4)-(5.6).

2) From (5.1), (5.2), and (5.7), determining the physical length $lm_1$ to $lm_5$ of the MSLDR with given microstrip line widths, based on the required center frequency and bandwidth of the second passband.

3) Based on the desired ripple level of the first passband, tuning the length $l_{f1}$ and width $w_{f1}$ of wide microstrip line. Then, tuning the length ($l_{f2}+l_{f3}$), width $w_{f2}$ and coupling gap $g_f$ of narrow microstrip line to satisfy the required ripple level of the second passband.

4) Optimizing the overall filter circuit to obtain the desired performance of the designed dual-band BPF.

The simulation of the dual-band BPF is carried out by using the EM simulator, *Sonnet em*, and the measurement is executed on a network analyzer, Agilent E5071C. Fig. 5.7 gives the simulated and measured frequency responses, which are in good agreements. The simulated passbands are centered at 2.45 GHz and 3.45 GHz, with a 3-dB FBW of 11.3% and 6.3%, respectively. In the measurements, two passbands are centered at 2.44 GHz and 3.48 GHz, with a 3-dB FBW of 11.5% and 6.9%, respectively. The experimental insertion losses (ILs) are 2.11 dB and 2.06 dB, which are mainly attributed to the dielectric loss (loss tangent 0.0022) and radiation loss (no shielding box). Meanwhile, four TZs can be observed, which
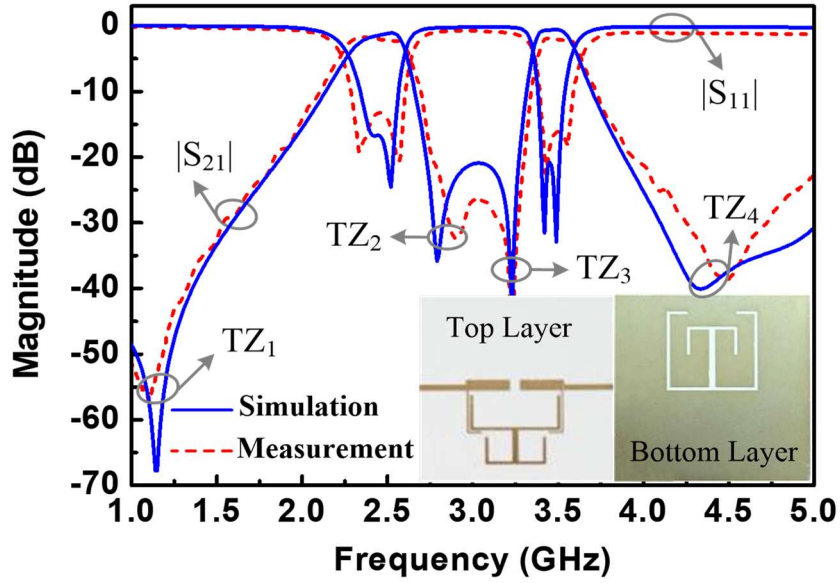
Fig. 5.7    Frequency response of the designed dual-band filter.

Table 5.1 Comparison of other referenced dual-band BPFs

| Ref. | Fre. (GHz) | Res. Type | IL (dB) | TZs | I.C.* | Size ($\lambda_g \times \lambda_g$) |
|------|-----------|-----------|---------|-----|-------|------------------|
| [92] | 2.4 / 5.2 | M* | 1.6 / 1.4 | 4 | Yes | 0.54×0.16 |
| [93] | 2.39 / 5.14 | M | 0.42 / 0.9 | 3 | No | 0.16×0.25 |
| [86] | 1.55 / 2.57 | M & S* | 1.2 / 1.4 | 1 | No | 0.32×0.11 |
| [87] | 2.35 / 3.15 | M & S | 1.8 /3.0 | 2 | Yes | 0.21×0.19 |
| [88] | 1.85 / 2.35 | S | 2 / 2.5 | 2 | No | 0.19×0.20 |
| This work | **2.45 / 3.45** | **M & S** | **2.11 / 2.06** | **4** | **Yes** | **0.14×0.22** |

M*: Microstrip, S*: Slotline, I.C.*: Independent Controllable

increase significantly the stopband rejection and the isolation between the two passbands. Among them, $TZ_2$ and $TZ_3$ are the inherent TZs of the proposed resonators, and $TZ_1$ and $TZ_4$ are produced by the source-load coupling. In addition, the comparison of proposed dual-band filter with referenced works is summarized in Table 5.1. It is seen that the proposed dual-band filter outperforms the others in terms of the selectivity of passbands, independent controllable and the circuit size.
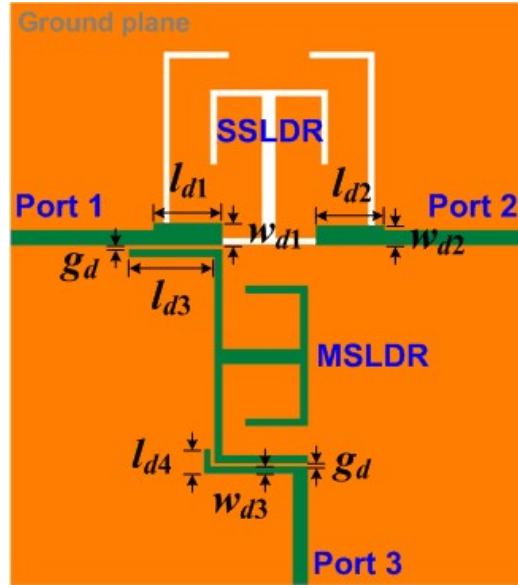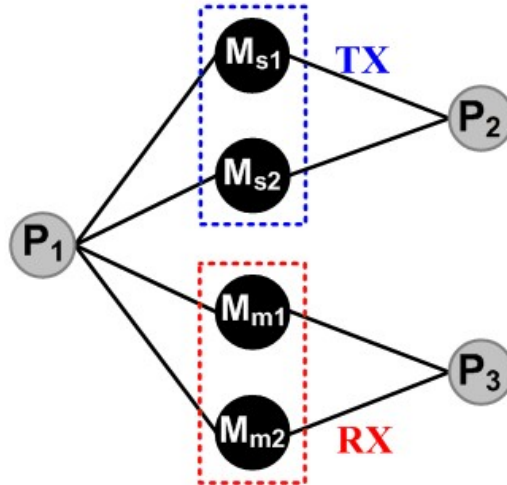
Fig. 5.8 (a) Configuration of the proposed diplexer with no matching network and (b) its coupling diagram.

Moreover, the unloaded quality factor ($Q_u$) of a slotline resonator is always lower than the $Q_u$ of a microstrip resonator with the same size, because the outward radiation of the slotline is bigger than the microstrip line. As studied in [66], the realizable fractional bandwidth of a bandpass filter is inversely proportional to the $Q_u$ for given midband insertion loss. So, the realizable bandwidth of the passband constructed by the proposed SSLDR is in general larger than the ones by adopting the MSLDR, which consists with this design.

## 5.2.4 Development of Diplexer

Next, the configuration of the dual-band BPF in Fig. 5.5(a) is varied as shown in Fig. 5.8(a) to
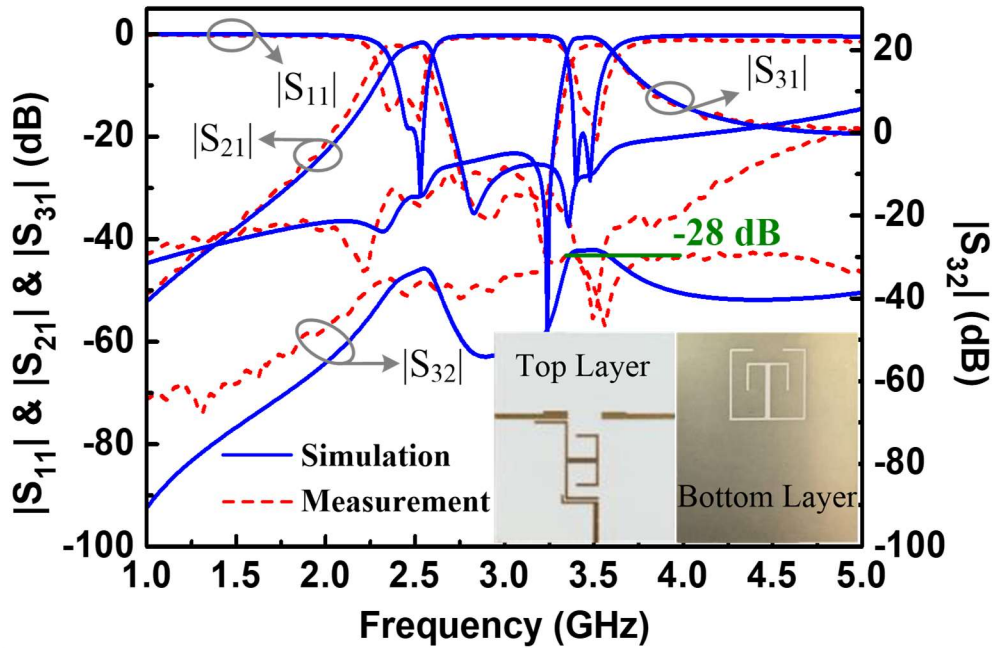


Fig. 5.9    Frequency response of the developed diplexer.

realize a compact diplexer, which has its transmit (TX) and receive (RX) channels operated at 2.45 and 3.45 GHz, respectively. The coupling diagram of this diplexer is illustrated in Fig. 5. 8(b).

As shown in Fig. 5.8(a), the feed lines of Port 1 and 2 are directly coupled to the background SSLDR through the parallel broadsides of the microstrip lines and slotlines. The feed lines of Port 1 and 3 are directly coupled to the MSLDR through the gaps between the parallel microstrip lines. No matching network is used in this diplexer, which simplifies the design of the diplexer and reduces the circuit size significantly. Besides, there are other two merits of the proposed diplexer structure: First, the isolation between the lower and the upper passbands can be increased since the two BPFs are placed on the opposite planes of the substrate; Second, the ground plane of the circuit is effectively used and the space on the top plane is saved which may be used for other circuits.

After optimized design by using Sonnet, the parameters of the feed lines indicated in Fig. 5. 8(a) are: $l_{d1} = l_{d2} = 2.9$, $l_{d3} = 3.65$, $l_{d4} = 1$, $w_{d1} = 0.9$, $w_{d2} = 0.8$, $w_{d3} = 0.25$, $g_d = 0.2$, all in mm. The simulated frequency response of the well-designed diplexer is shown as the blue solid lines in Fig. 5.9. The obtained center frequencies of the two passbands are 2.47 GHz and 3.45 GHz, respectively. The 3D view of current distributions of the diplexer at 2.45 and 3.45 GHz are

portrayed in Fig. 5.10. When the diplexer works at 2.45 GHz, the current is mainly located as the TX Channel (SSLDR) whereas the RX Channel (MSLDR) is considered as open circuit. Contrarily, when the diplexer operates in its upper passband (3.45 GHz), the current is
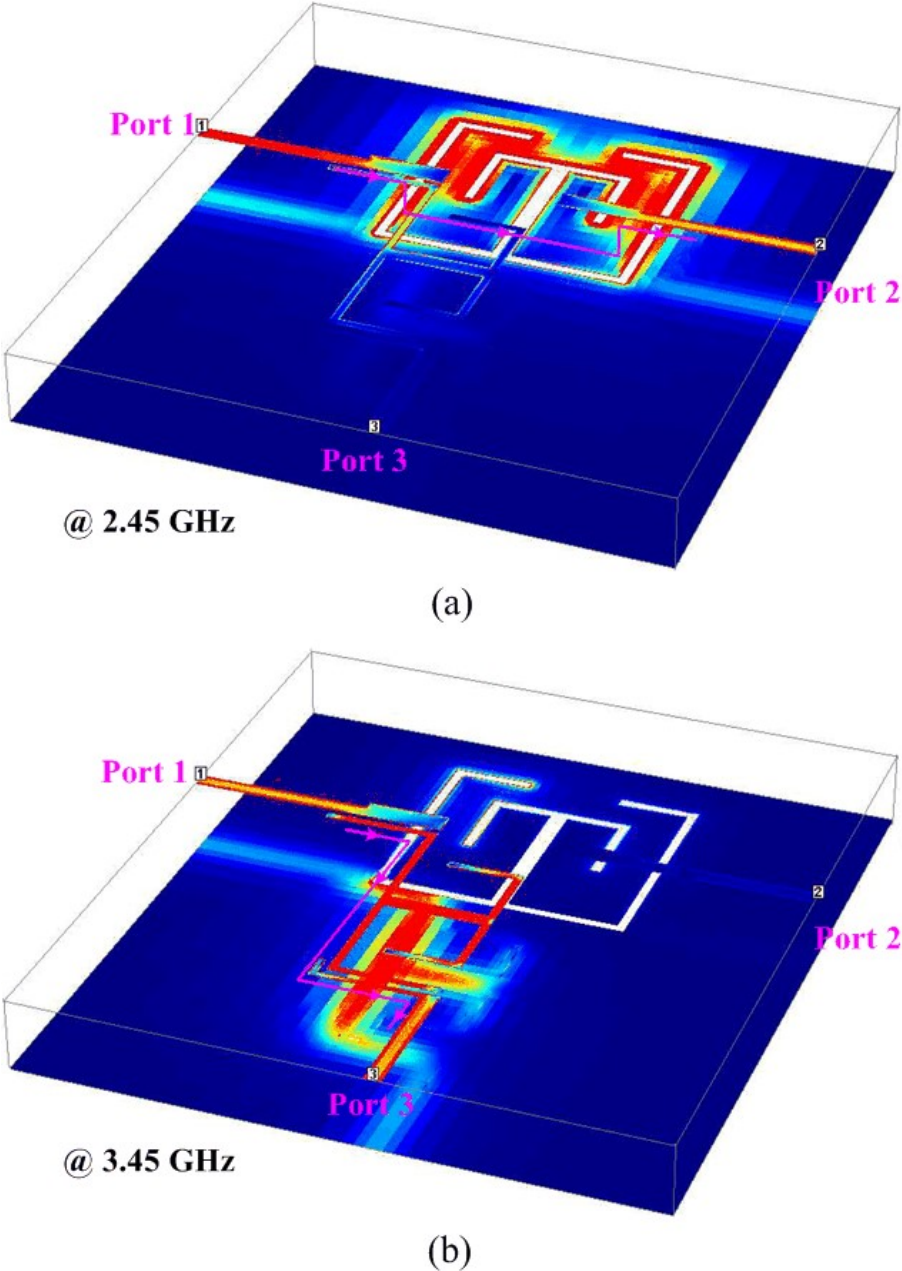


Fig. 5.10   Current distributions of the diplexer at (a) 2.45 and (b) 3.45 GHz.

dominantly distributed in its RX Chanel rather than its TX Channel. The results intuitively interpret the working principle of our proposed diplexer and also verify the feasibility of the proposed structure and design method.

### 5.2.5 Experimental Results and Discussion

The designed diplexer is then fabricated and measured. The circuit photographs are shown as the inserted figures in Fig. 5.9 and the measurement is depicted in red dashed lines. The maximum IL in TX and RX passband is 2.36 dB and 2.15 dB, respectively, and return loss is

Table 5.2 Comparison of other referenced diplexers

| Ref. | Fre. (GHz) | Res. Type | IL (dB) | I.C. | Iso. (dB) | Size ($\lambda_g \times \lambda_g$) |
|---|---|---|---|---|---|---|
| [58] | 2.44 / 3.52 | M | 1.43/1.59 | Yes | ≥ 42 | 0.48×0.59 |
| [59] | 1.95 / 2.14 | M | 1.2 / 1.5 | No | ≥ 35 | 0.36×0.38 |
| [60] | 1.8 / 2.2 | M | 1.43/1.59 | Yes | ≥ 41 | 0.29×0.23 |
| [61] | 1.8 / 2.45 | S | 2.05/2.15 | No | ≥ 25 | 0.37×0.33 |
| This work | **2.45 / 3.45** | **M & S** | **2.36 / 2.15** | **Yes** | ≥ 28 | **0.15×0.24** |

M*: Microstrip, S*: Slotline, I.C.*: Independent Controllable

larger than 12 dB in both passbands. Due to the inherent TZs of the two dual-mode resonators, a good isolation, better than 28 dB over 1 to 5 GHz, between the two output ports, Port 2 and 3, is obtained. Table 5.2 compares the proposed diplexer with those reported diplexers, which shows that the proposed diplexer has the merit of compact circuit size. Moreover, 3-dB improvement of isolation of the designed diplexer is obtained when compared with diplexer that purely configured by slotlines in [61]. This due to the placement of the two Channel filters on opposite planes of the substrate.

## 5.3 Conclusion

A novel compact dual-band BPF and a diplexer are designed by using the proposed MSLDR and SSLDR. The dual-modes of these two resonators are used to design separately the two passbands of the dual-band BPF and the diplexer. No matching network is required, which simplifies the design of the dual-band BPF and the diplexer, and reduces significantly the circuit size.

The design works described in this chapter have been published in the International Journal of

RF and Microwave Computer-Aided Engineering, and part of works in this chapter have been published in the Proceedings of 2017 6th Asia-Pacific Conf. on Antennas and Propagat. (APCAP2017).

# Chapter 6

# Conclusions and Recommendations

## 6.1 Conclusions

Bandpass filter and diplexer are two key components in RF/microwave wireless communication systems. High-performance, such as low insertion loss, high selectivity passbands, high isolation between neighboring channels, and compact size are constantly the main design targets. In this dissertation, it described my research and design works on high performance and compact microwave differential bandpass filters (BPFs) and diplexers in the doctoral period.

To pursuit the compact circuit size, manifold new multimode resonators are proposed and based on them, numerous compact multiband differential BPFs and diplexers are developed. In chapter 3, the multimode stepped-impedance square ring loaded resonators (SRLRs) are proposed and used to constitute the dual-band and tri-band differential BPFs. Then, a modified SRLR and new multimode symmetric-stub-loaded resonator (SSLR) with property of the fully-symmetric structure are proposed to construct high-order high temperature superconducting (HTS) dual-band differential BPFs in chapter 4. Benefiting from the HTS technology, these two designed high-order differential filters exhibit the low insertion-loss in passband, high attenuation in stopband, and steep side-band. In chapter 5, hybrid resonant structure, which consists of a microstrip stub-loaded dual-mode resonator and a slotline stub-loaded dual-mode resonator, is proposed and applied to develop a compact diplexer. High dielectric constant substrate is adopted to reduce the inevitable radiation loss of slotline structure.

The HTS material used in my designed filters is the YBCO film and the substrate is MgO (9.78, 0.5 mm). All the circuits are simulated by using EM software, *Sonnet em* and the fabricated circuits are measured at a temperature of 77 K in a cryogenic cooler. All the measured results are match well with the simulations. In general, the measured insertion loss in passband of a high-order HTS microwave filters is less than 0.5 dB, which show the excellent performance on in-band insertion loss and can be quite useful for application in radio astronomy and wireless communication system with high-sensitivity and high anti-interference capacity.

Besides, it should be emphasized here that the cost of the superconducting circuit is relatively high at present because of the cooler equipment and the advantage is not obvious when compared with the widely used cavity circuit in communication systems now. However, with the development of HTS material technology and processes, the critical temperature of HTS films will be increased and realization of work at room temperature is possible in the future. By then, the presented structures and design method in this book will be very useful to guide the implementation of novel compact and high-performance HTS microwave circuits.

## 6.2 Future Recommendations

Though numerous compact and high performance HTS multi-band differential filters and diplexers have been presented in this dissertation, there are still a lot of works can be carried on for investigating the high performance microwave differential circuits. The authors think that the following issues can be concerned.

The first one is the theory for designing of HTS differential multi-band filtering circuits based on the multimode resonators. Multimode resonators are widely used in designing of multi-band microwave circuits for a compact size. However, resonances provided by multimode resonators are always not controlled independently. Thus, it is difficult to design a multi-band filter, especially the high-order one, with the arbitrary bandwidths and such that the practicality is limited. So, the design theory for high-order HTS filter conduct by using the coupled resonant modes is one of key issue to address.

The second is the investigation of high-order ultra-wideband or ultra-narrowband HTS differential filtering circuits. The existing low-pass prototype based design theory is suitable for narrow-band design and a large error will be occurred when implementing the ultra-wideband or ultra-narrowband ones. So, the theory for design of high-order ultra-wideband or ultra-narrowband filtering circuits should be studied. In addition, the tight coupling structure and extremely weak coupling structure should be investigated for realization of a wide or narrow bandwidth frequency responses.

The third one is the design of a low loss tunable HTS differential filtering circuits. Recently, RF/microwave tunable circuits have progressed at a fast rate and tunable solutions are now considered due to their potential of reducing the system size and complexity. However, introducing of the active components always leading to a large insertion loss in the passbands, which will discount the advantage of low loss of HTS circuits. Therefore, it is meaningful to

explore the now method or structure to design the tunable HTS differential filtering circuits with low loss.

Lastly is the design of differential diplexer based on the hybrid microstrip and slotline resonant structure. As studied in the literatures review, the microstrip-slotline transition structure has the property of intrinsic CM suppression and some differential filters have been designed based on the microstrip and slotline resonant structure. So, based on this design concept, a lot of works on design of compact and high CM suppression differential diplexers can be carried on in a simple design process.

# Published Journal ad Conference Papers

## Journal Papers:

[1] **Baoping Ren**, Haiwen Liu, Zhewang Ma, Masataka Ohira, Pin Wen, Xiaolong Wang, and Xuehui Guan, "Compact Dual-Band Differential Bandpass Filter Using Quadruple-Mode Stepped-Impedance Square Ring Loaded Resonators," *IEEE Access*, vol. 6, pp. 21850-21858, Apr. 2018. (Section 3.2, Chapter 3)

[2] **Baoping Ren**, Zhewang Ma, Haiwen Liu, Xuehui Guan, Pin Wen, Chuanyun Wang, and Masataka Ohira, "Balanced Tri-Band Bandpass Filter Using Sext-Mode Stepped-Impedance Square Ring Loaded Resonators," *IEICE Electronics Express*, vol. 15, no. 18, pp. 1-6, Aug. 2018. (Section 3.3, Chapter 3)

[3] **Baoping Ren**, Zhewang Ma, Haiwen Liu, Xuehui Guan, Xiaolong Wang, Pin Wen, and Masataka Ohira, "Differential Dual-Band Superconducting Bandpass Filter Using Multi-Mode Square Ring Loaded Resonators With Controllable Bandwidths," *IEEE Transactions on Microwave Theory and Techniques*, vol. 67, no. 2, pp. 726-737, Feb. 2019. (Section 4.2, Chapter 4)

[4] **Baoping Ren**, Haiwen Liu, Zhewang Ma, Masataka Ohira, Xuehui Guan, Pin Wen, and Xiaolong Wang, "Compact Dual-Band Bandpass Filter and Diplexer Using Hybrid Resonant Structure with Independently Controllable Dual Passbands," *International Journal of RF and Microwave Computer-Aided Engineering*, vol.29, no. 1, e21435, Jan. 2019. (Chapter 5)

[5] **Baoping Ren**, Zhewang Ma, Haiwen Liu, Xuehui Guan, Pin Wen, Xiaolong Wang, and Masataka Ohira, "Miniature Dual-Band Bandpass Filter Using Modified Quarter-Wavelength SIRs With Controllable Passbands," *Electronics Letters*, vol. 55, no. 1, pp. 38-40, Jan. 2019.

## Conferences Papers:

[1] **Baoping Ren**, Zhewang Ma, Haiwen Liu, Masataka Ohira, Pin Wen, Xiaolong Wang, and Xuehui Guan, "Design of a Compact Diplexer Using Microstrip and Slotline Dual-Mode Resonators," *2017 6th Asia-Pacific Conf. on Antennas and Propagat. (APCAP2017)*, Xi'an, China, Oct. 2017. (Chapter5)

[2] **Baoping Ren**, Zhewang Ma, Haiwen Liu, Masataka Ohira, Xuehui Guan, and Pin Wen, "Design of Balanced Dual-Band Superconducting Bandpass Filter With High Selectivity and Deep Common-Mode Suppression," *2018 Asia-pacific Microwave Conference (APMC 2018)*, pp. 423-425, Kyoto, Japan, Nov. 2018. (Section 4.3, Chapter 4)

# Bibliography:

[1] L. Sun and Y. S. He, "Research Progress of High Temperature Superconducting Filters in China," *IEEE Trans. Appl. Supercond.*, vol. 24, no. 5, p. 1501308, Oct. 2014.

[2] W. J. Feng, W. Q. Che, and Q. Xue, "The proper balanced: overview of microstrip wideband balance circuits with wideband common mode suppression," *IEEE Micro. Mag.*, vol. 16, no. 5, pp:55-68, Jun. 2015.

[3] F. Martín, L. zhu, J. S. Hong, and F. Medina, Balanced Microwave Filters. New York, NY, USA: Wiley, 2018.

[4] C.-H. Wu, C.-H. Wang, and C. H. Chen, "Novel balanced coupled-line bandpass filters with common-mode noise suppression," *IEEE Trans. Microw. Theory Techn.*, vol. 55, no. 2, pp. 287‑295, Feb. 2007.

[5] C.-H. Wu, C.-H. Wang, and C. H. Chen, "Stopband-extended balanced bandpass filter using coupled stepped-impedance resonators," *IEEE Microw. Wireless Compon. Lett.*, vol. 17, no. 2, pp. 507‑509, Jun. 2007.

[6] C.-H. Wu, C.-H. Wang, and C. H. Chen, "Balanced coupled-resonator bandpass filters using multisection resonators for common-mode suppression and stopband extension," *IEEE Trans. Microw. Theory Techn.*, vol. 55, no. 8, pp. 1756‑1763, Aug. 2007.

[7] J. Shi and Q. Xue, "Balanced bandpass filters using center-loaded half-wavelength resonators," *IEEE Trans. Microw. Theory Techn.*, vol. 58, no. 4, pp. 970‑977, Apr. 2010.

[8] J. Shi and Q. Xue, "Dual-band and wide-stopband single-band balanced bandpass filters with high selectivity and common-mode suppression," *IEEE Trans. Microw. Theory Techn.*, vol. 58, no. 8, pp. 2204‑2212, Aug. 2010.

[9] Y. C. Li and Q. Xue, "Tunable balanced bandpass filter with constant bandwidth and high common-mode suppression," *IEEE Trans. Microw. Theory Techn.*, vol. 59, no. 10, pp. 2452‑2460, Oct. 2011.

[10] T. B. Lim and L. Zhu, "A differential-mode wideband bandpass filter on microstrip line for UWB application," *IEEE Microw. Wireless Compon. Lett.*, vol. 19, no. 10, pp. 632‑634, Oct. 2009.

[11] T. B. Lim and L. Zhu, "Highly selective differential-mode wideband bandpass filter for UWB application," *IEEE Microw. Wireless Compon. Lett.*, vol. 21, no. 3, pp. 133‑135, Mar. 2011.

[12] X.-H. Wu and Q.-X. Chu, "Compact differential ultra-wideband bandpass filter with

common-mode suppression," *IEEE Microw. Wireless Compon. Lett.*, vol. 22, no. 9, pp. 456‑458, Sep. 2012.

[13] X.-H. Wu, Q.-X. Chu, and L.-L. Qiu, "Differential wideband bandpass filter with high-selectivity and common-mode suppression," *IEEE Microw. Wireless Compon. Lett.*, vol. 23, no. 12, pp. 644‑646, Dec. 2013.

[14] X.-H. Wang, Q. Xue, and W.-W. Choi, "A novel ultra-wideband differential filter based on double-sided parallel-strip line," *IEEE Microw. Wireless Compon. Lett.*, vol. 20, no. 8, pp. 471‑473, Aug. 2010.

[15] Y.-J. Lu, S.-Y. Chen, and P. Hsu, "A differential-mode wideband bandpass filter with enhanced common-mode suppression using slotline resonator," *IEEE Microw. Wireless Compon. Lett.*, vol. 22, no. 10, pp. 503‑505, Oct. 2012.

[16] C.-H. Lee, C. I. G. Hsu, and C.-J. Chen, "Band-notched balanced UWB BPF with stepped-impedance slotline multi-mode resonator," *IEEE Microw. Wireless Compon. Lett.*, vol. 22, no. 4, pp. 182‑184, Apr. 2012.

[17] J. Shi *et al.*, "Compact low-loss wideband differential bandpass filter with high common-mode suppression," *IEEE Microw. Wireless Compon. Lett.*, vol. 23, no. 9, pp. 480‑482, Sep. 2013.

[18] X. Guo, L. Zhu, K. W. Tam, and W. Wu, "Wideband differential bandpass filter on multimode slotline resonator with intrinsic common-mode rejection," *IEEE Trans. Microw. Theory Tech.*, vol. 63, no. 5, pp.1587-1594, May 2015.

[19] X. Guo, L. Zhu, W. Wu, "Strip-loaded slotline resonators for differential wideband bandpass filter with intrinsic common-mode rejection," *IEEE Trans. Microw. Theory Tech.*, vol. 64, no. 2, pp.450-458, Feb. 2016.

[20] X. Guo, L. Zhu, W. Wu, "Optimized design of differential moderate-band BPF on coupled slotline resonators," *IEEE Microw. Wireless Compon. Lett.*, vol. 27, no. 3, pp.263-265, Mar. 2017.

[21] W. J. Feng, W. Q. Che, Y. L. Ma, and Q. Xue, "Compact wideband differential bandpass filter using half-wavelength ring resonator," *IEEE Microw. Wireless Compon. Lett.*, vol. 23, no. 2, pp. 81‑83, Feb. 2013.

[22] W. J. Feng and W. Q. Che, "Novel wideband differential bandpass filters based on T-shaped structure," *IEEE Trans. Microw. Theory Tech.*, vol. 60, no. 6, pp. 1560‑1568, Jun. 2012.

[23] W. J. Feng, W. Q. Che, L. M. Gu, and Q. Xue, "High selectivity wideband balanced

bandpass filters using symmetrical multimode resonators," *IET Microw. Antennas Propagat.*, vol. 7, no. 12, pp. 1005‑1015, Nov. 2013.

[24] W. J. Feng and W. Q. Che, "Wideband differential bandpass filter based on three-line coupled structure," *Electron. Lett.*, vol. 48, no. 16, pp. 1007‑1008, Aug. 2012.

[25] C. -H. Lee, C. -I. G. Hsu, and C. -C. Hsu, "Balanced dual-band BPF with stub-loaded SIRs for common-mode suppression," *IEEE Microw. Wireless Compon. Lett.*, vol. 20, no. 2, pp. 70‑72, Feb. 2010.

[26] J. Shi and Q. Xue, "Dual-band and wide-stopband single-band balanced bandpass filters with high selectivity and common-mode suppression," *IEEE Trans. Microw. Theory Tech.*, vol. 58, no. 8, pp.2204-2212, Aug. 2010.

[27] J. Shi and Q. Xue, "Balanced bandpass filters using center-loaded half-wavelength resonators," *IEEE Trans. Microw. Theory Tech.*, vol. 58, no. 4, pp.970-977, Apr. 2010.

[28] Y.-H. Cho, I.-S. Jeon, X.-G. Wang, S.-W. Yun, and D.-C. Park, "Balanced dual-band bandpass filter using microstrip resonator loaded with lumped-elements," *Proceedings of the Asia-Pacific Micro. Conf.*, pp. 1286-1289, 2012.

[29] X. H. Wu, F. Y. Wan, and J. X. Ge, "Stub-loaded theory and its application to balanced dual-band bandpass filter design," *IEEE Microw. Wireless Compon. Lett.*, vol. 26, no. 4, pp. 231‑233, Apr. 2016.

[30] W. Jiang, Y. J. Peng, W. Shen, and G. A. Wang, "Dual-mode dual-band balanced filter with high differential-mode frequency selectivity and enhanced common-mode suppression," 2015 *IEEE MTT-S International Microwave Symposium*, pp. 1-3, 2015.

[31] Y. -H. Cho and S. -W. Yun, "Design of balanced dual-band bandpass filters using asymmetrical coupled lines," *IEEE Trans. Microw. Theory Tech.*, vol. 61, no. 8, pp.2814-2820, Aug. 2013.

[32] Y. -H. Cho and S. -W. Yun, "Design of balanced dual-band bandpass filters using asymmetrical coupled lines," *IEEE Trans. Microw. Theory Tech.*, vol. 61, no. 8, pp.2814-2820, Aug. 2013.

[33] X. Guo, L. Zhu, and W. Wu, "Balanced wideband/dual-band BPFs on a hybrid multimode resonator with intrinsic common-mode rejection," *IEEE Trans. Microw. Theory Tech.*, vol. 64, no. 7, pp.1997-2005, Jul. 2016.

[34] X. Guo, L. Zhu, and W. Wu, "A dual-wideband differential filter on strip-loaded slotline resonators with enhanced coupling scheme," *IEEE Microw. Wireless Compon. Lett.*, vol. 26, no. 11, pp. 882‑884, Nov. 2016.

[35] L. Yang, W. -W, Choi, K. -W. Tam, and L. Zhu, "Balanced dual-band bandpass filter with multiple transmission zeros using doubly short-ended resonator coupled line," *IEEE Trans. Microw. Theory Tech.*, vol. 63, no. 7, pp.2225-2232, Jul. 2015.

[36] L. H. Zhou, Y. L. Ma, J. Shi, J. X. Chen, and W. Q. Che, "Differential dual-band bandpass filter with tunable lower band using embedded DGS unit for common-mode suppression," *IEEE Trans. Microw. Theory Tech.*, vol. 64, no. 12, pp.4183-4191, Dec. 2016.

[37] X. Xu, J. P. Wang, G. Zhang, and J. X. Chen, "Design of balanced dual-band bandpass filter based on substrate integrated waveguide," *Electron. Lett.*, vol. 49, no. 20, pp. 1278-1280, Sep. 2013.

[38] Y. J. Shen, H. Wang, W. Kang, and W. Wu, "Dual-band SIW differential bandpass filter with improved common-mode suppression," *IEEE Microw. Wireless Compon. Lett.*, vol. 25, no. 2, pp. 100‑102, Feb. 2015.

[39] L. H. Zhou and J. X. Chen, "Differential dual-band bandpass filters with flexible frequency ratio using Asymmetrical shunt branches for wideband CM suppression," *IEEE Trans. Microw. Theory Tech.*, vol. 65, no. 11, pp.4606-4615, Nov. 2017.

[40] F. Wei, Y. J. Guo, P. Y. Qin, and X. W. Shi, "Compact balanced dual- and tri-band bandpass filters based on stub loaded resonators," *IEEE Microw. Wireless Compon. Lett.*, vol. 25, no. 2, pp. 76‑78, Feb. 2015.

[41] S.-X. Zhang, Z.-H. Chen, and Q.-X. Chu, "Design of tri-band balanced bandpass filter with controllable frequencies and bandwidths," *IEEE MTT-S International Microwave Symposium (IMS)*, pp. 1823-1825, 2017.

[42] F. Wei, P.-Y. Qin, Y. J. Guo, C. Ding, and X. W. Shi, "Compact balanced dual- and tri-band BPFs based on coupled complementary split-ring resonators (C-CSRR)," *IEEE Microw. Wirel. Compon. Lett.*, vol. 26, no. 2, pp. 107-109, Feb. 2016.

[43] S.-X. Zhang, L.-L. Qiu, and Q.-X. Chu, "Multiband balanced filters with controllable bandwidths based on slotline coupling feed," *IEEE Microw. Wirel. Compon. Lett.*, vol. 27 no. 11, pp. 974-976, Nov. 2017.

[44] H. W. Liu, Y. Song, B. P. Ren, P. Wen, X. H. Guan, and H. X. Xu, "Balanced tri-band bandpass filter design using octo-section stepped-impedance ring resonator with open stubs," *IEEE Microw. Wirel. Compon. Lett.,* vol. 27, no. 10, pp. 912-914, Oct. 2017.

[45] T. Shen, K. A. Zaki, and T. G. Dolam, "Rectangular waveguide diplexers with a circular waveguide common port," *IEEE Trans. Microw. Theory Tech.*, vol. 51, no. 2, pp.578-582, Feb. 2003.

[46] T. Skaik, M. Lancaster, M. L. Ke, and Y. Wang, "A micromachined WR-3 band waveguide diplexer based on coupled resonator structures," *Proceedings of the 41ˢᵗ European Microwave Conference*, pp. 770-773, Oct. 2011.

[47] L. Zhu, R. R. Mansour, and M. Yu, "Compact waveguide dual-band filters and diplexers," *IEEE Trans. Microw. Theory Tech.*, vol. 65, no. 5, pp.1525-1533, May 2017.

[48] H. J. Tang, W. Hong, J.-X. Chen, G. Q. Luo, and K. Wu, "Development of millimeter-wave planar diplexers based on complementary characters of dual-mode substrate integrated waveguide filters with circular and elliptic cavities," *IEEE Trans. Microw. Theory Tech.*, vol. 55, no. 4, pp.776-782, Apr 2007.

[49] Y. D. Dong and T. Itoh, "Substrate integrated waveguide loaded by complementary split-ring resonators for miniaturized diplexer design," *IEEE Microw. Wirel. Compon. Lett.,* vol. 21, no. 1, pp. 10-12, Jan. 2011.

[50] F. Cheng, X. Q. Liu, K. J. Song, Y. Jiang, and Y. Fan, "Compact diplexer with high isolation using the dual-mode substrate integrated waveguide resonator," *IEEE Microw. Wirel. Compon. Lett.,* vol. 23, no. 9, pp. 459-461, Sep. 2013.

[51] S. Sirci, J. D. Martínez, J. Vague, and V. E. Boria, "Substrate integrated waveguide diplexer based on circular triplet combline filters," *IEEE Microw. Wirel. Compon. Lett.,* vol. 25, no. 7, pp. 430-432, Jul. 2015.

[52] T. Jaschke, B. Rohrdantz, J.-P. Mohncke, and A. F. Jacob, "A Ka-band substrate-integrated waveguide diplexer with wide frequency spread," *Proceedings of the 46ᵗʰ European Microwave Conference*, pp. 779-782, Oct. 2016.

[53] I. Llamas-Garro, F. Mira, P. Zheng, Z. F. Liu, L.-S. Wu, and Y. Wang, "All-resonator based LTCC diplexer using substrate-integrated-waveguides," *Electro. Lett.*, vol. 53, no. 21, pp. 1410-1412, Oct. 2017.

[54] K. Zhou, C. X. Zhou, W. Wu, "Compact SIW diplexer with flexibly allocated bandwidths using common dual-mode cavities," *IEEE Microw. Wirel. Compon. Lett.,* vol. 28, no. 4, pp. 317-319, Apr. 2018.

[55] T. Yang, P. L. Chi, and T. Itoh, "High isolation and compact diplexer using the hybrid resonators," *IEEE Trans., Microw. Wireless Compon. Lett.*, vol. 20, no. 10, pp. 551-553, Oct. 2010.

[56] K. Dhwaj, L. J. Jiang, and T. Itoh, "Microstrip diplexer with low channel-frequency ratio," *Proceedings of the Asia-Pacific Microwave Conference*, pp. 1-4, Jul. 2016.

[57] C.-F. Chen, T.-Y. Huang, C.-P. Chou, and R.-B. Wu, "Microstrip diplexers design with

common resonator sections for compact size, but high isolation," *IEEE Trans. Microw. Theory Tech.*, vol. 54, no. 5, pp. 1945-1952, May. 2006.

[58] M.-L. Chuang and M.-T. Wu, "Microstrip diplexer design using common T-shaped resonator," *IEEE Microw. Wireless Compon. Lett.*, vol. 11, no. 20, pp. 583-585, Nov. 2011.

[59] X. Guan, F. Q. Yang, H. W. Liu, and L. Zhu, "Compact and high-isolation diplexer using dual-mode stub-loaded resonators," *IEEE Microw. Wireless Comp. Lett.*, vol. 24, no. 6, pp. 385-387. Jun. 2013.

[60] F. C. Chen, H. T. Hu, J. M. Qiu, M. F. Guo, and Q. X. Chu, "Novel diplexer with improved isolation using asymmetric transmission zeros technique," *Chin J Electron.*, vol. 25, no. 3, pp. 591-594, May 2016.

[61] H. W. Liu, W. Y. Xu, Z. C. Zhang, and X. Guan, "Compact diplexer using slotline stepped impedance resonator," *IEEE Trans. Microw. Wireless Compon. Lett.*, vol. 23, no. 2, pp. 75-77, Feb. 2013.

[62] D. Chen, L. Zhu, H. Z. Bu, and C. H. Cheng, "A novel planar diplexer using slotline-loaded microstrip ring resonator," *IEEE Trans. Microw. Wireless Compon. Lett.*, vol. 25, no. 11, pp. 706-708, Nov. 2015.

[63] Z. P. Li, L. J. Zhang, T. Su, and C. H. Liang, "A compact microstrip quadruplexer using slotline stepped impedance stub loaded resonators," *Prog. Electromagn. Res.*, vol. 140, pp. 509-522, Jun. 2013.

[64] Z. L. Wu, C.-H. Lee, and H.-H. Chen, "Balun diplexer design in hybrid structure of microstrip line and slot-line," *Proceedings of the Asia-Pacific Microwave Conference*, pp. 1-3, Dec. 2015.

[65] H.-W. Deng, Y.-J. Zhao, Y. He, H. Liu, and H.-L. Wang, "Compact diplexer with slotline resonators for wideband and WLAN application," *Microw. Opt. Techn. Let.*, vol. 56, no. 11, Nov. 2014.

[66] J. S. Hong and M. J. Lancaster, Microwave Filter for RF/Microwave Application. New York, NY, USA: Wiley, 2001.

[67] H. K. Onnes, On the sudden change in the rate at which the resistance of mercury disappears, Comm Phys Lab Univ Leiden, No. 124c, 1911.

[68] J. G. Bednorz and K. A. Müller, "Possible high Tc superconductivity in the Ba-La-Cu-O system," *Phys. Z.*, B64, 189, 1986.

[69] M. J. Lancaster, Passive microwave device applications of high-temperature superconductors. Cambridge, UK: Cambridge University Press, 1997.

[70] M. Abramowitz and I. A. Stegun, Handbook of mathematical Functions, Dover Publications, New York, 1972.

[71] J. M. O'callaghan, C. Collado, S. H. Talisa, J. Mateu, Superconducting filters and passive components. Wiley, 2005.

[72] J. W. Ekin, A. J. Panson, and B. A. Blankenship, "Method for making low-resistivity contacts to high Tc superconductors," *Appl. Phys. Lett.*, vol. 52, no. 4, pp. 331-333, Jan. 1988.

[73] S. H. Talisa et al., "High-temperature superconducting space qualified multiplexers and delay lines," *IEEE Trans. Microw. Theory Tech.*, vol. 44, no. 7, pp. 1229-1239, Jul. 1996.

[74] H. W. Liu, B. P. Ren, X. H. Guan, J. H. Lei, and S. Li, "Compact dual-band bandpass filter using quadruple-mode square ring loaded resonator (SRLR)," *IEEE Microw. Wireless Compon. Lett.*, vol. 23, no. 4, pp. 181–183, Apr. 2013.

[75] T. J. Du, B. R. Guan, A. T. Wu, and Z. H. Zhang, "Dual-band bandpass filter based on quadruple-mode open stub loaded square ring resonator," *2017 IEEE International Conference on Signal Processing, Communications and Computing (ICSPCC)*, Xiamen, China, 2017, pp. 1-4.

[76] H. W. Liu, B. P. Ren, X. H. Guan, P. Wen, and Y. Wang, "Quad-band high-temperature superconducting bandpass filter using quadruple-mode square ring loaded resonator," *IEEE Trans. Microw. Theory Tech.*, vol. 62, no. 12, pp.2931-2941, Dec. 2014.

[77] B. P. Ren, H. W. Liu, Z. W. Ma, M. Ohira, P. Wen, X. L. Wang, and X. X. Guan, "Compact Dual-Band Differential Bandpass Filter Using Quadruple-Mode Stepped-Impedance Square Ring Loaded Resonators," *IEEE Access*, vol. 6, pp. 21850-21858, May 2018.

[78] S. B. Zhang and L. Zhu, "Compact and high selectivity microstrip bandpass filters using triple-/quad-mode stub-loaded resonator," *IEEE Microw. Wirel. Compon. Lett.* vol. 21, no. 10, pp.522-524, Oct. 522.

[79] X. L. Lu, B. S. Cao, X. B. Guo, X. P. Zhang, X. K. Song, Y. Heng, and Z. Xu, "Design of a high-order dual-band superconducting filter with controllable frequencies and bandwidths," *IEEE Trans. Appl. Supercond.*, vol. 24, no. 2, p. 1500205, Apr. 2014.

[80] F. Song, B. Wei, L. Zhu, B. S. Cao, and X. L. Lu, "Dual-band high-temperature superconducting bandpass filter using quint-mode stub-loaded resonators," *IEEE Trans. Appl. Supercond.*, vol. 25, no. 4, p. 1501410, Aug. 2015.

[81] H. W. Liu, B. P. Ren, S. X. Hu, X. H. Guan, P. Wen, and J. M. Tang, "High-order dual-

band superconducting bandpass filter with controllable bandwidths and multitransmission zeros," *IEEE Trans. Microw. Theory Tech.*, vol. 65, no. 10, pp.3813-3823, Nov. 2017.

[82] P. Y. Ma, B. Wei, J. S. Hong, B. S. Cao, X. B. Guo, and L. N. Jiang, "Design of dual-mode dual-band superconducting filters," *IEEE Trans. Appl. Supercond.*, vol. 27, no. 7, p. 1502809, Oct. 2017.

[83] J. Z. Chen, N. Wang, Y. He, and C. H. Liang, "Fourth-order tri-band bandpass filter using square ring loaded resonators," *Electron. Lett.*, vol. 47, no. 15, pp. 858 – 859, Jul. 2011.

[84] M. T. Doan, W. Q. Che, and W. J. Feng, "Tri-band bandpass filter using square ring short stub loaded resonator," *Electron. Lett.*, vol. 48, no. 2, pp. 106 – 107, Jul. 2012.

[85] R. J. Cameron, "General coupling matrix synthesis methods for Chebyshev filtering functions," *IEEE Trans. Microw. Theory Tech.*, vol. 47, no. 4, pp.433-442, Apr. 1999.

[86] B. Wu, C. H. Liang, Q. Li, and P. Y. Qin, "Novel dual-band filter incorporating defected SIR and Microstrip SIR," *IEEE Microw Wireless Compon. Lett.*, vol. 18, no. 6, pp. 392-394, 2008.

[87] X. Y. Zhang, J. X. Chen, Q. Xue, "Novel dual-band filter using slotline and microstrip resonators," *Microw Opt Technol Lett.*, vol. 49, no. 5, pp. 1080-1081, 2007.

[88] B. Wu, C. H. Liang, P. Y. Qin, and Q. Li, "Compact dual-band filter using defected stepped impedance resonator," *IEEE Microw Wireless Compon Lett., .* 18, no. 10, pp. 674-676, 2008.

[89] J.-X. Chen, J. Shi, and Z.-H. Bao, "Tunable and switchable bandpass filters using slot-line resonators," *Prog. Electromagn. Res.*, vol. 111, pp. 25-41, Nov. 2011.

[90] J. S Hong, H. Shaman, Y. H. Chun, "Dual-mode microstrip open-loop resonators and filters," *IEEE Trans Microw Theory Tech*, vol. 55, no. 8, pp. 1764-1770, Aug. 2007.

[91] G. Ramesh, I. Bahl I, and M. Bozzi. Microstrip lines and slotlines. Norwood, MA, USA: Artech House, 2013.

[92] C.-Y. Chen and C.-Y. Hsu, "A simple and effective method for microstrip dual-band filters design," *IEEE Microw Wireless Compon Lett.*, vol.16, no. 5, pp. 246-248, 2006.

[93] J. Li, "Multi-mode resonators with quad-/penta-/sext-mode resonant characteristics and their applications to bandpass filters," *Int J RF Microw Comput Aided Eng.,* vol.27, ID. e21072, 2017.